



HAL
open science

Spin noise spectroscopy in metatable helium

Shikang Liu

► **To cite this version:**

Shikang Liu. Spin noise spectroscopy in metatable helium. Quantum Physics [quant-ph]. Université Paris-Saclay; East China normal university (Shanghai), 2023. English. NNT: 2023UPASP051 . tel-04190120

HAL Id: tel-04190120

<https://theses.hal.science/tel-04190120v1>

Submitted on 29 Aug 2023

HAL is a multi-disciplinary open access archive for the deposit and dissemination of scientific research documents, whether they are published or not. The documents may come from teaching and research institutions in France or abroad, or from public or private research centers.

L'archive ouverte pluridisciplinaire **HAL**, est destinée au dépôt et à la diffusion de documents scientifiques de niveau recherche, publiés ou non, émanant des établissements d'enseignement et de recherche français ou étrangers, des laboratoires publics ou privés.

Spectroscopie de bruit de spin dans l'hélium métatable

Spin noise spectroscopy in metastable helium

Thèse de doctorat de l'université Paris-Saclay et de l'École normale supérieure de l'Est de la Chine

École doctorale n° 572, Ondes et Matière (EDOM)
Spécialité de doctorat: Physique
Graduate School: Physique. Référent: ENS Paris-Saclay

Thèse préparée dans l'unité de recherche LuMin (Université Paris-Saclay, CNRS, ENS Paris-Saclay), sous la direction de Fabien Bretenaker, directeur de recherche, la co-direction de E Wu, Professeur.

Thèse soutenue à Shanghai, le 09 Juin 2023, par

Shikang LIU

Composition du jury:

Membres du jury avec voix délibérative

Emmanuelle Deleporte Professeur, Laboratoire Lumière, Université Paris-Saclay	Président
Athanasios Laliotis Assistant professor, Laboratoire de Physique des Lasers, Université Sorbonne Paris Nord	Examineur
Jun He Professeur, State Key Laboratory of Quantum Optics and Quantum Optics Devices, Shanxi University	Examineur
Bingwen Hu Professeur, École des sciences physiques et électroniques, East China Normal University	Examineur

Spin noise spectroscopy in metastable helium

Abstract

This Ph.D. thesis mainly addresses the spin noise spectroscopy (SNS) of metastable helium. We report for the first time the measurement of spontaneous spin noise of metastable helium atom ensemble using non-invasive spin noise spectroscopy. We utilize an off-resonant laser to investigate the random fluctuations of the Zeeman states of the ground level of metastable helium with a mild magnetic field of approximately 1 Gauss. Moreover, we examine the changes in the spectral pattern when the probe approaches the resonance. We investigate the two main types of polarization noise of the probe, namely Faraday rotation noise and ellipticity noise. To replicate the experimental spin noise signal qualitatively and quantitatively, we construct a simulation model that performs well even near resonance.

After the investigation of the simpler level structure of the metastable helium transition line, we extend spin noise spectroscopy to the transition lines with more complicated structures. Our simulation results are consistent with the experimental findings, which are distinct from those obtained using the simpler level structure. To explain the SNS pattern's characteristics near different transition lines, we have developed a comprehensive theoretical spin-1 model based on the superposition states theory.

We then investigate the correlation between Faraday rotation noise and ellipticity noise. Using the eight noise modes of spin-1, we are able to explain the correlation under different conditions. Additionally, we study the effect of magnetic field noise on the SNS pattern. The magnetic field noise is found to alter the noise spectra pattern, and the eight noise modes theory is able to well explain this phenomenon well.

This Ph.D. work mainly serves as proof of principle. The simple level structure of metastable helium provides an ideal model to study the phenomenon of spin noise spectroscopy in spin-1 systems. These findings offer a fresh perspective on SNS and the characterization of spin-1 systems. This new understanding can assist in further research in this area.

Keywords: spin noise spectroscopy, spin fluctuations, Faraday rotation, metastable helium.

Résumé

Cette thèse porte principalement sur la spectroscopie de bruit de spin (SNS) de l'hélium métastable. Nous rapportons pour la première fois dans cette thèse la mesure du bruit de spin spontané d'un ensemble d'atomes d'hélium métastable en utilisant la spectroscopie de bruit de spin non invasive. Nous utilisons un laser hors résonance pour étudier les fluctuations aléatoires des sous-niveaux Zeeman du niveau métastable de l'hélium sous un champ magnétique relativement faible d'environ 1 Gauss. De plus, nous examinons les changements dans le spectre lorsque la sonde s'approche de la résonance. Nous étudions les deux principaux types de bruit de polarisation de la sonde, à savoir le bruit de rotation de Faraday et le bruit d'ellipticité. Pour reproduire qualitativement et quantitativement le signal de bruit de spin expérimental, nous construisons un modèle de simulation qui fonctionne bien même près de la résonance.

Après l'étude de la transition la plus simple de l'hélium métastable, nous étudions la spectroscopie de bruit de spin aux transitions de l'hélium métastable avec des structures plus compliquées. Nos résultats de simulation sont cohérents avec les résultats expérimentaux, qui sont distincts de ceux obtenus en utilisant la structure de niveau la plus simple. Pour expliquer les caractéristiques du SNS près des différentes transitions, nous avons développé un modèle théorique complet basé sur le modèle d'états de superposition.

Nous avons ensuite étudié la corrélation entre le bruit de rotation de Faraday et le bruit d'ellipticité. En utilisant les huit modes de bruit du spin-1, nous sommes capables d'expliquer les corrélations dans différentes conditions. De plus, nous avons étudié l'effet du bruit du champ magnétique sur le modèle SNS. On a constaté que le bruit du champ magnétique altérait le spectre de bruit, et la théorie des huit modes de bruit est capable d'expliquer correctement ce phénomène.

Ce travail de thèse sert principalement de preuve de principe. La structure de niveaux simple de l'hélium métastable a fourni un modèle idéal pour étudier le phénomène de spectroscopie de bruit de spin dans les systèmes de spin-1. Ces résultats offrent une nouvelle perspective pour comprendre le SNS et la caractérisation des systèmes de spin-1, ce qui peut aider à poursuivre les recherches dans ce domaine.

Mots-clés: spectroscopie de bruit de spin, fluctuations de spin, Rotation de Faraday,, hélium métastable.

摘要

该论文主要研究了亚稳态氮气的自旋噪声谱。我们首次采用非扰动的自旋噪声谱技术测量了亚稳态氮气的自发自旋噪声 (SNS)。我们采用非共振激光和一个大约1高斯的外置弱磁场来检测亚稳态氮的随机波动。在文中，我们检测了当激光靠近氮气的共振吸收区域时自旋噪声功率谱的变化。文中研究了探测光的两种偏振噪声类型，分别是法拉第旋转噪声和椭圆率噪声。我们构建了一个数值模拟模型，该模型可以定性和定量地复现我们的实验结果。

我们首先将光的频率放在了具有较简单的能级结构的共振跃迁频率处，之后我们在其他共振跃迁频率处进行了更加一般化的研究。对于不同的能级结构，我们的数值模拟结果均和实验结果一致。但不同的能级结构带来的自旋噪声功率谱的结果是不同的。基于量子叠加态模，我们提出了一个自旋-1模型。该模型可以直观地解释自旋-1系统中存在的高次谐波共振峰及其偏振依赖行为。相应的，我们对比了不同的能级结构中的量子叠加态结构，发现了自旋噪声谱在不同能级结构的自旋噪声谱不同的原因。

此外，我们研究了法拉第旋转噪声和椭圆率噪声之间的关联性。我们发现在两者之间的关联性和探测光的频率以及探测光的偏振方向有关。通过研究自旋-1模型中的八种噪声振荡模式，我们可以成功解释这种关联性背后的原因。最后，我们研究了外置磁场噪声对自旋噪声谱的影响，这种影响同样可以通过自旋-1模型的八种噪声振荡模式的到解释。

本论文的工作主要为原理性证明。亚稳态氮气简单的能级结构提供了一个理想的模型来研究自旋-1系统在自旋噪声谱下的新现象。这些发现为理解自旋噪声谱和自旋-1系统提供了一个新的视角并为自旋噪声谱将来的研究提供理论和实验依据。

Keywords: 自旋噪声谱, 自旋随机波动, 法拉第效应, 亚稳态氮气.

Preface

Spin noise spectroscopy (SNS) was first performed in alkali metal atom vapors due to their relatively simple structure with only one valence electron, which makes them easier to manipulate and control in experiments [1, 2]. Over time, SNS has found successful applications in the study of semiconductor and quantum dots [3–6] and reveal new insights into spin dynamics in condensed matter physics [7, 8].

In recent decades, the rapid development of SNS has been driven by advances in narrow linewidth lasers and low noise electronics. Despite these advancements, the analysis methods for experimental results in SNS still require further improvement. While the simplified spin 1/2 model has been widely used as a physical model for SNS and has provided intuitive preliminary results [9], it can only account for conventional orientation noise for linearly polarized probe lasers with large detuning.

This Ph.D. work focuses on investigating spin noise spectroscopy of metastable helium-4 ensembles at room temperature. Although this system may not possess some of the unique characteristics found in other systems, such as the novel many-body quantum states arising from interactions of ultracold atoms [7], the presence of free and localized carriers in doped semiconductors [5], and spin exchange between different species [10], it has revealed several new phenomena. These include second harmonic resonance, polarization patterns [11, 12], optical light shift [13], correlation of different kinds of probe noise, and the effect of magnetic field noise. The simple level structure of metastable helium provides clear explanations for these phenomena.

The goal of this PhD research is to investigate the properties of a spin-one system. We propose a complementary model to the spin 1/2 model to address questions that cannot be answered by the latter. Our aim is to develop a practical and simple spin-one model that can explain phenomena in a manner similar to the spin 1/2 model. Currently, the spin-1 model offers a solution to the preliminary results of SNS in metastable helium, as well as the ability to address more complex questions such as the correlation of rotation and ellipticity noise and the effects of magnetic fields. We anticipate that in the future, the spin-one model can be used as a simplified model, similar to the spin 1/2 model, to explore novel phenomena in SNS.

This thesis is structured as follows.

1. Chapter 1 introduces the SNS experiment and presents the current state-of-the-art research in this field.

2. Chapter 2 reviews the metastable helium system and the primary measurement methods used throughout the thesis. We focus on the SNS of metastable helium near the transition line D_0 , where the level structure is the simplest.

3. In Chapter 3, we develop a simulation model to reproduce the experimental results. This simulation model serves as a guide for further research, and we use it to explore other transition lines, D_1 and D_2 and some simulation results in Chapter 5 and Chapter 6.

4. In Chapter 4, with sufficient experimental support and simulation results, we propose a spin-one model. This model successfully explains the experimental observations presented in Chapters 2, 4, 5, and 6.

5. In Chapters 5 and 6, we investigate the correlation between ellipticity and rotation noise, and the effect of magnetic field noise, respectively. Based on the simulation model developed in Chapter 3, we identify several interesting phenomena that require further experimental investigation. Additionally, we use the spin-one model introduced in Chapter 4 to interpret these simulation results, highlighting the potential applications of this model.

6. Finally, In chapter 7, I present the concluding remarks of this thesis.

Publications

1. Liu, S., Neveu, P., Delpy, J., Wu, E., Bretenaker, F., & Goldfarb, F. (2023). Spin-noise spectroscopy of a spin-one system. *Physical Review A*, 107(2), 023527.
2. Liu, S., Neveu, P., Delpy, J., Hemmen, L., Brion, E., Wu, E., ... & Goldfarb, F. (2022). Birefringence and dichroism effects in the spin noise spectra of a spin-1 system. *New Journal of Physics*, 24(11), 113047.
3. Liu, S., Neveu, P., Hemmen, L., Brion, E., Wu, E., Bretenaker, F., & Goldfarb, F. (2022, June). Spin noise spectroscopy of metastable helium. In *Quantum Technologies 2022* (p. PC1213307). SPIE.
4. Delpy, J., Liu, S., Neveu, P., Wu, E., Bretenaker, F., & Goldfarb, F. (2023). Spin-noise spectroscopy of optical light shifts. *Physical Review A*, 107(1), L011701.
5. Bian, Y., Liu, S., Zhang, Y., Liu, Y., Yang, X., Lou, S., ... & Jin, Q. (2021). Distance-Dependent plasmon-enhanced fluorescence of submonolayer rhodamine 6G by gold nanoparticles. *Nanoscale Research Letters*, 16(1), 1-7.
6. Neveu, P., Delpy, J., Liu, S., Banerjee, C., Lugani, J., Bretenaker, F., ... & Goldfarb, F. (2021). Generation of squeezed light vacuum enabled by coherent population trapping. *Optics Express*, 29(7), 10471-10479.
7. Bretenaker, F., Goldfarb, F., Liu, S., Neveu, P., & Brion, E. (2022, March). Quantum optics in a metastable helium vapor. In *Optical and Quantum Sensing and Precision Metrology II* (p. PC1201634). SPIE.
8. Pan, C., Ma, Q., Liu, S., Xue, Y., Fang, Z., Zhang, S., ... & Wu, B. (2022). Angularly anisotropic tunability of upconversion luminescence by tuning plasmonic local-field responses in gold nanorods antennae with different configurations. *Nanophotonics*, 11(10), 2349-2359.
9. Rong, Y., Ju, Z., Ma, Q., Liu, S., Pan, C., Wu, B., ... & Wu, E. (2020). Efficient generation of nitrogen vacancy centers by laser writing close to the diamond surface with a layer of silicon nanoballs. *New Journal of Physics*, 22(1), 013006.
10. Rong, Y., Cheng, K., Ju, Z., Pan, C., Ma, Q., Liu, S., ... & Jia, T. (2019). Bright near-surface silicon vacancy centers in diamond fabricated by femtosecond laser ablation. *Optics letters*, 44(15), 3793-3796.

Contents

1	Introduction and state-of-the art of spin noise spectroscopy	1
1.1	Probing a system with noise	2
1.2	Spin noise spectroscopy	3
1.2.1	SNS principle	3
1.2.2	Faraday rotation effect	4
1.2.3	Noise power spectrum and second order correlator	5
1.3	The development of SNS	6
1.3.1	First SNS experiment	6
1.3.2	New interests in SNS	6
1.3.2.1	Correlation of different spins	8
1.3.2.2	Spatial correlation of spins	8
1.3.2.3	Nonequilibrium SNS	9
1.3.2.4	Higher order correlators	9
2	SNS around the D_0 transition line of ^4He	11
2.1	Introduction	12
2.2	System and set up	12
2.2.1	Metastable helium	12
2.3	Polarization orientation noise	14
2.3.1	Set-up	14
2.3.2	Experimental results for the RND set-up	15

2.3.3	Background noise dependence	17
2.4	Ellipticity noise	18
2.4.1	Set-up	18
2.4.2	Results for ellipticity noise	19
2.5	Conclusion	20
3	Spin noise simulation model	23
3.1	Density matrix evolution	24
3.2	Noise operator	26
3.3	From atomic spin noise to probe noise	28
3.4	Comparison with experimental results	30
3.5	Conclusion	33
4	SNS around the D_1 and D_2 transition lines of ^4He	35
4.1	SNS results close to the D_1 and D_2 lines	35
4.2	Interpretation in terms of spin noise modes	38
4.2.1	Spin-1 noise decomposition	39
4.2.2	Time evolution	41
4.3	Probe noise	42
4.3.1	Probe noise modes near D_0 transition line	42
4.3.2	Oscillation frequencies of the modes	45
4.4	Cases of the D_1 and D_2 transitions	49
4.4.1	FR noise of the D_1 and D_2 transitions	49
4.4.2	Ellipticity noise of the D_1 and D_2 transitions	52
4.5	Conclusion	57
5	Correlation between FR noise and ellipticity noise	59
5.1	Definitions	60
5.1.1	Covariance	60
5.1.2	Correlator C_2	61
5.1.3	Magnitude square coherence	61

5.2	Correlation results	62
5.2.1	Case where $\theta = 0^\circ$	62
5.2.2	Case where $\theta = 45^\circ$	64
5.3	Interpretation of correlations in terms of spin noise modes	66
5.3.1	Weak correlation at $\theta = 0^\circ$	66
5.3.2	Strong correlation at $\theta = 45^\circ$	67
5.4	Proposed experiment	69
5.5	Conclusion	69
6	SNS in the presence of magnetic noise	73
6.1	Modeling the magnetic noise	74
6.1.1	Fluctuating Larmor frequency	75
6.1.2	SNS simulation in the presence of magnetic noise	75
6.2	Simulation results with varying noise bandwidth	77
6.3	Interpretation in terms of oscillation modes	77
6.4	Experimental Noise Calibration	80
6.5	Conclusion	81
7	Conclusion	83
Appendix A	Main results obtained in Faraday geometry	85
A.1	Introduction	85
A.2	Spin oscillation frequency in Faraday geometry	85
A.3	The evolution of the eight spin noise modes	87
A.4	Experimental results and simulations	88
Appendix B	The spin noise of spin $1/2$ system	91
B.1	Spin- $1/2$ system in a magnetic field	91
B.1.1	Spin- $1/2$ decomposition	92
B.1.2	Atom-photon coupling	93
B.1.3	Representation transformation	93

Appendix C Hamiltonien and dipole operator	97
C.1 Dipole operator near D_0, D_1, D_2	97
C.2 Hamiltonien of spin system.	100
C.3 Polarization of the system	101
Appendix D Operators in different basis	103
References	105

Chapter **1**

Introduction and state-of-the art of spin noise spectroscopy

Contents

1.1	Probing a system with noise	2
1.2	Spin noise spectroscopy	3
1.2.1	SNS principle	3
1.2.2	Faraday rotation effect	4
1.2.3	Noise power spectrum and second order correlator	5
1.3	The development of SNS	6
1.3.1	First SNS experiment	6
1.3.2	New interests in SNS	6

In this chapter, we provide several examples to illustrate the concept of probing systems with noise, which forms the fundamental idea behind spin noise spectroscopy (SNS). Subsequently, we describe a comprehensive experimental framework for SNS and explain the mechanism of Faraday rotation noise associated with SNS as well as the technique of using noise power spectrum to explore SNS. Finally, we introduce the latest breakthroughs in SNS development. This chapter will make us familiar with SNS and the state-of-the-art of current international research.

1.1 Probing a system with noise

Properties of materials in physics are studied most frequently by measuring their response to external excitation. However, this may dramatically change the features of the system, making the experimental results sometimes difficult to interpret. But there is another way to probe a system. In the absence of any external disturbance, the spontaneous noise of the system seems to be extremely useful. There are various fluctuations in different physical variables, such as electric current, pressure, magnetization, etc. Different variable noises can be related to different physical quantities of the system. For example, although the value of resistance R is typically obtained by applying a constant voltage V to the resistor and measuring the average electric current I , it can also be determined from voltage variance at thermodynamic equilibrium (the Johnson-Nyquist noise) without application of any external voltage, as demonstrated as early as 1928 [14, 15]. Indeed, according to the fluctuation-dissipation theorem, the voltage variance is given by [16, 17]

$$\langle V^2 \rangle = 4k_B T R \Delta f, \quad (1.1)$$

where k_B is the Boltzmann constant, T is temperature, the average is taken over many repeated measurements, and Δf is the bandwidth of the noise in Hz. Another striking historical example is the determination of star angular dimensions using correlations in light intensity fluctuations performed in 1956 [18].

Similarly, spin fluctuations of a paramagnetic system can also give information and be interesting to probe. Indeed, the noise originates from the coupling of the system with its environments and can be used as a probe of the interactions. This concept has a wide range of possible applications, including high-resolution imaging [19–23], non-invasive probing of quantum phase transitions in cold atoms [10, 24–26]. Spin noise spectroscopy (SNS) with its narrow spin noise peaks in the range of hundreds of kHz is suggested for precise magnetometry [27–29]. Improved sensitivity can be achieved through techniques like squeezed-light [30] or homodyne detection amplification [31, 32].

In this chapter, we first describe the general experimental scheme of SNS and the properties of the noise power spectrum. Then we introduce the development of SNS and its applicability.

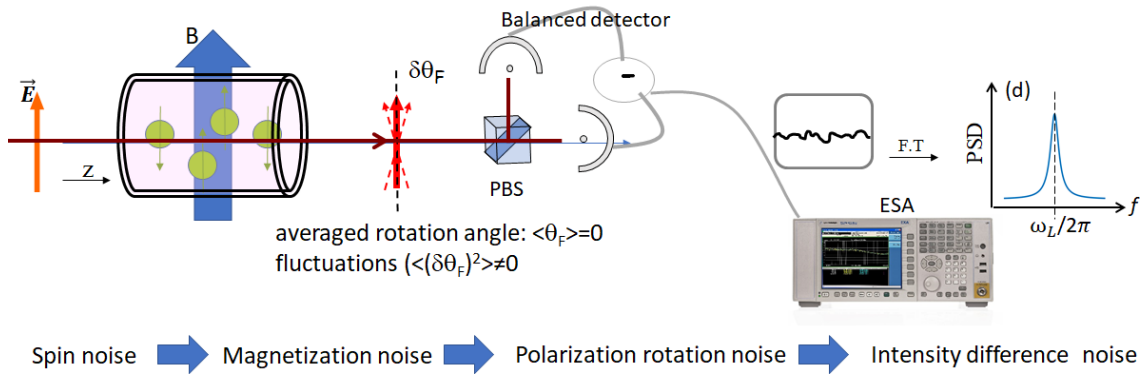


Figure 1.1: The principle of SNS. A linearly polarized probe beam experiences rotation noise passing through a medium with magnetization noise. The rotation noise becomes a light intensity difference between the two paths of the balanced detection. An electronic spectrum analyzer (ESA) is used to get the power spectrum density (PSD) of the noise signal.

1.2 Spin noise spectroscopy

Among spectroscopic techniques, the one that uses spin fluctuations as a signal is called spin noise spectroscopy. We first describe the typical experimental scheme of SNS, and then further explain the Faraday rotation (FR) effect, the associated circular birefringence (CB) effect, and the associated noise power spectrum.

1.2.1 SNS principle

A typical SNS experiment scheme is shown in Figure 1.1. The magnetization of a paramagnet can be detected with an optical method based on the Faraday rotation (FR) effect. A linearly polarized light beam will change polarization direction after passing through a medium with magnetization along the light propagation direction z . Although the average magnetization of the medium in thermal equilibrium is zero, it has spontaneous magnetization noise that results in some rotation noise for the probe. After a polarization beam splitter, this rotation noise becomes a light intensity difference between the two paths of a balanced detection. The corresponding power spectrum density (PSD) can be obtained through an electronic spectrum analyzer (ESA).

The power spectrum of spin noise, i.e. the Fourier transform of the correlation of the spin fluctuations, is centered at zero frequency where measurements are frequently impeded by technical noise. A transverse¹ magnetic field \mathbf{B} is introduced making the spins precess at the Larmor frequency ω_L . Then the center frequency of the spectra is shifted from zero to the Larmor frequency as shown in Fig. 1.1. This configuration is called Voigt geometry. On the other hand, some SNS experiments also choose the Faraday geometry:

¹Perpendicular to the direction of the detected magnetization z .

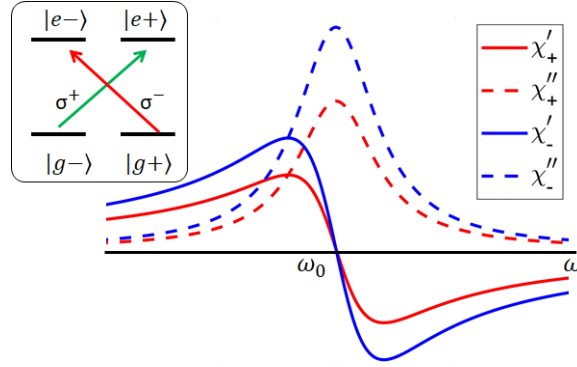


Figure 1.2: Real χ'_{\pm} and imaginary χ''_{\pm} parts of the dielectric susceptibility as function of frequency near resonance. The sign \pm means the left and right circular components. The inset is a schematic to show the simple physical picture to interpret the Faraday rotation effect. The two circular components have different interaction strengths with the system due to the unequal populations of the ground sublevels.

the magnetic field is oriented along the light propagation direction. The details of the Faraday geometry and some corresponding experimental results are given in Appendix A.

1.2.2 Faraday rotation effect

Here we give a simple physical picture of the FR effect in a paramagnetic system. As described in Figure 1.2, the real and imaginary parts of the medium susceptibility χ , which correspond to the dispersion and absorption of the medium respectively, are linked by the Kramers-Kronig relation. In the framework of the Lorentz model, they read:

$$\chi' = \frac{Nq^2(\omega_0 - \omega)}{2\omega_0\epsilon_0m[(\omega_0 - \omega)^2 + \gamma^2]}, \quad (1.2)$$

$$\chi'' = \frac{Nq^2\gamma}{2\omega_0\epsilon_0m[(\omega_0 - \omega)^2 + \gamma^2]}, \quad (1.3)$$

where N is the total number of atoms, $q = 1.6 \times 10^{-19}\text{C}$, γ is the damping coefficient of the electron motion, and m is the mass of the electron.

Let us consider a transverse wave that propagates along z and is linearly polarized in the xy plane:

$$\mathbf{E}(\theta) = E \cos(\theta)\mathbf{x} + E \sin(\theta)\mathbf{y} = (Ee^{i\theta}\boldsymbol{\sigma}^+ + Ee^{-i\theta}\boldsymbol{\sigma}^-)/\sqrt{2}, \quad (1.4)$$

where θ indicates the polarization direction. This probe can be written in linear x/y or circular $\boldsymbol{\sigma}^{\pm}$ basis.

Let us suppose that the populations of the ground Zeeman sublevels $|g-\rangle, |g+\rangle$ are different. This results in different dispersion coefficients χ'_{\pm} of the two circular components

σ^\pm of the probe. Then the angle θ will change when there is a relative phase difference between the two circular components. Assume that the phase of the σ^- component leads σ^+ by ϕ , then the outgoing probe becomes

$$\mathbf{E}_{out} = (Ee^{i\theta}\sigma^+ + Ee^{-i\theta}e^{i\phi}\sigma^-)/\sqrt{2}. \quad (1.5)$$

Neglecting the overall phase factor $e^{i\frac{\phi}{2}}$, one obtains

$$\mathbf{E}_{out} = (Ee^{i(\theta-\frac{\phi}{2})}\sigma^+ + Ee^{-i(\theta-\frac{\phi}{2})}\sigma^-)/\sqrt{2} = \mathbf{E}(\theta - \phi/2). \quad (1.6)$$

The rotation angle is $-\phi/2$ and is independent of θ . This phenomenon is also named as magnetic circular birefringence (CB) effect. For the medium with only CB, the induced rotation is constant for all values of θ for a given spin fluctuation.

This CB effect depends on the relative detuning between the light and the optical resonance of the medium. As shown in Fig. 1.2, near the edge of the absorption band, where the FR experiments are usually performed, the refractive indices of the two circular components are maximum for a given population difference. Naturally, we can predict that when light and matter resonate, the absorption of the medium is stronger. In this case, the population difference mainly causes some absorption difference of σ^\pm components and circular dichroism (CD) is dominant.

1.2.3 Noise power spectrum and second order correlator

We have explained the principle of an SNS experiment. The magnetization noise is transformed into probe polarization noise via the Faraday rotation effect. In this section, leaving those technical details aside, and going back to our spin system, we explain what properties of the spin system we can probe when we look at the noise power spectrum.

For the spin system, we define the real number $S_z(t)$ as the projection along z of the spin of the ensemble. The spin fluctuation is

$$\delta S_z(t) = S_z(t) - \langle S_z(t) \rangle. \quad (1.7)$$

Considering the equilibrium state of the spin ensemble at room temperature, the populations of Zeeman sublevels are equally distributed. Therefore, the average spin is zero $\langle S_z \rangle = 0$. The Fourier transform of the recorded spin trajectory $S_z(t)$ during the measurement interval T_m is defined as follows:

$$a(\omega) = \frac{1}{\sqrt{T_m}} \int_0^{T_m} dt e^{i\omega t} S_z(t). \quad (1.8)$$

We assume that $T_m \gg \tau_s$, where τ_s is the relaxation time of spins. As $S_z(t)$ is real, one has $a(-\omega) = a^*(\omega)$. For such a stochastic noise signal, the statistic average $\langle a(\omega) \rangle = 0$. The most useful property in the frequency domain is the noise power spectrum, which is defined as

$$C_2(\omega) = \langle |a(\omega)|^2 \rangle. \quad (1.9)$$

The noise power spectrum also has some physical meaning, i.e. the power density of the noise at frequency ω . In the experiment, power spectrum density (PSD) can be easily obtained using an ESA.

According to the *Wiener – Khinchine* theorem, the noise power spectrum carries the same information as the second order correlator. The spin-spin 2nd order correlator is defined as [33]:

$$\langle S_z(t_2) S_z(t_1) \rangle. \quad (1.10)$$

Considering a stationary stochastic process, the auto-correlation depends only on the time difference $t_2 - t_1$. The noise power spectrum is the Fourier transform of the auto correlation function.

$$C_2(\omega) = 2 \int_0^{\infty} dt \cos(\omega t) \langle S_z(t) S_z(0) \rangle \quad (1.11)$$

As a result, the spin dynamics information, such as the spin lifetime τ_s , noise intensity, and Larmor frequency, can be easily derived from the spectrum on account of the information equivalence of noise power spectrum and 2nd order correlation.

1.3 The development of SNS

I will first give a brief introduction about the first SNS experiments and then provide a quick overview of many key study directions around the world over the last decade.

1.3.1 First SNS experiment

The first experimental effort was initially reported in the early 1980s by Aleksandrov and Zapasskii [34] (Figure 1.3). The magnetic resonance of sodium atoms is observed in the fluctuation spectrum instead of measuring the conventional magnetic polarization of the medium. As there was no spectra analyser, they observed the signal resonance at a pre-selected frequency (1.3 MHz) by scanning the amplitude of the applied magnetic field. When the Larmor frequency corresponds to the selected one, the noise signal is amplified and can be seen. This research uses some optical frequency to probe the system instead of the radio frequency used in electronic paramagnetic resonance. And one should notice that here the applied B-field is weak and present only to shift the center frequency to several MHz. The medium can be considered as in a thermal equilibrium state. This is very different from the external B-field used to polarize the medium in electronic paramagnetic resonance.

1.3.2 New interests in SNS

At the time of Alexandrov and Zapaskii's first paper, it was debatable whether or not exceedingly faint noise signals were beneficial. SNS has seen a renewed interest in the past 20

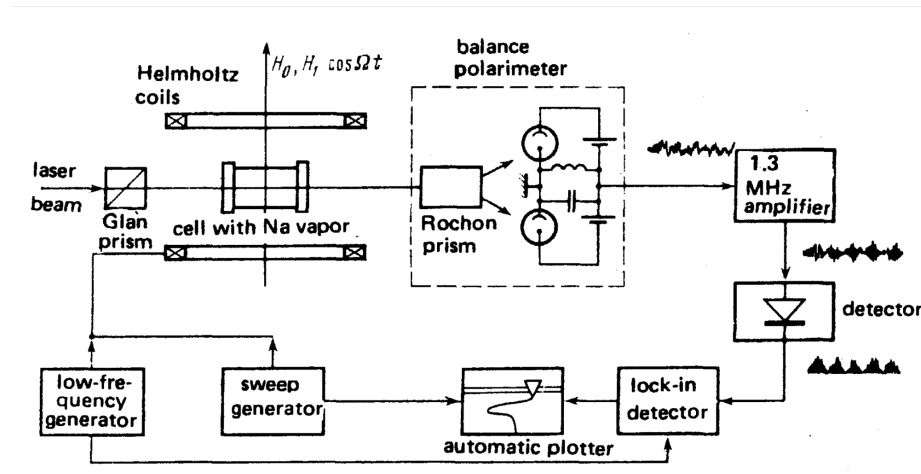


Figure 1.3: First SNS experiment [34]. The magnitude of the applied magnetic field is scanned and the noise signal is detected if the applied magnetic field provides a Larmor frequency close to 1.3 MHz.

years, due to advances in narrow linewidth lasers and developments in low noise electronics required for spectrum analysis: second order (and higher order) correlators of atomic spin fluctuations were shown to give access to classical (and purely quantum) signatures of the interaction of the system with its environment. The work in [2] is the reason for the interest in spin noise research today. Crooker et al. first demonstrated the access to information such as g-factor, isotope abundance ratio, hyperfine structures, and spin relaxation time of Rb and K vapor. Those data were quantitatively obtained purely from thermal fluctuations rather than traditional methods, which require the polarization of the medium. Although the work of Crooker in 2004 [35] only demonstrates the same capability of SNS as traditional detection methods, its weak perturbation property attracted attention [36–38]. Beyond the atomic vapor system, SNS was then used to probe different properties of various media such as semiconductors [4] or quantum wells [39] [6] and crystals [40]. In these cases, SNS can be employed to study the anisotropy of the dephasing time in the samples. Furthermore, the observation of spin noise in cold atoms, where quantum effects are more readily observable, can be highly intriguing. This approach is expected to have practical implications in understanding quantum phases [24] and precision magnetometry [27, 29]. However, the observation is challenging due to the exceedingly weak noise. Spin noise measurement of cold atoms has been reported through coherent Raman drive recently [41]. These notable advancements serve to underscore the potential application scenarios of SNS.

In terms of noise type of the probe, apart from the polarization rotation noise, people also consider the ellipticity noise of the linearly polarized probe [42, 43] or the intensity of the circularly polarized probe [44]. The way of performing the measurements mainly depends on how the spin noise affects the probe light. In the following chapters, through SNS of metastable helium, we will demonstrate the necessity and completeness of detecting both rotation and ellipticity noises for a high-spin system.

In the following, I will introduce some other works including the correlation of different spins, spatial correlation of spins, nonequilibrium SNS, and higher order correlators. These works illustrate the potential of SNS.

1.3.2.1 Correlation of different spins

We have seen that the essence of the noise spectrum analysis lies in the correlations of the fluctuating variables in the thermal environment. From the perspective of whether two physical quantities are correlated, we can obtain a lot of information.

According to a work published in 2013 [45], the optical spectroscopy of spin noise in certain circumstances can have higher resolution than traditional linear optics. The spins belonging to the same or different transitions have a strong correlation or no correlation leading the spin noises to have different optical spectroscopy patterns. Here the authors pay attention to whether the transition channels are independent and design a SNS experiment to verify it. They also point out that the correlations between the spins can also reveal the type of broadening of absorption lines. Immediately after, Yang et al [46] demonstrated SNS experiment in InGaAS quantum dots with two independent lasers with different and controllable frequencies. The cross spectra of the two probes show the correlations between the corresponding detected spins of the two probes. These cross spectra successfully show the homogeneous broadening width in a medium with strong inhomogeneous broadening. Here the authors exploit the independence of the probe noise from different spins with different velocity groups. Furthermore, in the work of Roy et al [10], two beam SNS is used to investigate the spin interaction between different species, namely Rb and Cs vapors. They successfully observed the spin exchanges between Rb and Cs atoms in the cross spectra of the two corresponding probes. It is important to note that the information mentioned above is typically acquired by nonlinear optics experiments like four-wave mixing, photon echo, and spectral hole burning [47–49].

1.3.2.2 Spatial correlation of spins

Naturally, apart from the correlation information in the time domain, the spatial correlation contains a lot of information. Generally, in SNS, all spatial information is supposed to be irreparably lost since the polarization noise of the probe is a weighted average of the spin ensemble over the probe beam.

However, it has been proved that SNS can show prospects in three-dimensional tomography [50]. When using Z-scan, which is typically employed to detect optical nonlinearity [51, 52], the noise power displays a peak that is centered at the location of the focus point of the probe. This is caused by the fact that spin noise power is inversely proportional to the beam area of the probe [5, 53, 54]. Two-beam SNS is practical in the spatial correlation study of spins. When the two beams overlap in space, the two independent beams can show cross correlations as the noise of the two beams may come from the same spin fluctuations. Furthermore, when the spins contributing to the detected noise are not localized, beams can

show correlations even if they are spatially separated. This kind of method, as proposed in [55], can be used to study spin transport. In [56], the authors propose a method to probe the spatiotemporal spin noise through the homodyne mixing of a local oscillator and the scattered light noise. By modulating the path of LO, part of the probe noise is selectively amplified, which encodes the information on the spatial spin noise.

1.3.2.3 Nonequilibrium SNS

The fluctuation-dissipation theorem tells us that the information we can obtain from the noise of the system in thermal environments is constrained by the linear response function of the system. However, SNS has been found to offer real advantages over traditional detection techniques when breaking the equilibrium with the environment.

For example, theoretically, Li et al. [57] demonstrate that by adding a mild ac electric field to the sample, SNS may be used to quantify the spin-orbit coupling anisotropy and separate spin noise from the conducting and localized electrons of the sample. In the work of Glaserapp et al. [58], a weak RF magnetic field is introduced to modulate the spin fluctuations of the Zeeman sub-levels. The RF magnetic field resonance with the energy levels reveals how the sub-levels couple to each other via the stochastic spin fluctuations without polarizing the system. Furthermore, when the amplitude of the off-resonant RF magnetic field increases, they observe the ac Zeeman effect. Using optical pumping to alter the population distribution of the hyperfine levels, researchers discover that SNS can identify spectral lines with greater resolution than conventional absorption spectroscopy in the presence of a variety of spectral widening mechanisms [59]. The nonequilibrium SNS in quantum dots [60, 61] shows that it can be used to quantitatively describe the excitation and recombination dynamics of the carriers. Excitingly, we have also recently observed the ac Stark effect in nonequilibrium SNS with a relatively strong probe [13].

1.3.2.4 Higher order correlators

The 2nd order correlator carries information regarding spin dynamics but does not always fully characterize them. A simple example to illustrate this situation is that the noise spectrum only contains the values of different frequency components and it cannot determine whether one frequency has any relation with the other ones. Indeed, people already construct higher order correlations to extract information beyond the limit of the fluctuation-dissipation theorem [62]. Spin dynamics information different from the average linear response properties of spin systems can be studied by analyzing higher-order statistics [63–65], such as bispectrum used to investigate the correlation between different frequency components [66]. Furthermore, high order correlators allow one to distinguish between homogeneous and inhomogeneous broadening of the spin resonances (spin dephasing and decoherence time) [67, 68] and study the property of the reservoir, which leads to spin relaxation [58, 69]. It has also been realized that high order correlators are a powerful tool to study the so-called phase transition at fluctuating levels [63, 70, 71].

Firstly, we give the formalism of high order correlators. The n th order correlator is defined as [69]

$$\langle S_z(t_1)S_z(t_2) \cdots S_z(t_n) \rangle. \quad (1.12)$$

According to Refs [72, 73], it is easier to investigate the cumulants for a collection of independent spins ensembles than the correlation function of Eq. (1.12). And for a signal obeying time-reversal symmetry with $\langle S_z(t) \rangle = 0$, all odd-order correlators are zero [62]. The specific formalism of the higher order cumulants can be found in [69]. Here we limit ourselves to the simplest illustration of a spectrum of the high order cumulants named bispectrum, which is a section of the Fourier transform of fourth order cumulants. The bispectrum depicts the 'correlation' between spin noise components at two frequencies and reads

$$C_4(\omega_1, \omega_2) \equiv \langle |a(\omega_1)|^2 |a(\omega_2)|^2 \rangle - \langle |a(\omega_1)|^2 \rangle \langle |a(\omega_2)|^2 \rangle, \quad \omega_1 \neq \omega_2. \quad (1.13)$$

A positive or negative value of $C_4(\omega_1, \omega_2)$ indicates a correlation or anti-correlation between two frequencies, which indicates that observing a strong signal at one frequency means another frequency may be boosted or suppressed respectively. A picture of the experimental measurement of the bispectrum has been demonstrated in [66].

Then we have to emphasize that any high order correlator for a Gaussian noise S_z is zero. The second order correlator can fully describe a Gaussian fluctuation. Indeed, one of the prerequisites of the definition of various higher order cumulants is that such cumulants should be zero for Gaussian fluctuations [33]. However, the study of higher-order spin correlations has been hampered by the fact that the noise of a system composed of a large number of spins is Gaussian, as constrained by the central limit theorem. Nevertheless, this can be resolved by decreasing the number of spins at the price of an even weaker signal. From this point of view, a nano thin cell with much fewer spins is a promising direction to study high order correlators. Recently, the extreme limit case of a single spin noise of a heavy hole localized in (InGa)As quantum dot has been successfully observed by SNS [74], which has again sparked interest in high order correlations. The other difficulties of the measurement of higher order correlation include the relatively long measurement time compared with the relaxation time of spin and the fluctuating probe intensity [62]. Several methods to study high order correlations by SNS have been provided including the study of ferromagnetic ensemble which has strongly interacting spins, low-temperature SNS [62], and 'stimulated' spin noise in an activated crystal [75].

Chapter 2

SNS around the D_0 transition line of ^4He

Contents

2.1	Introduction	12
2.2	System and set up	12
2.2.1	Metastable helium	12
2.3	Polarization orientation noise	14
2.3.1	Set-up	14
2.3.2	Experimental results for the RND set-up	15
2.3.3	Background noise dependence	17
2.4	Ellipticity noise	18
2.4.1	Set-up	18
2.4.2	Results for ellipticity noise	19
2.5	Conclusion	20

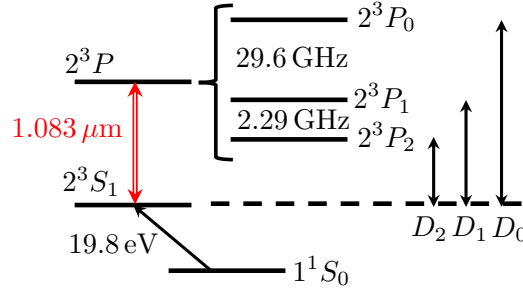


Figure 2.1: Level structure of ${}^4\text{He}$. The three transitions D_0 , D_1 , and D_2 from the metastable 2^3S_1 level are well separated, by a difference larger than the Doppler broadening at room temperature.

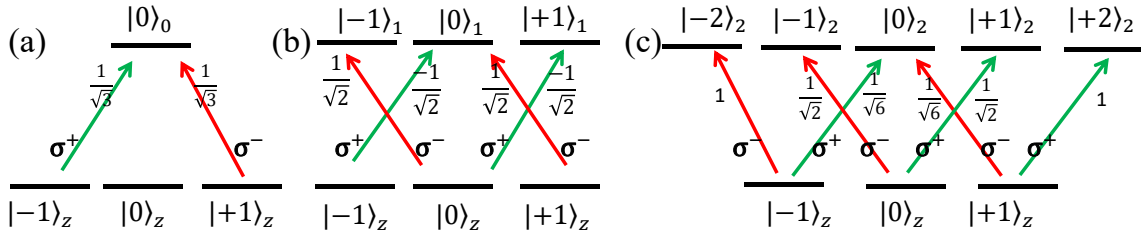


Figure 2.2: The level structure of the D_0 (a), D_1 (b) and D_2 (c) lines. The three lines have the same ground levels but different upper levels with an increasing number of sublevels.

2.1 Introduction

This chapter introduces metastable helium, i.e. the experimental object of my entire thesis, and the basic experimental set-up of SNS. We provide the SNS pattern in metastable helium for different detuning of the probe and different polarization directions of the probe. These are the most fundamental experimental results of this thesis. We identify the two main types of noise that are studied throughout this thesis.

2.2 System and set up

2.2.1 Metastable helium

Metastable ${}^4\text{He}$ has the advantage of being a very simple system. Contrary to alkali atoms, without any nuclear spin, it does not have any hyperfine structure. The $|2^3S_1\rangle \leftrightarrow |2^3P\rangle$ transition of metastable helium has only three absorption lines separated by a frequency difference larger than the 0.8 GHz room temperature Doppler broadening [76], as shown in Fig. 2.1.

The triplet 2^3S_1 is 19.8 eV above the ground state of helium. The helium gas-cell is

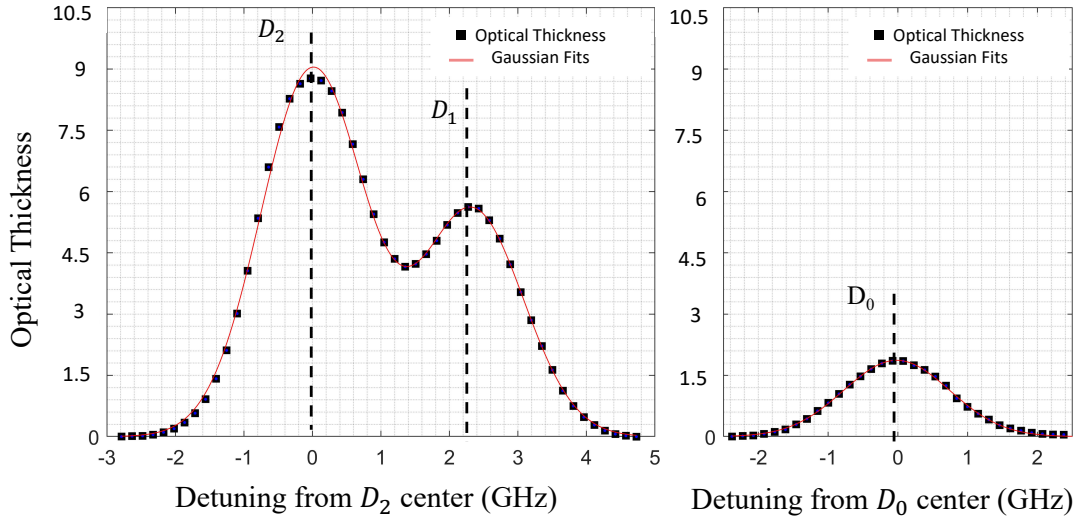


Figure 2.3: Optical thickness near three transition lines. The input power is 0.1 mW with a 1.5 cm beam diameter to limit saturation. Black dots: experimental data. Red line: Gaussian fits.

surrounded by 2 electrodes providing a radio frequency discharge at 27 MHz. The discharge creates a plasma, which is used to excite the helium atoms from the ground state to the triplet 2^3S_1 . The transition between 2^3S_1 with spin one ($S = 1$) to 1^1S_0 with spin zero ($S = 0$) is optical forbidden on account of moment conservation. As a result, the atoms at state 2^3S_1 , named metastable helium, have a long lifetime of around 8000 s [77]. The $|2^3S_1\rangle$ metastable state has three Zeeman sublevels, with a ± 2.8 MHz/Gauss Zeeman shift for the $m = \pm 1$ sublevels, respectively. We could create a density of $\sim 10^{11}\text{cm}^{-3}$ compared to the density $\sim 10^{17}\text{cm}^{-3}$ of the ground state helium atoms which act as a buffer gas. There are collisions between the buffer gas and the metastable helium leading in frequent velocity changes of the metastable helium atoms. Considering that the interaction timescale between atoms and the probe is much larger than the characteristic time between the collisions, the inhomogeneous broadening due to the Doppler effect of the ensemble will be 'homogenized' as each atom can experience many different velocity classes within Doppler profile in a short time due to frequent collisions. This approximation is well verified by the electromagnetically induced transparency observation in helium [76].

The 2^3P state is split into 3 fine structure levels with $J = 0, 1, 2$, which respectively constitute the D_0, D_1, D_2 transition lines. The three lines have the same ground Zeeman sublevels but an increasing number of upper sublevels due to the increasing total angular momentum as shown in Fig. 2.2.

The optical thickness of the different lines is shown in Fig. 2.3. In the SNS experiment of this chapter, we choose to blue detune the frequency of the probe beam from the D_0 line to probe this transition in a purely dispersive and non-perturbative manner without being significantly disturbed by the influence of the two other lines. The goal of the present

chapter is thus to explore the properties of the SNS in this relatively pure and simple closed $J = 1 \rightarrow J = 0$ atomic transition, in order to put into evidence the peculiarities of spin noise in the case of a spin 1 system like the $|2^3S_1\rangle$ state. The more complex cases such as near D_1, D_2 are investigated in the following chapters.

2.3 Polarization orientation noise

2.3.1 Set-up

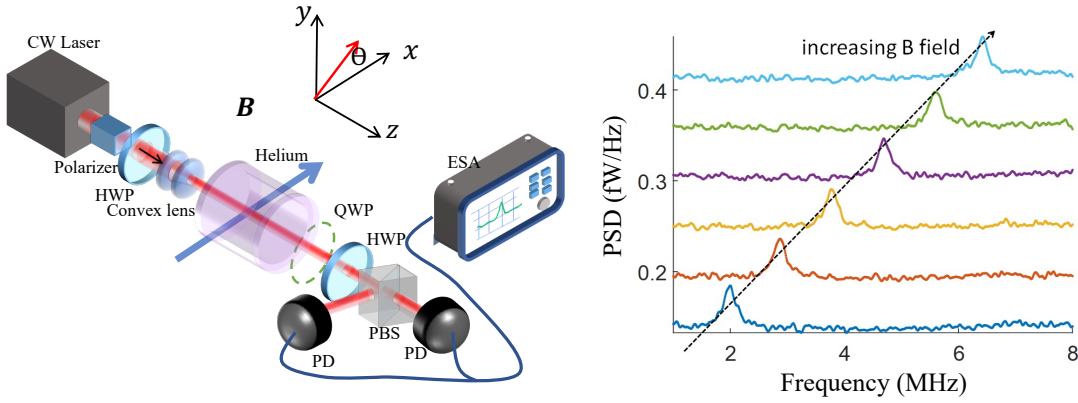


Figure 2.4: Left: experimental set-up: rotation noise detection (RND): a half-wave plate (HWP) allows to have an equal average intensity on both photodiodes (PD). Ellipticity noise detection (END) : a quarter-wave plate (QWP) is added just after the cell to record the ellipticity noise. The zero frequency noise resonance is shifted by a transverse DC magnetic field so that the noise peak is detected around the Larmor frequency ω_L . Right: experimental data recorded with an electrical spectrum analyzer (ESA) for different magnetic fields in the case of the RND, for an angle $\theta = 0^\circ$ between the input linear polarization and the magnetic field: one resonance is visible at the Larmor frequency ω_L . Arbitrary offsets are added for better visibility.

Figure 2.4 shows a schematic of the experimental setup. A linearly polarized laser beam at $1.083 \mu\text{m}$, corresponding to the $|2^3S_1\rangle \leftrightarrow |2^3P\rangle$ optical transitions, is sent into a cell filled with 1 Torr of ^4He at room temperature. With a diameter of about 0.6 mm and 1 mW power, the corresponding Rabi frequency is about 40 MHz.

While propagating inside the helium cell, the laser polarization experiences some random Faraday rotation induced by random fluctuations of the populations of the three Zeeman ground state sublevels. A transverse DC magnetic field is added to the atoms to shift the spin noise resonance to the Larmor frequency ω_L [9, 78]. This B-field is created by two rectangular coils, whose dimensions are much larger than the cell so that it can be

considered as homogeneous inside the sample. The relative angle between this magnetic field and the incident polarization direction of the probe beam is denoted as θ .

After the cell, a half-wave plate (HWP) followed by a polarizing beamsplitter (PBS) allows to get an equal average intensity on the two photodiodes of a balanced detection, so that their signal difference is zero on average and non-zero when the polarization direction deviates from its initial direction. This corresponds to fluctuations of the orientation of a linearly polarized field, which we can call *Faraday rotation* (FR) noise. And we call the corresponding set-up as rotation noise detection (RND). On the other hand, ellipticity noise detection (END) with one extra quarter-wave plate will be described later.

The associated noise power spectral density can then be recorded using an electrical spectrum analyzer (ESA). To describe the balanced detection scheme, the output field complex amplitude can be written as the sum of a mean value \mathbf{E} and a fluctuating part $\mathbf{e}(t)$:

$$\mathbf{E}_{\text{out}}(t) = \mathbf{E} + \mathbf{e}(t) , \quad (2.1)$$

where \mathbf{E} is assumed to be real, and the vectorial fluctuations $\mathbf{e}(t)$ can consist in amplitude, phase or polarization variations, which carry the spin noise information. After the HWP, the field sent to the balanced detection has an average polarization at 45° of the polarizing beamsplitter axes \mathbf{x} and \mathbf{y} :

$$\mathbf{E}_{\text{out}}(t) = \frac{1}{\sqrt{2}} \left[(E + e_{\parallel}(t) + e_{\perp}(t)) \mathbf{x} + (E + e_{\parallel}(t) - e_{\perp}(t)) \mathbf{y} \right] . \quad (2.2)$$

where $e_{\parallel}(t)$ and $e_{\perp}(t)$ are the components of $\mathbf{e}(t)$, which are parallel and perpendicular to \mathbf{E} , respectively, and E is the amplitude of \mathbf{E} , supposed to be real. The signal at the output of the balanced detection is thus proportional to:

$$\begin{aligned} D &= |\mathbf{E}_{\text{out}}(t) \cdot \mathbf{x}|^2 - |\mathbf{E}_{\text{out}}(t) \cdot \mathbf{y}|^2 \\ &= 2E \operatorname{Re}(e_{\perp}(t)) + \mathcal{O}(\mathbf{e}(t)^2) . \end{aligned} \quad (2.3)$$

The ESA thus records the power spectral density (PSD) of the field fluctuations polarized orthogonally to the mean output field, and in phase with it. This first order calculation remains valid in the case of a mean field with a small ellipticity. Figure 2.4 shows examples of experimental noise spectra obtained for increasing transverse magnetic field values, in the case of a 1.5 mW probe laser blue detuned by 1.5 GHz: the spin noise resonance frequency, which is centered on the corresponding Larmor frequency, increases with the magnetic field value.

2.3.2 Experimental results for the RND set-up

Generally, SNS is performed far away from resonance where the absorption is negligible, to avoid disturbing the system. But remaining far from resonance can be difficult in systems exhibiting large inhomogeneous broadening, and some groups already investigated

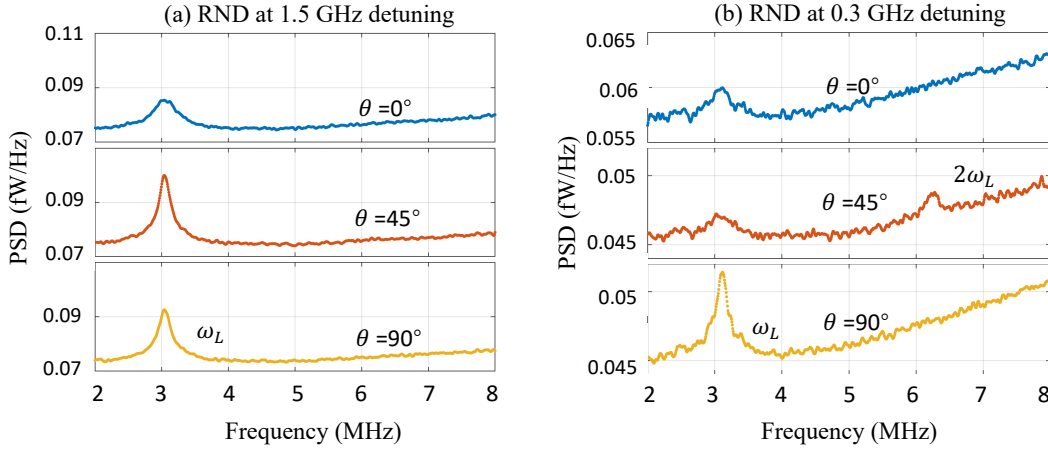


Figure 2.5: Experimental spectra obtained for $\theta = 0^\circ$, 45° and 90° in the case of (a) the RND set-up and an optical detuning 1.5 GHz; (b) the RND set-up and 0.3 GHz. The laser input power is about 1 mW.

the effect of small optical detunings [79, 80]. In such conditions, absorption cannot be ignored. Here the rotation noise of the probe is investigated both far from and near resonance. Figure 2.5 shows examples of experimental noise in the case of a 1 mW probe laser blue detuned by 1.5 GHz and 0.3 GHz with $\theta = 0^\circ, 45^\circ, 90^\circ$. While strongly detuned (Fig. 2.5(a)), a standard SNS result is obtained: one noise resonance at the Larmor frequency with small variations for different polarization directions of the probe θ^1 . Surprisingly, when the probe is closer to resonance (Fig. 2.5(b)), SNS shows some strong polarization θ dependence. Furthermore, we see that there are now two spin noise resonances, at the Larmor frequency ω_L and at $2\omega_L$.

The traditional SNS result at 1.5 GHz detuning can be well explained in view of circular birefringence (CB) effect. Differently, when the probe frequency is closer to resonance, birefringence effects become negligible compared to dichroism, so the behavior of the SNS resonance may change. Considering the polarization θ dependence and the type of the recorded noise (rotation noise), RND spectra at 0.3 GHz detuning are supposed to be linear dichroism (LD) noise effect with different eigenfrequency ω_L or $2\omega_L$ and different neutral axis². However, fully explaining this phenomenon requires more theoretical analysis, which will be in later chapters.

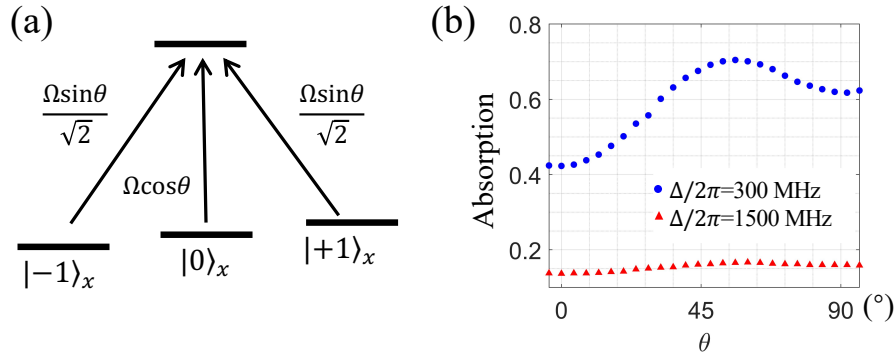


Figure 2.6: (a) Transitions of the ${}^3S_1 \rightarrow {}^3P_0$ line, and their excitations by an electric field, which makes an angle θ with respect to the quantization axis x and has a corresponding total Rabi frequency Ω . (b) Experimental measurements of the absorption of a 1 mW probe for a detuning of 1.5 GHz (red triangles) and 300 MHz (blue circles).

2.3.3 Background noise dependence

It is also worth noticing that the signal becomes much smaller when the detuning is reduced, because of the absorption that decreases the power reaching the detector. This explains why the detector background noise, which increases with the frequency, becomes much more visible in Fig. 2.5(b) compared with (a).

It can also be noticed by comparing for example the different spectra in Fig. 2.5(b) that the noise floor at $\theta = 0^\circ$ is larger than at $\theta = 45^\circ$ and 90° . This is because the detected power depends on θ , because the transverse magnetic field \mathbf{B} makes the vapor transmission dependent on the incident polarization direction. Indeed, Figure 2.6(b) reproduces measurements of the evolution of the cell absorption versus θ , clearly evidencing this effect. The dependence of the cell absorption on θ can be easily understood if one uses a quantization axis along \mathbf{B} : Figure 2.6(a) shows the transitions induced by a light beam linearly polarized at an angle θ with respect to the quantization axis x , from the sublevels $| -1 \rangle$, $| 0 \rangle$, $| +1 \rangle$ of the level 3S_1 to level 3P_0 . At $\theta = 0^\circ$, the only probed transition is $| m_x = 0 \rangle \leftrightarrow | m_x = 0 \rangle$, which leads to a strong optical pumping of the atoms to the $| m_x = \pm 1 \rangle$ sublevels and an increased transmission. For $\theta = 55^\circ$ the three transitions see equal Rabi frequencies, so that the absorption is maximum.

¹The small power difference can come from optical pumping effects when the power of the probe is not weak enough.

²When the polarization direction θ along the neutral axis, LD effect does not lead a difference in the amplitude of the two linearly polarized components of the linearly polarized light.

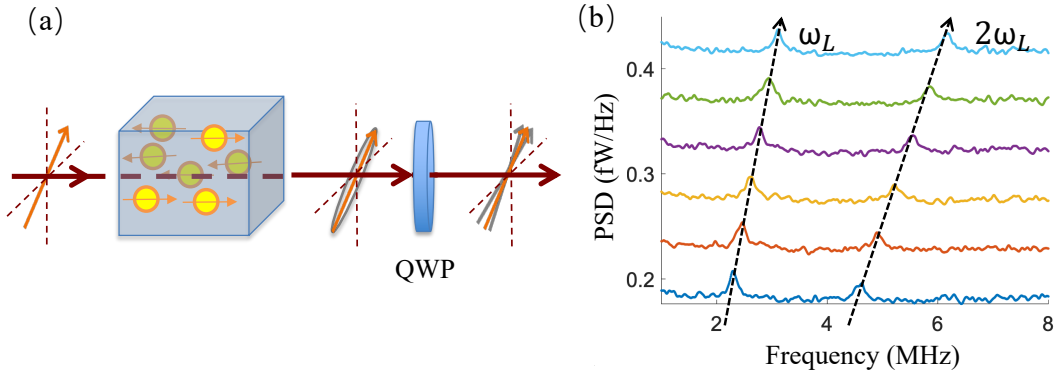


Figure 2.7: (a) Schematic of ellipticity noise detection (END). A quarter wave plate (QWP) is added after the cell to convert the rotation noise to ellipticity noise. (b) Experimental data recorded with an electrical spectrum analyzer (ESA) for different magnetic fields in the case of END, for an angle $\theta = 55^\circ$ between the input linear polarization and the magnetic field: two resonances are then visible, at ω_L and $2\omega_L$. Arbitrary offsets are added for a better visibility.

2.4 Ellipticity noise

The real and imaginary parts of the dielectric susceptibility χ , which describe the medium dispersion and absorption, obey the Kramers-Kronig relation. As a result, birefringence and dichroism effects come in pairs.

Based on the rotation noise from the previous section, our system exhibits circular birefringence and linear dichroism. And we can expect that it should have circular dichroism (CD) and linear birefringence (LB). Different from CB and LD leading to the rotation, CD and LB make the probe change from linear to elliptical polarization. In SNS, CD and LB noises manifest themselves as *ellipticity noise* of the probe.

2.4.1 Set-up

Ellipticity fluctuations are monitored by inserting a quarter-wave plate (QWP) just after the cell, as shown in Fig. 2.7(a). While Fomin & al [42] used a circularly polarized input beam, we choose to orient the QWP to transform an input elliptic polarization into a linear one by optimizing the fast axis of the QWP. The ellipticity noise is then changed into rotation noise, which can be detected with the same set-up as before.

Similarly, the recorded ellipticity noise can be written in terms of the small fluctuation part $e(t)$. The QWP induces a $\pi/2$ phase shift on the fluctuations along the y axis so that,

when the average ellipticity is small and can be neglected, Eq. (2.2) must be replaced by:

$$\mathbf{E}_{\text{out}}(t) = \frac{1}{\sqrt{2}} \left[(E + e_{\parallel}(t) + ie_{\perp}(t)) \mathbf{x} + (E + e_{\parallel}(t) - ie_{\perp}(t)) \mathbf{y} \right]. \quad (2.4)$$

Consequently, the signal analyzed by the ESA becomes:

$$D = 2E \text{Im}(e_{\perp}(t)) + \mathcal{O}(\mathbf{e}(t)^2). \quad (2.5)$$

In the following, we call this setup the ellipticity noise detection (END) setup, while the preceding one is called the rotation noise detection (RND) setup. These two setups correspond to the two limiting cases explored in [32], where the relative phase between the local oscillator and the signal can be continuously tuned: the balanced detection plays the role of a homodyne detector in which the local oscillator is provided by the mean field E and the role of the signal is played by the fluctuations e_{\perp} . One can choose between the two signal quadratures by adding or not the QWP as shown in Fig. 2.7 (a). It should be noted that we always check that the wave plate is oriented so that the average output polarization is linear and the detection properly balanced.

Fig. 2.7 (b) shows examples of experimental noise spectra obtained with this END setup for increasing transverse magnetic field values with $\theta = 55^\circ$, in the case of a 1.5 mW probe laser blue detuned by 1.5 GHz : there are now two spin noise resonances, at the Larmor frequency ω_L and at $2\omega_L$. It shows that for some θ , the spin noise centered at $2\omega_L$ resonance is visible in END at large detuning.

2.4.2 Results for ellipticity noise

Figure 2.8 shows examples of ellipticity noise in the case of a 1 mW probe laser blue detuned by 1.5 GHz and 0.3 GHz with values of $\theta = 0^\circ, 45^\circ, 90^\circ$. Contrary to the rotation noise, we find that there are now two spin noise resonances for a strongly detuned probe (Fig. 2.8(a)), at the Larmor frequency ω_L and at $2\omega_L$. They exhibit a strong polarization θ dependence. Near resonance (Fig. 2.8(b)), only the ω_L resonance is observed without any obvious polarization dependence.

We then perform a full scan of the dependence of the intensities of the rotation and ellipticity noise peaks as a function of θ with four different optical detunings Δ of the probe beam with respect to the center of the Doppler broadening, which is shown in Figure 2.9. The results of Fig. 2.9 (with removed background noise) clearly show that the polarization dependence of the RND and END spectra have reversed their behaviors close to resonance with respect to the far detuned case. Indeed, the RND noise peaks near resonance ($\Delta/2\pi = 300$ MHz) now exhibit a strong θ dependence, while the END noise peak amplitude becomes almost independent of the polarization.

This exchange between the END and RND behaviors at large and small optical detunings is well explained by the fact that dispersive effects dominate at large detunings

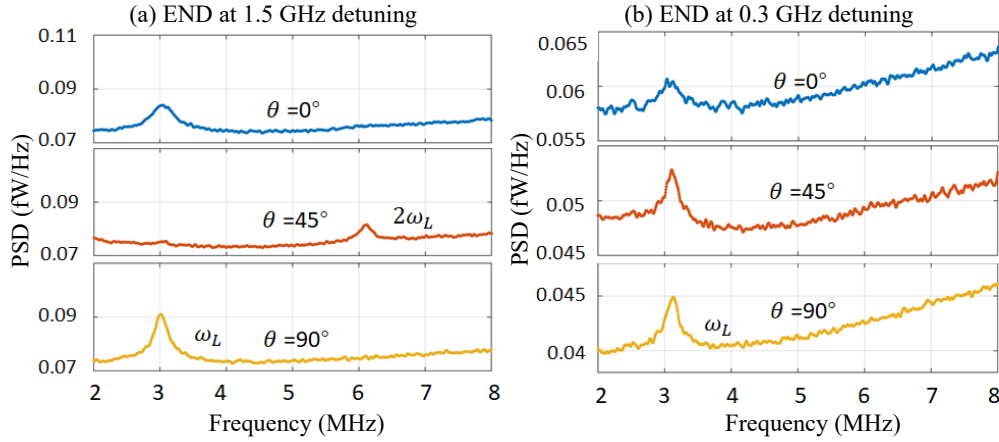


Figure 2.8: Experimental spectra obtained for $\theta = 0^\circ$, 45° and 90° in the case of (a) the END set-up and an optical detuning 1.5 GHz; (b) the END set-up and 0.3 GHz. The laser input power is about 1 mW.

while absorption effects dominate close to resonance. Far from resonance, circular and linear birefringence effects are dominant, leading to polarization independent results for the RND set-up and polarization dependent spectra for the END one respectively. On the contrary, close to resonance, circular dichroism leads to polarization independent END spectra while linear dichroism is associated with θ dependent RND spectra.

2.5 Conclusion

In this chapter, the preliminary SNS results of metastable Helium have been obtained. For the experimental set up, we realized that both rotation and ellipticity noise recorded in RND and END should be performed to have complete results. In terms of the experimental results, new SNS results are found: there are two spin resonances at ω_L and $2\omega_L$ and these resonance have θ dependence. These noises can be interpreted by the circular or linear birefringence and dichroism effects. In the next chapter, we build a numerical simulation model to reproduce the experimental results.

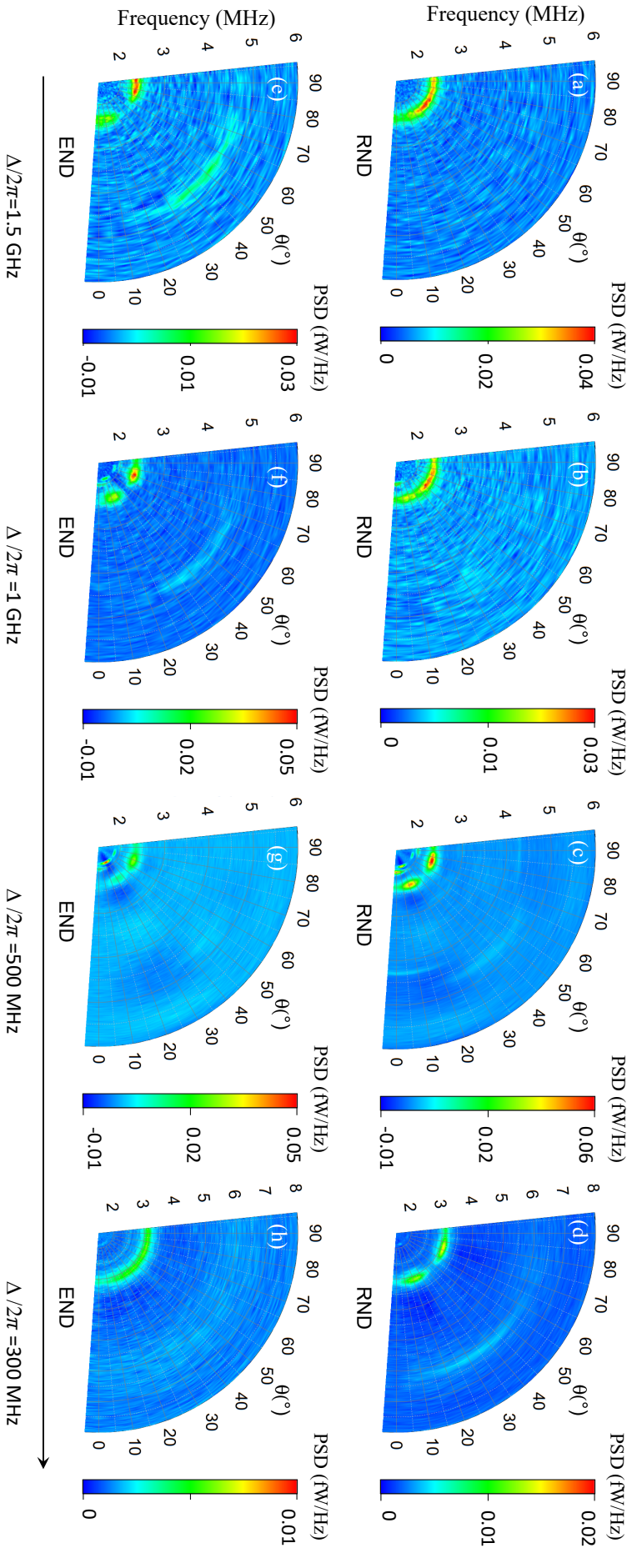


Figure 2.9: Experimental power spectral densities (PSD) obtained with (a-d) the RND set-up and (e-h) the END set-up for decreasing probe detunings: (a,e) $\Delta/2\pi \simeq 1.5$ GHz, (b,f) $\Delta/2\pi \simeq 1$ GHz, (c,g) $\Delta/2\pi \simeq 500$ MHz and (d,h) $\Delta/2\pi \simeq 300$ MHz. ESA resolution and video bandwidths: 42 kHz and 15 Hz, respectively. Larmor frequency: $\omega_L/2\pi \simeq 2.3$ MHz; laser power: 1 mW. (c,d,g,h): data averaged over three spectra. The background noise is removed.

Chapter 3

Spin noise simulation model

Contents

3.1	Density matrix evolution	24
3.2	Noise operator	26
3.3	From atomic spin noise to probe noise	28
3.4	Comparison with experimental results	30
3.5	Conclusion	33

In this chapter, we aim at reproducing the experimental findings from the previous chapter by examining the spin noise of the system. To do so, we introduce a random noise term that mimics the fluctuations of the spin system during its evolution. Specifically, we focus on the optical noise close to D_0 line. We will address the case of other lines in subsequent chapters.

3.1 Density matrix evolution

We consider the density matrix ρ of the system composed of the three Zeeman sublevels of the $|2^3S_1\rangle$ state and the excited $|2^3P_0\rangle$ level. Its evolution can be modeled by the usual equation of evolution:

$$\frac{d\rho}{dt} = \frac{1}{i\hbar}[H, \rho] + \frac{1}{i\hbar}D(\rho). \quad (3.1)$$

Here H is the Hamiltonian and $D(\rho)$ holds for the system relaxations. The Hamiltonian H takes into account the effect of the transverse DC magnetic field through the corresponding Larmor frequency ω_L , and the interaction with the probe light, which couples the σ_{\pm} transitions with Rabi frequencies Ω^{\pm} and is optically detuned from the optical transition by a frequency Δ . We begin from the simplest case of SNS near the D_0 transition line. The corresponding Hamiltonian is :

$$H = \hbar \begin{pmatrix} 0 & \frac{\omega_L}{\sqrt{2}} & 0 & \frac{\Omega^{+*}}{\sqrt{3}} \\ \frac{\omega_L}{\sqrt{2}} & 0 & \frac{\omega_L}{\sqrt{2}} & 0 \\ 0 & \frac{\omega_L}{\sqrt{2}} & 0 & -\frac{\Omega^{-*}}{\sqrt{3}} \\ \frac{\Omega^+}{\sqrt{3}} & 0 & -\frac{\Omega^-}{\sqrt{3}} & \Delta \end{pmatrix}. \quad (3.2)$$

We have $\Omega/2 = \Omega^+ \sigma^+ + \Omega^- \sigma^-$, where the amplitude of Ω is Rabi frequency. The matrix representation of H in Eq. (6.1) is written in the basis $\{|-1\rangle_z, |0\rangle_z, |1\rangle_z, |e\rangle\}$, where $|-1\rangle_z$, $|0\rangle_z$, $|1\rangle_z$ are the Zeeman sublevels of the lower state of the transition with the quantization axis chosen along z , the light propagation axis, and where $|e\rangle$ is the excited level. For a detailed derivation, see Appendix C.

The relaxation term $D(\rho)$ contains the upper level population decay rate $\Gamma_0/2\pi = 1.6$ MHz, the transit rate γ_t of the atoms through the beam and the Raman coherence decay rate γ_R of the lower levels. In our experimental conditions, $\gamma_t/2\pi \simeq \gamma_R/2\pi \simeq 30$ kHz. The optical coherence decay rate is Γ . As already shown in many circumstances, the velocity changing collisions in this system are very efficient to redistribute the atoms among the different velocity classes [76, 81], leading to the fact that Γ can be replaced by the Doppler width in the simulations, i. e. $\Gamma/2\pi = 0.8$ GHz.

Term	Notation	Value
Spontaneous decay rate of level 2^3P	Γ_0	$\Gamma_0/2\pi = 1.6$ MHz
Doppler broadening	Γ_D	$\Gamma_D/2\pi = 0.8$ GHz
Optical coherence decay rate	Γ	$\Gamma/2\pi = 0.8$ GHz
Transit rate	γ_t	$\gamma_t/2\pi = 30$ kHz
Raman decoherence rate	γ_R	$\gamma_R/2\pi = 30$ kHz
Rabi frequency	Ω	$\Omega/2\pi = 40$ MHz

If we ignore all the disturbances, any state of the system will eventually be in thermal equilibrium after a long enough time under decay $D(\rho)$. The population are then equally distributed in the three Zeeman levels and there is no coherence between them. However, because of the interaction between the system and the environment, the system has fluctuations around this equilibrium. Here we introduce a random noise operator \hat{f} which can be adapted to the physical origin of the experienced fluctuation of the system. Then the evolution of the system in the presence of fluctuations obeys the following formalism,

$$\frac{d\rho}{dt} = \frac{1}{i\hbar}[H, \rho] + \frac{1}{i\hbar}D(\rho) + \hat{f}(t). \quad (3.3)$$

The last term $\hat{f}(t)$ in Eq. (3.3) is introduced to model the source of fluctuations. In principle, all relaxation mechanisms are random by nature and should be taken into account in this term. However, here, for the sake of simplicity, we suppose that the fluctuations arising from the motion of the atoms in and out of the laser beam dominate, and we introduce them in $\hat{f}(t)$ in a heuristic manner. Since the lifetime $1/\Gamma_0$ of the upper level is much shorter than the typical transit time $1/\gamma_t$, we neglect the random fluctuations associated with the upper level and write

$$f(t) = \begin{pmatrix} f_{-1} & k_{-10}^* & k_{-11}^* & 0 \\ k_{-10} & f_0 & k_{01}^* & 0 \\ k_{-11} & k_{01} & f_1 & 0 \\ 0 & 0 & 0 & 0 \end{pmatrix}. \quad (3.4)$$

Finally, the density matrix elements obey the following equations of evolution:

$$\frac{d\rho_{-1-1}}{dt} = -\gamma_t\rho_{-1-1} + \frac{\gamma_t}{3} + \frac{\Gamma_0}{3}\rho_{ee} + f_{-1}, \quad (3.5)$$

$$\frac{d\rho_{00}}{dt} = -\gamma_t\rho_{00} + \frac{\gamma_t}{3} + \frac{\Gamma_0}{3}\rho_{ee} + f_0, \quad (3.6)$$

$$\frac{d\rho_{11}}{dt} = -\gamma_t\rho_{11} + \frac{\gamma_t}{3} + \frac{\Gamma_0}{3}\rho_{ee} + f_1, \quad (3.7)$$

$$\frac{d\rho_{-10}}{dt} = -\gamma_t\rho_{-10} + k_{-10}, \quad (3.8)$$

$$\frac{d\rho_{-11}}{dt} = -\gamma_t\rho_{-11} + k_{-11}, \quad (3.9)$$

$$\frac{d\rho_{01}}{dt} = -\gamma_t\rho_{01} + k_{01}, \quad (3.10)$$

$$(3.11)$$

where ρ_{ij} refers to the element $\langle i | \rho | j \rangle$ in representation $\{|-1\rangle_z, |0\rangle_z, |1\rangle_z, |e\rangle\}$.

3.2 Noise operator

In this section, we derive the concrete form of the noise operator used in the simulation code.

The noise matrix modeling the fluctuations due to the atoms randomly entering and leaving the beam reads, when restricted to the three sublevels of the ground state :

$$f^z(t) = \begin{pmatrix} f_{-1} & k_{-1,0}^* & k_{-1,1}^* \\ k_{-1,0} & f_0 & k_{0,1}^* \\ k_{-1,1} & k_{0,1} & f_1 \end{pmatrix}, \quad (3.12)$$

where the superscript z means that this matrix is written in the basis linked to the z quantization axis for the spin. From the definition of the density matrix, the real diagonal elements f_j , with $j = -1, 0, 1$, can be interpreted as the fluctuations in the sublevel populations. They are related to the variance of the populations of these three sublevels. The non-diagonal elements represent the coherences between these sublevels and are more difficult to derive.

To determine the statistical properties of the non-diagonal terms $k_{i,j}$, we argue that their statistical properties should not depend on the orientation of the quantization axis. We thus make a change of basis to derive the noise matrix f^x in the basis related to the x quantization axis. By this method, the non-diagonal elements can go to the diagonal position where the obeyed physical law is already known.

Firstly, the relations between the spin states in different quantization directions are

$$\begin{aligned} |-1\rangle_x &= \frac{1}{2}(|-1\rangle_z - \sqrt{2}|0\rangle_z + |+1\rangle_z), \\ |0\rangle_x &= \frac{1}{\sqrt{2}}(|-1\rangle_z - |+1\rangle_z), \\ |+1\rangle_x &= \frac{1}{2}(|-1\rangle_z + \sqrt{2}|0\rangle_z + |+1\rangle_z), \end{aligned} \quad (3.13)$$

$$\begin{aligned} |-1\rangle_y &= \frac{1}{2}(|-1\rangle_z + i\sqrt{2}|0\rangle_z - |+1\rangle_z), \\ |0\rangle_y &= \frac{1}{\sqrt{2}}(|-1\rangle_z + |+1\rangle_z), \\ |+1\rangle_y &= \frac{1}{2}(|-1\rangle_z - i\sqrt{2}|0\rangle_z - |+1\rangle_z). \end{aligned} \quad (3.14)$$

The unitary matrices describing the transformations between spin states with different quantization directions are

$$S_{zx} = \frac{1}{2} \begin{pmatrix} 1 & -\sqrt{2} & 1 \\ \sqrt{2} & 0 & -\sqrt{2} \\ 1 & \sqrt{2} & 1 \end{pmatrix}, \quad (3.15)$$

$$S_{zy} = \frac{1}{2} \begin{pmatrix} 1 & i\sqrt{2} & -1 \\ \sqrt{2} & 0 & \sqrt{2} \\ 1 & -i\sqrt{2} & -1 \end{pmatrix}. \quad (3.16)$$

Here S_{zx}, S_{zy} are the transformation matrices for the spin states from quantization axis z to x and z to y , respectively. We can thus make a change of basis to derive the noise matrix

f^x in the basis related to the x quantization axis:

$$f^x = S_{zx} \cdot f^z(t) \cdot S_{zx}^{-1}. \quad (3.17)$$

From Eqs. (3.17) and (3.15), one obtains the expressions of the diagonal elements of f^x as a function of those of f^z :

$$f_{-1}^x = f_0 - \frac{\operatorname{Re}(k_{-1,0})}{\sqrt{2}} + \frac{\operatorname{Re}(k_{-1,1})}{2} - \frac{\operatorname{Re}(k_{0,1})}{\sqrt{2}}, \quad (3.18)$$

$$f_0^x = -\frac{f_0}{2} - \operatorname{Re}(k_{-1,1}), \quad (3.19)$$

$$f_1^x = f_0 + \frac{\operatorname{Re}(k_{-1,0})}{\sqrt{2}} + \frac{\operatorname{Re}(k_{-1,1})}{2} + \frac{\operatorname{Re}(k_{0,1})}{\sqrt{2}}. \quad (3.20)$$

Similarly, one can make a change of basis from z to y quantization axis:

$$f^y = S_{zy} \cdot f^z(t) \cdot S_{zy}^{-1}, \quad (3.21)$$

leading to the following relations between the diagonal elements of f^y and the elements of f^z :

$$f_{-1}^y = f_0 - \frac{\operatorname{Im}(k_{-1,0})}{\sqrt{2}} - \frac{\operatorname{Re}(k_{-1,1})}{2} - \frac{\operatorname{Im}(k_{0,1})}{\sqrt{2}}, \quad (3.22)$$

$$f_0^y = -\frac{f_0}{2} + \operatorname{Re}(k_{-1,1}), \quad (3.23)$$

$$f_1^y = f_0 + \frac{\operatorname{Im}(k_{-1,0})}{\sqrt{2}} - \frac{\operatorname{Re}(k_{-1,1})}{2} + \frac{\operatorname{Im}(k_{0,1})}{\sqrt{2}}. \quad (3.24)$$

From Eqs. (3.18 ~ 3.20) and Eqs. (3.22 ~ 3.24), we succeed in converting the off-diagonal elements in the noise operator to the diagonal ones in another quantization direction. We can thus derive the distribution law of the non-diagonal terms from the properties of the diagonal elements in different quantization directions. The distribution of the diagonal elements should all be the same whatever the quantization axis. Suppose that the diagonal elements of the noise operator for all quantization directions z, x, y obey

$$f_i dt \sim N(0, \sigma^2), \quad i = -1, 0, 1. \quad (3.25)$$

Since for two different random variables, one has

$$\operatorname{Var}(aX + bY) = a^2 \operatorname{Var}(X) + b^2 \operatorname{Var}(Y) + 2ab \operatorname{Cov}(X, Y), \quad (3.26)$$

where Var and Cov are the variance and covariance, respectively. we can deduce from Eqs. (3.18 ~ 3.20) that the real and imaginary parts of the non-diagonal elements k_{ij} exhibit variances, which are $3/4$ times those of the diagonal elements. For any couple $i \neq j$, $\operatorname{Re}(k_{ij} dt)$ and $\operatorname{Im}(k_{ij} dt)$ are thus independent centered Gaussian variables of variance $\frac{3}{4}\sigma^2$.

$$\operatorname{Re}(k_{i,j} dt), \operatorname{Im}(k_{i,j} dt) \sim N\left(0, \frac{3}{4}\sigma^2\right), \quad i, j = -1, 0, 1. \quad (3.27)$$

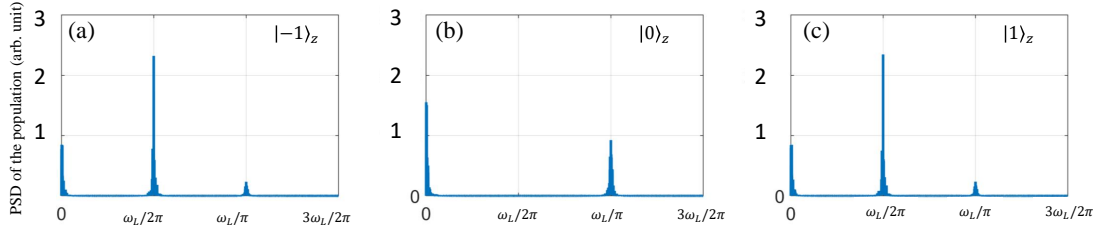


Figure 3.1: The PSD of the populations of the ground levels (a) $|-1\rangle_z$ (b) $|0\rangle_z$ (c) $|+1\rangle_z$. With the introduced random noise $\hat{f}(t)$, the population of each level has a random noise centered around the Larmor frequency and/or the double Larmor frequency. The time duration of the sample is $T = 50/\gamma_t$. The time step duration $t = 1/50\Gamma$.

To implement the simulation, the variance σ^2 is required. The real diagonal terms f_j with $j = -1, 0, 1$ correspond to the fluctuations of the populations of the three ground state sublevels. Since the average number of atoms \bar{N} in the interaction region is large, the Poissonian laws governing the fluctuations $f_j dt$ of the fraction of atoms in state j leaving and entering the interaction volume over a simulation time step dt are approximated by Gaussian random variables with a sum of their variances equal to

$$\sigma^2 = 2\gamma_t dt / 3\bar{N}. \quad (3.28)$$

where γ_t (with $\gamma_t/2\pi = 30\text{kHz}$) is the transit rate of the atoms evaluated from the experiment [76]. The density of the metastable helium atoms is around $n_{at} = 2 \times 10^{17} \text{m}^{-3}$ [82]. Then the average number of atoms \bar{N} in the interaction region is around

$$\bar{N} = n_{at} V = 1.08 \times 10^9, \quad (3.29)$$

where V is the beam volume with a diameter 0.6 mm and a length 6 cm. With Eqs. (3.25) and (3.27), the noise matrix \hat{f} can be obtained.

Figure 3.1 shows the PSD of the population of each ground level obtained from simulation. With the introduced random noise matrix $\hat{f}(t)$, the population is not a constant value anymore. In the presence of a magnetic field, the populations exhibit components at both the Larmor frequency and its second harmonic. One should note that until now, there is no light included. These frequencies are a property of the system itself and not of the detection method. This weak fluctuation $\Delta\rho(t)$ can then be probed as shown in the next section.

3.3 From atomic spin noise to probe noise

The propagation of a transverse wave in the medium obeys:

$$\Delta \mathbf{E} - \frac{1}{c^2} \frac{\partial^2 \mathbf{E}}{\partial t^2} = \mu_0 \frac{\partial^2 \mathbf{P}}{\partial t^2}. \quad (3.30)$$

Here we can simplify the equation a little bit by introducing the slowly varying envelopes of the electric field and polarization:

$$\mathbf{P} = (\mathcal{P}(z, t)e^{i(kz-\omega t)} + c.c)/2 \quad \text{and} \quad \mathbf{E} = (\mathcal{E}(z, t)e^{i(kz-\omega t)} + c.c)/2, \quad (3.31)$$

where \mathcal{P} , \mathcal{E} are the complex amplitudes of the polarization of the medium and the field, respectively. We set in these equations $k = \omega/c$ as for free space propagation (the phase shifts due to the index of refraction will be encapsulated in the slowly varying envelope). Neglecting the second derivatives of the field in z and t , the field propagation equation under slowly varying envelope approximation is :

$$\partial_z \mathcal{E} + \frac{1}{c} \partial_t \mathcal{E} = i \frac{\omega}{2\epsilon_0 c} \mathcal{P}. \quad (3.32)$$

To save some computation time, we suppose that the medium is optically thin, i.e. $|\partial_z \mathcal{E} \ll \frac{1}{c} |\partial_t \mathcal{E}|$, leading to:

$$\mathcal{E}(L, t + \frac{L}{c}) = \mathbf{E}_{in} + \partial_z \mathcal{E} \cdot L + \partial_t \mathcal{E} \cdot \frac{L}{c} = \mathbf{E}_{in} + i \frac{\omega}{2\epsilon_0 c} \mathcal{P}(t) \cdot L \quad (3.33)$$

When the medium has negligible absorption, the complex amplitude \mathcal{E} varies little over the propagation along z . This *thin cell approximation* is reasonable. The polarization of the medium \mathcal{P} can be obtained from the density matrix (See Appendix C):

$$\mathcal{P}^\pm = n_{at} \text{Tr}(\rho \hat{d}^\pm) = \pm n_{at} \frac{d_0}{\sqrt{3}} \langle \pm 1 | \rho | e \rangle, \quad (3.34)$$

where we have $\mathcal{P} = \mathcal{P}^+ \sigma^+ + \mathcal{P}^- \sigma^-$, the atom number density $n_{at} = 2 \times 10^{17}/\text{m}^3$, the dipole moment operator \hat{d} and the irreducible matrix element of the transition $d_0 = 1.5 \times 10^{-29} \text{C}\cdot\text{m}$.

After the cell, the probe will pass through wave plates. In END set-up, the outgoing field has the following relation with the input field

$$\begin{pmatrix} E'_x \\ E'_y \end{pmatrix} = \text{HWP} \cdot \text{QWP} \cdot \begin{pmatrix} E_x \\ E_y \end{pmatrix}, \quad (3.35)$$

where HWP and QWP are the Jones matrices of the corresponding wave plates. The Jones matrix of the HPW is

$$\text{HWP} = \begin{pmatrix} \cos(2\theta_h) & \sin(2\theta_h) \\ \sin(2\theta_h) & -\cos(2\theta_h) \end{pmatrix}, \quad (3.36)$$

where θ_h is the orientation (fast axis direction) of the HWP. The Jones matrix of the QWP is

$$\text{QWP} = \begin{pmatrix} \cos(\theta_q)^2 + i \sin(\theta_q)^2 & (1-i) \cos(\theta_q) \sin(\theta_q) \\ (1-i) \cos(\theta_q) \sin(\theta_q) & i \cos(\theta_q)^2 + \sin(\theta_q)^2 \end{pmatrix}, \quad (3.37)$$

where θ_q is the orientation of the QWP. As we already know, the balance detection system finally records the fluctuation e_\perp perpendicular to the main polarization direction. In the

simulation, we can suppose that the main direction along x after the wave plate. Then $\text{Im } e_{\perp} = E'_y$. The orientation of the wave plates is optimized automatically to make the mean value of e_{\perp} equal to zero. With this condition, we have the parameters θ_h and θ_q . From Eq. (3.35~ 3.37), the imaginary part of the perpendicular fluctuation is

$$\text{Im}(e_{\perp})(t) = \frac{1}{2\sqrt{2}}[(1+i)e^{-2i\theta_h}E^- + (1-i)e^{-2i(\theta_h-\theta_q)}E^- - (1+i)e^{2i\theta_h}E^+ - (1-i)e^{-2i(\theta_q-\theta_h)}E^+]. \quad (3.38)$$

Here E^{\pm} are the σ^{\pm} circular components of the probe after the cell. This small fluctuation can be amplified by the mean field amplitude E : the detector receives $2E \text{Im}(e_{\perp})(t)$ as shown in Eq. 2.5. The power spectra can then easily be analyzed by fast Fourier transformation using MATLAB.

3.4 Comparison with experimental results

The results of these simulations are shown in Figure 3.2 after having removed the background noise. They reproduce very well the experimental results of Figure 3.3: as the probe approaches resonance, the patterns of RND and END are exchanged as the dominant effect goes from birefringence to dichroism. It is even visible that similarly to the experimental data, the noise component at ω_L is stronger close to $\theta = 0^\circ$ than to $\theta = 90^\circ$. Nevertheless, one can notice a small discrepancy by about 5 to 10° between the angular positions of the peaks, and it is visible that the experimental resonances are broader than the theoretical ones. The first discrepancy can be explained by the fact that finding the angle $\theta = 0^\circ$ is not easy and by some possible misorientation of the DC magnetic field. The fact that the experimental noise peaks are broader than the simulated ones can arise from the fact that the Rabi frequency can be underestimated. Indeed, the simulations are based on its average value across the Gaussian beam section (top-hat beam approximation), while in the experiment it is larger at the center of the beam, which can broaden the SNS peaks. Possible magnetic field inhomogeneities can also contribute to this discrepancy.

In summary, here both qualitative and even quantitative agreement are obtained with the experimental results. It should be noted that although the parameters are extracted from other experimental data, the computed noise values agree with the recorded spin noise spectra. Nevertheless, here we admit that when we are close to the resonance region, first of all, there is more disturbance to the system which cannot be strictly seen as in thermal equilibrium. Especially, the existence of the optical pumping effect makes the absorption of the medium exhibit some polarization dependence for the probe light. This can affect the noise peak value at different θ . Secondly, the thin cell approximation introduces some error as it does not take the absorption of the light (and light noise) during the propagation. As a result, the absorption in the simulations is weaker than in the experiment and gives larger spin noise than experiment.

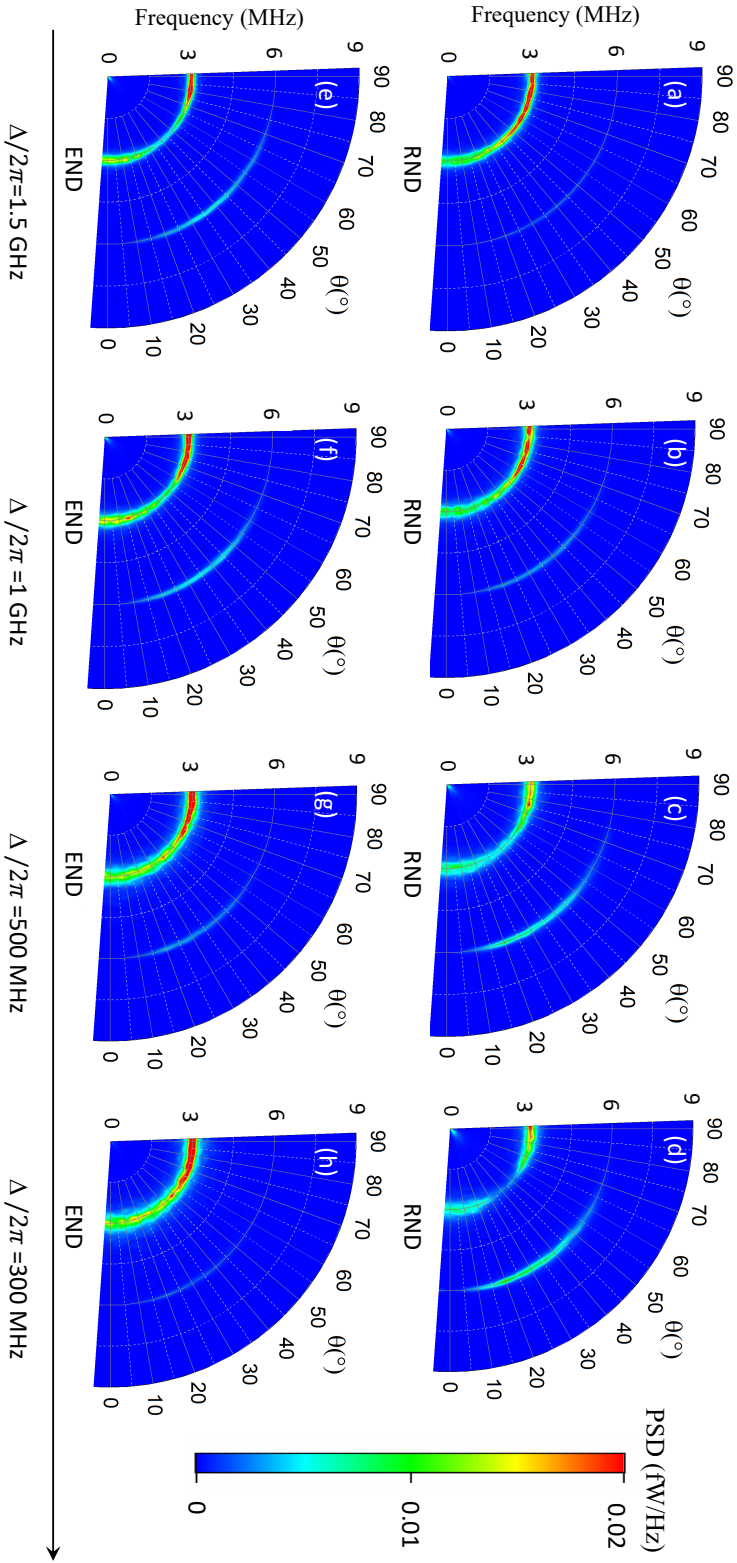


Figure 3.2: Simulated power spectral densities (PSD) obtained with (a-d) the RND set-up and (e-h) the END set-up for decreasing probe detunings: (a,e) $\Delta/2\pi \simeq 1.5$ GHz, (b,f) $\Delta/2\pi \simeq 1$ GHz, (c,g) $\Delta/2\pi \simeq 500$ MHz and (d,h) $\Delta/2\pi \simeq 300$ MHz. Larmor frequency: $\omega_L/2\pi \simeq 3$ MHz; Rabi frequency: $2\pi \times 40$ MHz. The background noise is not included.

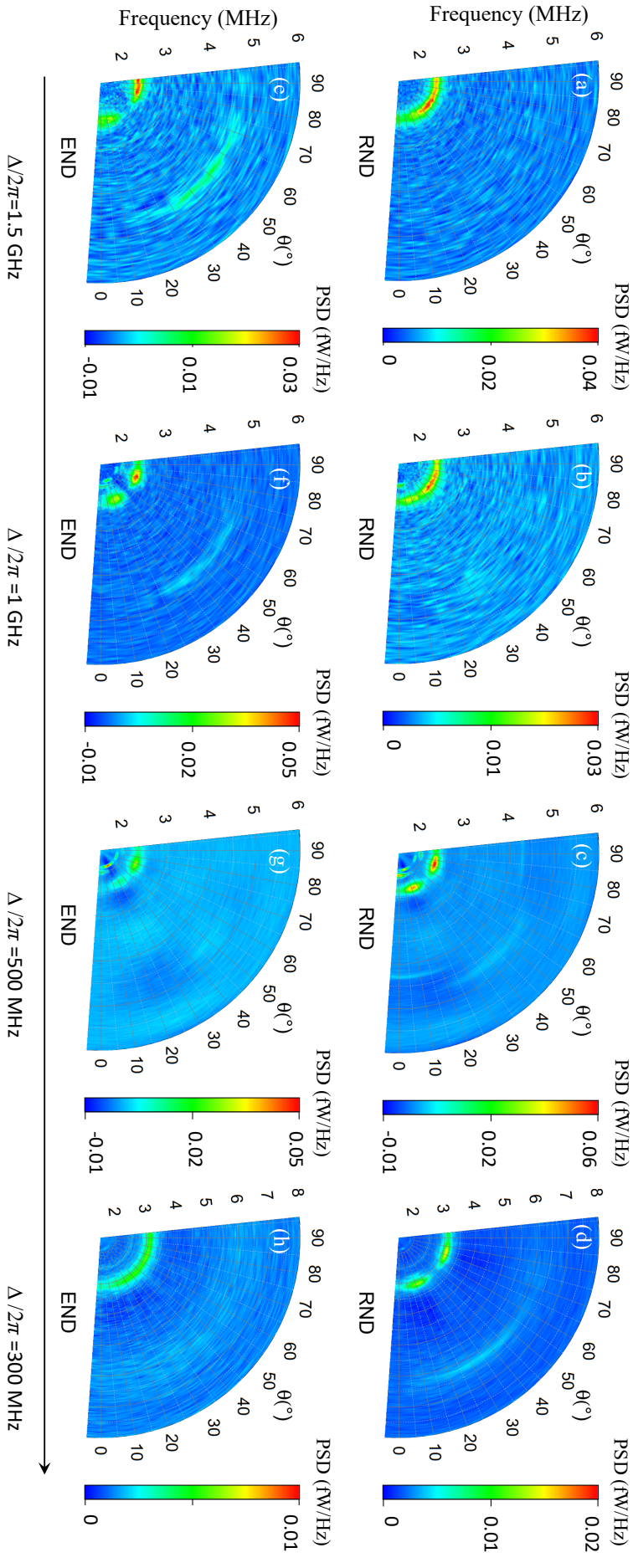


Figure 3.3: Experimental power spectral densities (PSD) obtained with (a-d) the RND set-up and (e-h) the END set-up for decreasing probe detunings: (a,e) $\Delta/2\pi \simeq 1.5$ GHz, (b,f) $\Delta/2\pi \simeq 1$ GHz, (c,g) $\Delta/2\pi \simeq 500$ MHz and (d,h) $\Delta/2\pi \simeq 300$ MHz. ESA resolution and video bandwidths: 42 kHz and 15 Hz, respectively. Larmor frequency: $\omega_L/2\pi \simeq 2.3$ MHz; laser power: 1 mW. (c,d,g,h): data averaged over three spectra. The back ground noise is removed.

3.5 Conclusion

In this chapter, we use the density matrix formalism to describe the evolution of the system. To include the random noise that an open system experiences in the environment, a noise matrix \hat{f} is introduced. By simply considering the main source of noise—atom moves in and out of the laser beam, we can quantify the variance of the ground level population which is related to the diagonal elements of the noise matrix. Furthermore, the non-diagonal elements are also accessible by the noise matrix with other quantization directions. With the obtained noisy system, the probe noise can be well calculated. Accurate reproduction of the measurements proves that this is a very good model. In the following chapter, we will extend the situation to two other more complex situations: SNS near D_1 and D_2 , and try to provide a clear physical picture to interpret these results.

SNS around the D_1 and D_2 transition lines of ^4He

SNS around the D_0 transition has been studied experimentally in Chapter 2 and described theoretically and numerically in Chapter 3. Metastable ^4He has three well separated optical transitions: D_0 ($J = 1 \rightarrow J = 0$), D_1 ($J = 1 \rightarrow J = 1$), and D_2 ($J = 1 \rightarrow J = 2$). The SNS of metastable helium near the two other transition lines, D_1 and D_2 , is investigated in this chapter. Firstly, the model established in Chapter 3 is applied to the D_1 and D_2 lines and compared with the corresponding experimental results to verify the applicability of the model. Secondly, we use ^4He as an ideal toy model for the study of spin systems larger than $1/2$ because one can easily tune the number of sublevels of the upper levels from one to five. We develop a clear map for SNS of spin-1 systems by comparing experimental results for the three different lines. To reach this goal, we first theoretically describe the different spin degrees of freedom that can exist in spin-1 systems, and show that eight modes can be isolated similarly to the eight multipole moments' precessions already studied in earlier works [83]. We indeed explain how the different noise modes map to the two types of available optical detection: Faraday rotation noise or ellipticity noise.

4.1 SNS results close to the D_1 and D_2 lines

D_0 , D_1 , D_2 have the same ground level but different upper level structures as shown in Figure 4.2. D_2 has the strongest absorption, followed by D_1 , and D_0 is the weakest absorption line as shown in Figure 4.1². In this chapter, like in standard SNS experiments [2], we suppose here that i) the sample is probed using *linearly polarized light* and ii) the probe light is *far detuned from resonance*. The wavelengths of the probe are indicated in Fig. 4.1, so that absorption and dichroism can be neglected [11] and only birefringence effects (i.e., refractive effects) are considered.

²Here the optical depth is obtained with 1.5 mW power which is the value used in real SNS experiment. At resonance, this power has a strong saturation effect.

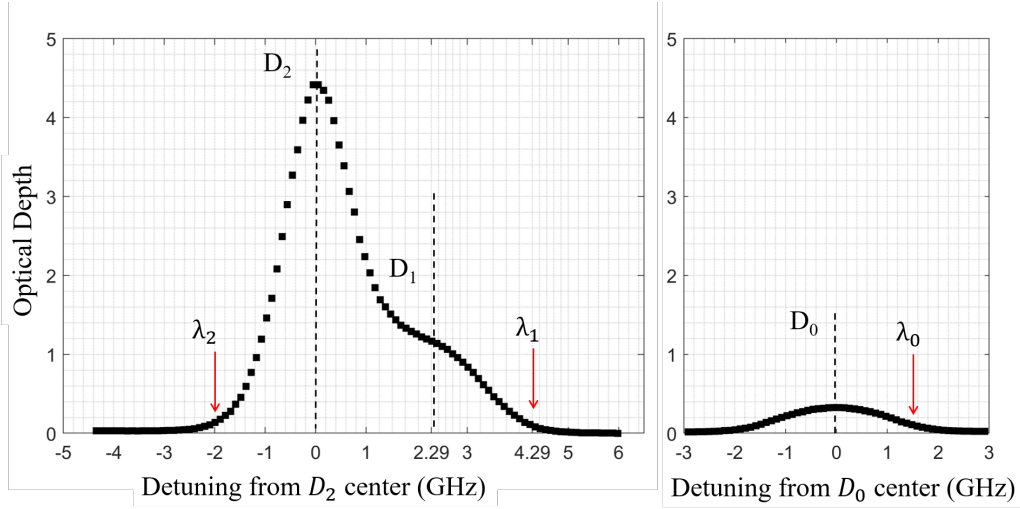


Figure 4.1: Experimental measurement of the optical depth near the three transition lines D_0 , D_1 , D_2 with probe power 1.5 mW and beam diameter 0.6 mm. λ_0 , λ_1 , λ_2 indicate the wavelength of actual SNS experiments near the three lines.

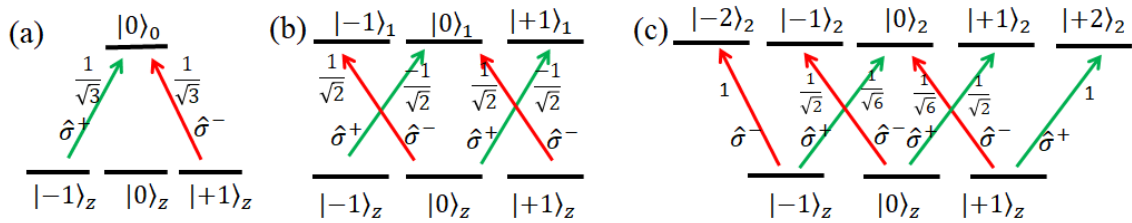


Figure 4.2: The level structure of the D_0 , D_1 , D_2 lines. With the quantization axis along light propagation direction z , only σ coupling channels are excited. The coupling types and the corresponding Clebsch-Gordan coefficients between levels are shown in the figure.

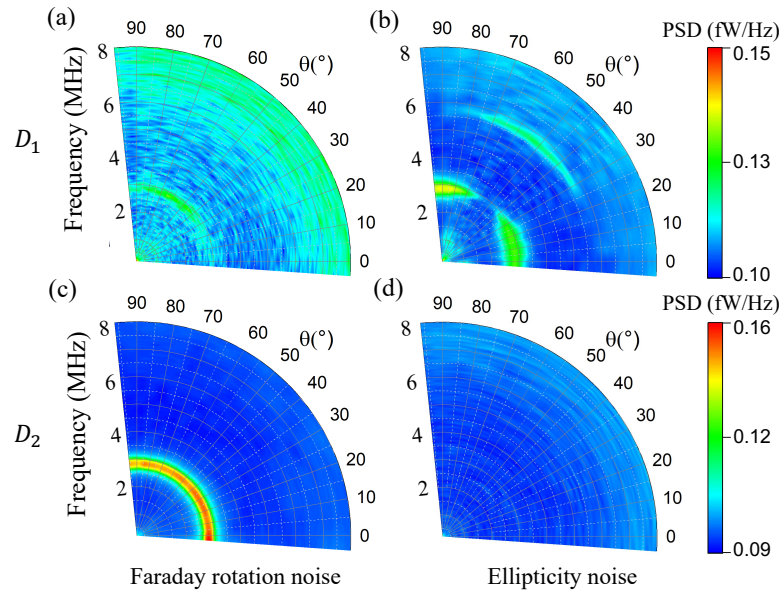


Figure 4.3: Experimental spin noise spectra for FR noise (left column) and ellipticity noise (right column). (a,b) Laser blue detuned by 2 GHz from the D_1 line; (c,d) Laser red detuned by 2 GHz from the D_2 line. Laser power: 1.5 mW

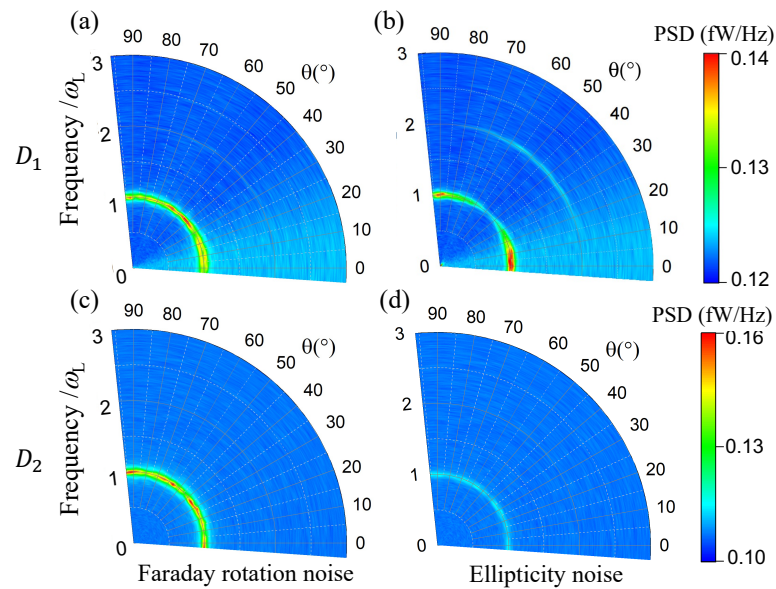


Figure 4.4: Simulated spin noise spectra corresponding to the measurements of Fig. 4.3. The parameters of the simulations are taken from the experiment.

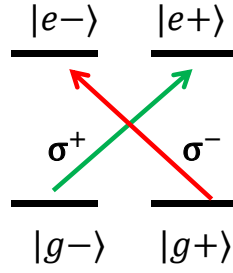


Figure 4.5: The simplified spin- $\frac{1}{2}$ model.

The experimental and simulated results are shown in Figure 4.3 and Figure 4.4, respectively.

The experimental results lead to the following observations:

1. D_1 has very weak FR noise at ω_L frequency and very similar ellipticity noise as D_0 . The ellipticity noise has two resonances at ω_L and $2\omega_L$ frequency with strong but different θ dependence: ω_L is strongest at $\theta = 0^\circ$ and $\theta = 90^\circ$ while $2\omega_L$ is strongest around $\theta = 50^\circ$, which is typical of linear birefringence.
2. D_2 has strong FR noise at ω_L whereas no ellipticity noise can be observed in the experiment. And there is no obvious θ dependence.

The simulation results of Fig. 4.4 lead to the following conclusions:

1. The simulations of D_1 SNS reproduce the experimental results, except the amplitude of the FR noise.
2. The simulations of D_2 reproduce the experimental results. Nevertheless, some weak ellipticity noise can be observed only in the simulations as shown in Fig. 4.4 (d).

We thus conclude that our model, whose validity in the case of the D_0 line was proved in the preceding chapters, also reproduces the SNS behavior close to the D_1 and D_2 lines. However, the interpretation of these results and the discussion of the remaining discrepancies requires a closer examination, which will be performed in the next section.

4.2 Interpretation in terms of spin noise modes

Before one can understand the random spin fluctuations, the spin states of such an atomic system must first be properly described. In the literature, FR effect is always described by a simplified spin-1/2 system [9, 44, 54]. This type of model, shown in Figure 4.5, is frequently used to explain how light interacts with matter in atomic and semiconductor systems [84, 85].

However, this model can lead only to conventional orientation noise for the linearly polarized probe laser¹.

Systems with a spin higher than 1 can exhibit much richer SNS signals such as ellipticity noise, which can give rise to polarization dependent resonances at both the Larmor and twice the Larmor frequencies [11, 42, 86]. High spin systems are ubiquitous and used in many applications in modern quantum technologies [87, 88]: understanding their dynamics and the corresponding spontaneous noise can thus have both fundamental and technological interests. Such investigations are nevertheless complicated by the hyperfine structure of the alkali atoms that are often used in SNS studies performed in atom vapors. In this context, metastable ⁴He appears as an ideal toy model as a spin one system for the study of spin systems larger than 1/2.

4.2.1 Spin-1 noise decomposition

This section discusses the various noise processes in a spin-1 system and their dynamic evolution under the influence of a transverse magnetic field. The way these different noises can be optically detected and the corresponding spectra are discussed in the following sections.

In the context of spin noise studies where one observes the fluctuations of the system around its thermal equilibrium state, the density matrix of a spin one system can be written as the sum of two parts: the thermal equilibrium state and the fluctuations around this thermal equilibrium state [89]:

$$\rho = \frac{1}{3}\hat{\mathbb{I}} + \frac{1}{2} \sum_{i=1}^8 \lambda_i \hat{M}_i. \quad (4.1)$$

In this equation the fluctuations are expanded over the spin operators \hat{M}_i , $i = 1..8$, of a single particle, with coefficients $\lambda_i \equiv \text{Tr}[\rho \hat{M}_i]$. The \hat{M}_i 's are traceless Hermitian operators, and obey the orthogonality relation $\text{Tr}(\hat{M}_i \hat{M}_j) = 2\delta_{ij}$. With the quantization axis along z , i.e. in a basis consisting in the three kets $\{|-1\rangle_z, |0\rangle_z, |1\rangle_z\}$, the first three operators $\hat{M}_1, \hat{M}_2, \hat{M}_3$ describe the polarization of the spin along the directions z , x , and y , respectively:

$$\hat{M}_1 = \begin{bmatrix} 1 & 0 & 0 \\ 0 & 0 & 0 \\ 0 & 0 & -1 \end{bmatrix}, \quad (4.2)$$

$$\hat{M}_2 = \frac{1}{\sqrt{2}} \begin{bmatrix} 0 & 1 & 0 \\ 1 & 0 & 1 \\ 0 & 1 & 0 \end{bmatrix}, \quad (4.3)$$

$$\hat{M}_3 = \frac{1}{\sqrt{2}} \begin{bmatrix} 0 & -i & 0 \\ i & 0 & -i \\ 0 & i & 0 \end{bmatrix}. \quad (4.4)$$

¹More details about spin-1/2 system are given in Appendix B

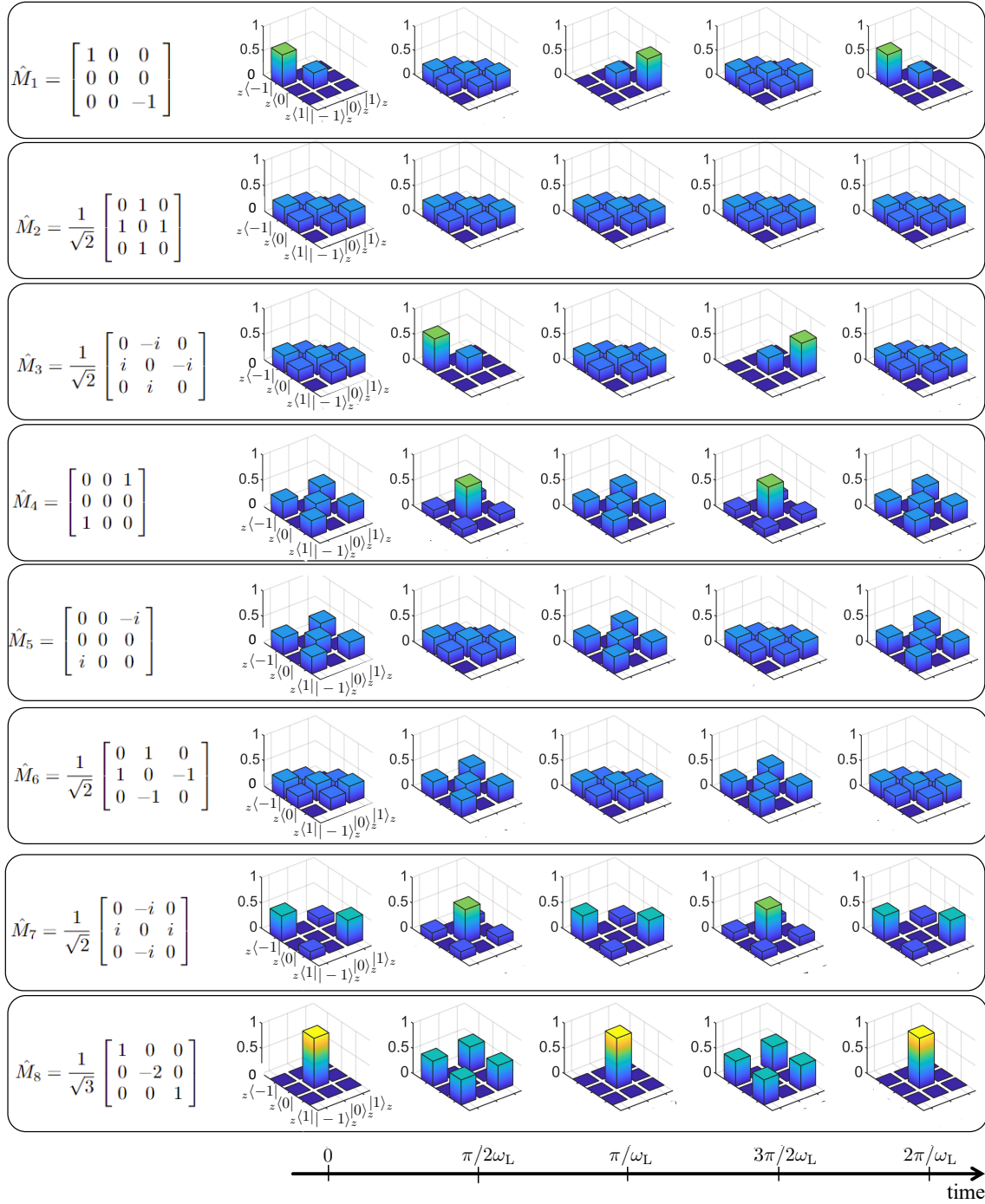


Figure 4.6: Time evolution of the density matrix in the transverse magnetic field with 8 different initial conditions including $\hat{M}_1 \cdots \hat{M}_8$. The bars correspond to the moduli of the density matrix elements. To clearly show the oscillation, \hat{M}_7 is shifted in time by $\pi/4\omega_L$.

The five remaining operators are represented by the following matrices:

$$\hat{M}_4 = \begin{bmatrix} 0 & 0 & 1 \\ 0 & 0 & 0 \\ 1 & 0 & 0 \end{bmatrix}, \quad \hat{M}_5 = \begin{bmatrix} 0 & 0 & -i \\ 0 & 0 & 0 \\ i & 0 & 0 \end{bmatrix}, \quad (4.5)$$

$$\hat{M}_6 = \frac{1}{\sqrt{2}} \begin{bmatrix} 0 & 1 & 0 \\ 1 & 0 & -1 \\ 0 & -1 & 0 \end{bmatrix}, \quad \hat{M}_7 = \frac{1}{\sqrt{2}} \begin{bmatrix} 0 & -i & 0 \\ i & 0 & i \\ 0 & -i & 0 \end{bmatrix}, \quad (4.6)$$

$$\hat{M}_8 = \frac{1}{\sqrt{3}} \begin{bmatrix} 1 & 0 & 0 \\ 0 & -2 & 0 \\ 0 & 0 & 1 \end{bmatrix}. \quad (4.7)$$

The operators \hat{M}_4, \hat{M}_5 describe coherences between the spin states $|-1\rangle_z$ and $|+1\rangle_z$, while \hat{M}_6 and \hat{M}_7 describe coherences between $|0\rangle_z$ and the states $|\pm 1\rangle_z$. Finally, \hat{M}_8 describes the spin alignment corresponding to population imbalance between $|0\rangle_z$ and the other two states.

4.2.2 Time evolution

The fluctuations of the spin system at thermal equilibrium correspond to the appearance of non zero random values for the coefficients λ_i at random instants. In a typical SNS experiment, a weak magnetic field is always introduced to shift the spin noise resonance frequency from DC where technical noises are dominant. Therefore, each time one of the processes \hat{M}_i is excited, it further evolves under the influence of this magnetic field. We consider here a magnetic field B_x oriented along the x direction, orthogonal to the propagation direction of the probe light. The evolution is then governed by the Hamiltonian $H_B = \hbar\omega_L \hat{M}_2$, where ω_L is the Larmor frequency associated to the 3S_1 state. The density operator $\rho(t)$ thus evolves from $t = 0$ to t according to

$$\rho(t) = \hat{U}(t)\rho(0)\hat{U}^\dagger(t) = \frac{1}{3}\hat{\mathbb{I}} + \frac{1}{2}\sum_i \lambda_i \hat{U}(t)\hat{M}_i\hat{U}^\dagger(t), \quad (4.8)$$

where the evolution operator $\hat{U}(t)$ is given by

$$\hat{U}(t) = \exp\left[-i\frac{H_B t}{\hbar}\right], \quad H_B = \frac{\hbar\omega_L}{\sqrt{2}} \begin{bmatrix} 0 & 1 & 0 \\ 1 & 0 & 1 \\ 0 & 1 & 0 \end{bmatrix}. \quad (4.9)$$

To understand the observations of SNS signals in different experimental conditions, it is instructive to observe the evolution of every component $\hat{U}(t)\hat{M}_i\hat{U}^\dagger(t)$ for $i = 1..8$. We thus successively take $\lambda_i \neq 0$ for $i = 1..8$ at $t = 0$ and compute the subsequent evolution of ρ . The results are reproduced in Figure 4.6. For example, the first frame in Fig. 4.6 corresponds to $i = 1$. To make the evolution easier to visualize, we take the

exaggerated value $\lambda_1 = 2/3$, which is much larger than the noise amplitudes observed in the experiment. The initial state at $t = 0$ is then

$$\rho(0) = \frac{1}{3}\hat{\mathbb{I}} + \frac{1}{3}\hat{M}_1 = \begin{bmatrix} \frac{2}{3} & 0 & 0 \\ 0 & \frac{1}{3} & 0 \\ 0 & 0 & 0 \end{bmatrix}. \quad (4.10)$$

The first frame in Fig. 4.6 then represents the evolution of this density operator with time at different instants between $t = 0$ and $t = 2\pi/\omega_L$. Since the non-diagonal elements of the density matrix are complex, we choose here to plot only the moduli of the density matrix elements.

Fig. 4.6 shows that the different initial states, labeled $i = 1..8$, lead to very different types of evolution. For some of them, populations ($i = 1, 3$) oscillate at the Larmor frequency ω_L while some others ($i = 4, 5, 6, 7, 8$) oscillate at $2\omega_L$. The case $i = 2$ corresponds to the spin aligned along x , which is an eigenstate of \hat{H} and thus does not evolve with time. Moreover, if one focuses for example on the population difference between $|-1\rangle_z$ and $|1\rangle_z$, which is at the origin of the spin noise signal in a standard SNS configuration (see the following sections), one notices that only mechanisms corresponding to $i = 1, 3$ lead to an oscillation of this population difference. This means that, in a standard SNS configuration, only one noise peak at ω_L will be observed.

Such a discussion, which is particularly simple in the case of the standard far detuned SNS configuration in which one observes the Faraday rotation noise with a transverse magnetic field, will be extended to more exotic configurations in the next sections, then involving all the different processes of Fig. 4.6.

4.3 Probe noise

4.3.1 Probe noise modes near D_0 transition line

We start in the present section by considering the simplest case of the $J = 0$ upper level (D_0 line). The first type of fluctuating birefringence that can be created by spin noise is circular birefringence (CB), leading to Faraday rotation for the probe light. It can be well explained using the simplified spin-1/2 model shown in Fig. 4.5. It corresponds to a relative phase difference between the two circularly polarized components of the probe light, which interact with two different transitions. Thus each circularly polarized component probes the population of one of the two ground state sublevels $|g_-\rangle$ and $|g_+\rangle$ [9]. This simplified picture remains valid in the case of our $J = 1 \rightarrow J = 0$ transition [10, 11, 90], as can be seen in Figure 4.7(a) as a linearly polarized light propagating along z can only probe the populations of sublevels $|-1\rangle_z$ and $|+1\rangle_z$. A fluctuating population imbalance between these two sublevels, such as \hat{M}_1, \hat{M}_3 polarized states shown in Fig. 4.6, leads to a fluctuating Faraday rotation (FR), whose observation is independent of the relative angle between the incident linear polarization direction and the magnetic field. However, we know that there are other kinds of fluctuations other than population unbalance between

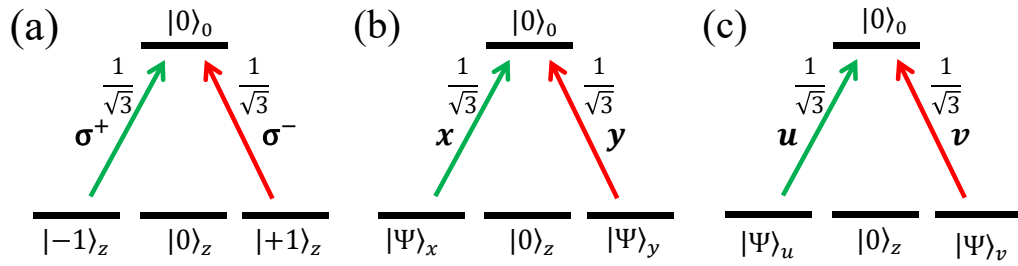


Figure 4.7: Level structure of the D_0 line. (a) Circular representation with quantization axis along z . (b) x/y linear representation, the ground levels are coupled to the excited state by x or y polarization components. (c) In u/v linear representation, the ground levels are coupled to the excited state by u or v polarization components.

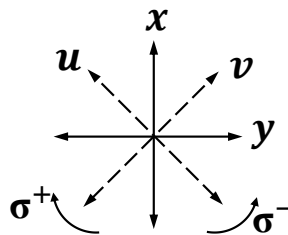


Figure 4.8: The three different bases in which the fluctuating birefringence of the vapor can be expanded.

$| -1 \rangle_z$ and $| +1 \rangle_z$. The remaining mechanisms $\hat{M}_i, i = 4, 5, 6, 7, 8$ effects on the ground levels $| -1 \rangle_z, | 0 \rangle_z, | +1 \rangle_z$ are vague. As the system changes, the populations of the $| -1 \rangle_z$ and $| +1 \rangle_z$ states fluctuate together. This implies that the interaction strengths between the system and the left or right circular components are equal. In terms of probe noise, apart from Faraday rotation fluctuations, there is ellipticity noise from linear birefringence (LB). Here we introduce two kinds of LB effect with different neutral axis LB with neutral axes oriented along x and y , and LB with neutral axes oriented along the directions u and v of Figure 4.8(b), which are rotated by $\pi/4$ with respect to x and y . The relations between the unit vectors along those different directions shown in Fig. 4.8 are given by

$$\boldsymbol{\sigma}^+ = (\mathbf{x} + i\mathbf{y})/\sqrt{2}, \quad (4.11)$$

$$\boldsymbol{\sigma}^- = (\mathbf{x} - i\mathbf{y})/\sqrt{2}, \quad (4.12)$$

and

$$\mathbf{u} = (\mathbf{x} - \mathbf{y})/\sqrt{2}, \quad (4.13)$$

$$\mathbf{v} = (\mathbf{x} + \mathbf{y})/\sqrt{2}. \quad (4.14)$$

By virtue of the relations between the different bases vectors, the superpositions states of the ground state sublevels that are coupled to the upper level by linearly polarized light can be constructed. The sublevels, which are coupled to the excited state by x - and y -polarized light are, respectively:

$$|\Psi_x\rangle = \frac{1}{\sqrt{2}}(|-1\rangle_z + |+1\rangle_z), \quad (4.15)$$

$$|\Psi_y\rangle = -\frac{i}{\sqrt{2}}(|-1\rangle_z - |+1\rangle_z). \quad (4.16)$$

In the case of the u/v LB, the sublevels that are coupled by light polarized along the u and v directions (see Fig. 4.7(b)) are respectively given by

$$|\Psi_u\rangle = \frac{1}{\sqrt{2}}(e^{i\pi/4}|-1\rangle_z + e^{-i\pi/4}|+1\rangle_z), \quad (4.17)$$

$$|\Psi_v\rangle = \frac{1}{\sqrt{2}}(e^{-i\pi/4}|-1\rangle_z + e^{i\pi/4}|+1\rangle_z). \quad (4.18)$$

The coupling relations in the different bases of D_0 are shown in Fig.4.7. The three considered bases are:

1. Circular basis: $| -1 \rangle_z, | 0 \rangle_z, | +1 \rangle_z$
2. Linear x/y basis: $|\Psi_x\rangle, | 0 \rangle_z, |\Psi_y\rangle$
3. Linear u/v basis: $|\Psi_u\rangle, | 0 \rangle_z, |\Psi_v\rangle$

Different bases are linked by unitary transformation matrices:

$$\begin{pmatrix} |\Psi_x\rangle \\ |0\rangle_z \\ |\Psi_y\rangle \end{pmatrix} = M_{g,0}^{(x/y)} \begin{pmatrix} |-1\rangle_z \\ |0\rangle_z \\ |+1\rangle_z \end{pmatrix}, \quad \begin{pmatrix} |\Psi_u\rangle \\ |0\rangle_z \\ |\Psi_v\rangle \end{pmatrix} = M_{g,0}^{(u/v)} \begin{pmatrix} |-1\rangle_z \\ |0\rangle_z \\ |+1\rangle_z \end{pmatrix}, \quad (4.19)$$

where

$$M_{g,0}^{(x/y)} = \frac{1}{\sqrt{2}} \begin{bmatrix} 1 & 0 & 1 \\ 0 & \sqrt{2} & 0 \\ -i & 0 & i \end{bmatrix}, \quad (4.20)$$

$$M_{g,0}^{(u/v)} = \frac{1}{2} \begin{bmatrix} 1+i & 0 & 1-i \\ 0 & 2 & 0 \\ 1-i & 0 & 1+i \end{bmatrix}. \quad (4.21)$$

We can then gain insight into knowing whether there can be linear birefringence noises along the x/y and u/v neutral axes, by observing the oscillation mechanisms of Fig. 4.6 in these alternative bases¹. This is performed in Figure 4.9. For each of these five mechanisms, the oscillation is shown in the only basis that leads to a significant population difference.

The mechanisms $\hat{M}_4, \hat{M}_5, \hat{M}_6, \hat{M}_7, \hat{M}_8$ that do not contribute to the population difference between $|-1\rangle_z$ and $|+1\rangle_z$ contribute to the population difference between either $\{|\Psi_x\rangle, |\Psi_y\rangle\}$ ($\hat{M}_4, \hat{M}_7, \hat{M}_8$) or $\{|\Psi_u\rangle, |\Psi_v\rangle\}$ (\hat{M}_5, \hat{M}_6).

4.3.2 Oscillation frequencies of the modes

One can see the oscillation frequencies of the system in the different bases as shown in Fig.4.6 and Fig.4.9. In the present section, we derive analytical expressions for the evolutions of the population differences. This part gives the analytical equation of the population difference. Considering the Schrödinger equation corresponding to a spin-1 subjected to a transverse \mathbf{B} field:

$$\frac{i}{\hbar} \frac{d}{dt} |\psi\rangle = H_B |\psi\rangle, \quad \text{where } H_B = \frac{\hbar\omega_L}{\sqrt{2}} \begin{bmatrix} 0 & 1 & 0 \\ 1 & 0 & 1 \\ 0 & 1 & 0 \end{bmatrix}, \quad (4.22)$$

in the basis $\{|-1\rangle_z, |0\rangle_z, |1\rangle_z\}$, where ω_L is the Larmor frequency. H_B/\hbar has three eigenvalues, $-\omega_L, 0$, and ω_L , associated to the following eigenvectors:

$$\begin{aligned} |v_1\rangle &= \frac{1}{2} [|-1\rangle_z + \sqrt{2}|0\rangle_z + |1\rangle_z], \\ |v_2\rangle &= \frac{1}{\sqrt{2}} [|-1\rangle_z - |1\rangle_z], \\ |v_3\rangle &= \frac{1}{2} [|-1\rangle_z - \sqrt{2}|0\rangle_z + |1\rangle_z]. \end{aligned} \quad (4.23)$$

¹The transformation of operators in different bases can be found in Appendix. D

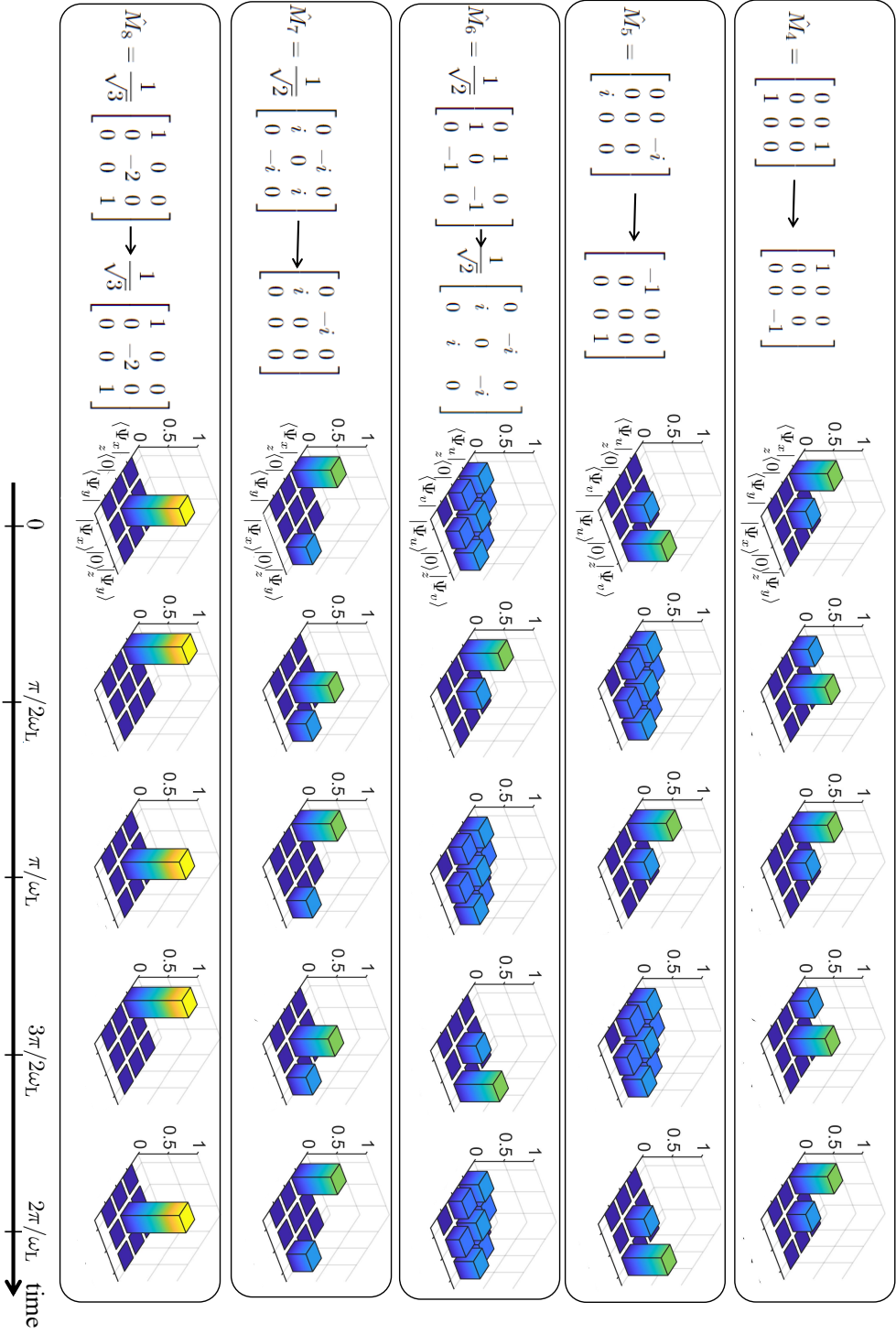


Figure 4.9: Same as Fig. 4.6 for the mechanisms \hat{M}_4 , \hat{M}_5 , \hat{M}_6 , \hat{M}_7 , and \hat{M}_8 , represented in another basis. The evolution of the density matrix for mechanisms \hat{M}_4 , \hat{M}_5 , \hat{M}_7 , and \hat{M}_8 (respectively \hat{M}_5 and \hat{M}_6) is shown in the x/y (respectively u/v) representation. The matrices after the arrow are the mechanisms represented in the new basis. For each mechanism, the oscillation is shown in the only basis that leads to a significant population difference.

Any solution of the Schrödinger equation can be written as a linear combination of the three eigenvectors v_i , with coefficients C_i that depend on the initial state:

$$|\psi\rangle = C_1 e^{-i\omega_L t} |v_1\rangle + C_2 |v_2\rangle + C_3 e^{i\omega_L t} |v_3\rangle \quad (4.24)$$

$$= \begin{bmatrix} \frac{1}{2}C_1 e^{-i\omega_L t} + \frac{1}{\sqrt{2}}C_2 + \frac{1}{2}C_3 e^{i\omega_L t} \\ \frac{1}{\sqrt{2}}C_1 e^{-i\omega_L t} - \frac{1}{\sqrt{2}}C_3 e^{i\omega_L t} \\ \frac{1}{2}C_1 e^{-i\omega_L t} - \frac{1}{\sqrt{2}}C_2 + \frac{1}{2}C_3 e^{i\omega_L t} \end{bmatrix} \quad (4.25)$$

so that the population difference between the levels $|-1\rangle_z$ and $|+1\rangle_z$ is

$$n_{-1} - n_1 = |{}_z\langle -1|\psi\rangle|^2 - |{}_z\langle +1|\psi\rangle|^2 \quad (4.26)$$

$$= \sqrt{2}|C_1 C_2| \cos[\omega_L t + \varphi_{21}] + \sqrt{2}|C_2 C_3| \cos[\omega_L t + \varphi_{32}], \quad (4.27)$$

where φ_{21} [resp φ_{32}] is the phase difference between C_1 and C_2 [resp. C_2 and C_3]: the oscillation between the states $|-1\rangle_z$ and $|+1\rangle_z$ contains only the frequency ω_L .

Now we write the ket $|\psi\rangle$ in the basis $|\Psi_x\rangle, |0\rangle_z, |\Psi_y\rangle$ instead of the original one. The ground level is transformed through¹ $M_{g,0}^{(x/y)\dagger}$. The state in the new basis is

$$|\psi'\rangle = M_{g,0}^{(x/y)\dagger} |\psi\rangle = \begin{bmatrix} (C_1 e^{-i\omega_L t} + C_3 e^{i\omega_L t})/\sqrt{2} \\ (C_1 e^{-i\omega_L t} - C_3 e^{i\omega_L t})/\sqrt{2} \\ iC_2 \end{bmatrix}. \quad (4.28)$$

The population difference between $|\Psi_x\rangle$ and $|\Psi_y\rangle$ reads:

$$\begin{aligned} n_x - n_y &= |\langle \Psi_x|\psi\rangle|^2 - |\langle \Psi_y|\psi\rangle|^2 \\ &= \frac{1}{2}C_1^2 + \frac{1}{2}C_3^2 - C_2^2 + \frac{1}{2}C_1 C_3 e^{-i2\omega_L t} + \frac{1}{2}C_3 C_1 e^{i2\omega_L t} \\ &= \frac{1}{2}C_1^2 + \frac{1}{2}C_3^2 - C_2^2 + |C_1 C_3| \cos(2\omega_L t + \varphi_{31}), \end{aligned} \quad (4.29)$$

where φ_{31} is the phase difference between C_1 and C_3 . The population difference has frequency components at $2\omega_L$ and zero frequencies.

Finally, the wave function in the u/v representation can be deduced from $M_{g,0}^{(u/v)\dagger}$

$$|\psi''\rangle = M_{g,0}^{(u/v)*} |\psi\rangle = \begin{bmatrix} \frac{1}{2}C_1 e^{-i\omega_L t} - \frac{i}{\sqrt{2}}C_2 + \frac{1}{2}C_3 e^{i\omega_L t} \\ (C_1 e^{-i\omega_L t} - C_3 e^{i\omega_L t})/\sqrt{2} \\ \frac{1}{2}C_1 e^{-i\omega_L t} + \frac{i}{\sqrt{2}}C_2 + \frac{1}{2}C_3 e^{i\omega_L t} \end{bmatrix}. \quad (4.30)$$

The corresponding population difference is

$$\begin{aligned} n_u - n_v &= |\langle \Psi_u|\psi\rangle|^2 - |\langle \Psi_v|\psi\rangle|^2 \\ &= \frac{i}{\sqrt{2}}(C_1 C_2 e^{-i\omega_L t} - C_2 C_1 e^{i\omega_L t} + C_3 C_2 e^{i\omega_L t} - C_2 C_3 e^{-i\omega_L t}) \\ &= \sqrt{2}|C_1 C_2| \sin(\omega_L t + \varphi_{21}) + \sqrt{2}|C_2 C_3| \sin(\omega_L t + \varphi_{32}). \end{aligned} \quad (4.31)$$

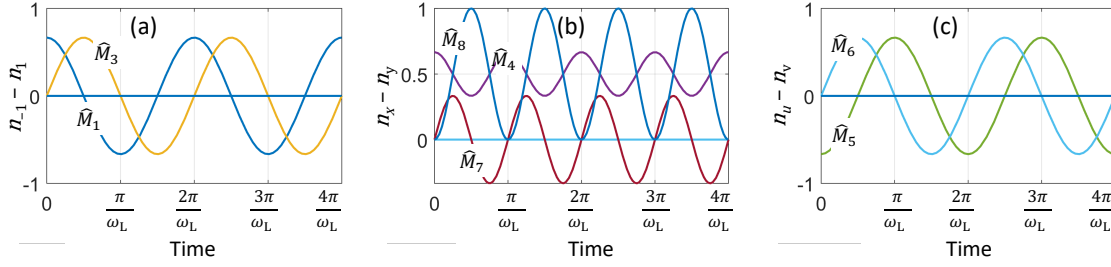


Figure 4.10: Time evolution of the population difference between states (a) $|{-1}\rangle_z$ and $|{1}\rangle_z$, (b) $|\Psi_x\rangle$ and $|\Psi_y\rangle$, and (c) $|\Psi_u\rangle$ and $|\Psi_v\rangle$ for different mechanisms.

The population difference has only components oscillating at ω_L . These population differences in different bases are shown in Figure 4.10. Initially, the system is prepared in eight different polarization states. Fig. 4.10 shows that each mechanism (except \hat{M}_2) contributes to one and only one population difference in the three different bases with the oscillation frequency ω_L or $2\omega_L$.

Table 4.1: Different noise mechanisms corresponding to different detection strategies and different types of fluctuating birefringences for the D_0 transition.

Noise type	Faraday rotation	Ellipticity	
Birefringence type	Circular birefringence	x/y Linear birefringence	u/v Linear birefringence
Mechanisms	\hat{M}_1, \hat{M}_3	$\hat{M}_4, \hat{M}_7, \hat{M}_8$	\hat{M}_5, \hat{M}_6
Frequency	ω_L	$2\omega_L$	ω_L

These oscillation modes of population differences correspond to different types of birefringence types for a large detuned probe (and of dichroism types for a near resonance probe). The relation between the spin mechanisms and the corresponding features for the probe are summarized in Table 4.1. So far, the spin noise of spin systems with the simplest structures such as D_0 has been well studied. The properties of the SNS in this relatively pure and simple closed $J = 1 \rightarrow J = 0$ atomic transition demonstrate the peculiarities of spin noise of a spin 1 system like the $|2^3S_1\rangle$ state.

We then generalize this approach to more complicated situations, namely the D_1 $J = 1 \rightarrow J = 1$ and D_2 $J = 1 \rightarrow J = 2$ transitions, in which the upper level has respectively three and five Zeeman sublevels. This allows us to predict the conditions in which the different noise modes can be detected, in particular the dependence of the different SNS signals on the probe polarization orientation in the different detection schemes. These predictions are compared with extensive measurements, allowing one to understand the influence of the structure of the upper level of the transition and going well beyond the oversimplified spin-1/2 model.

¹ $M_{g,0}^{(x/y)\dagger}$ is the conjugate matrix of $M_{g,0}^{(x/y)}$

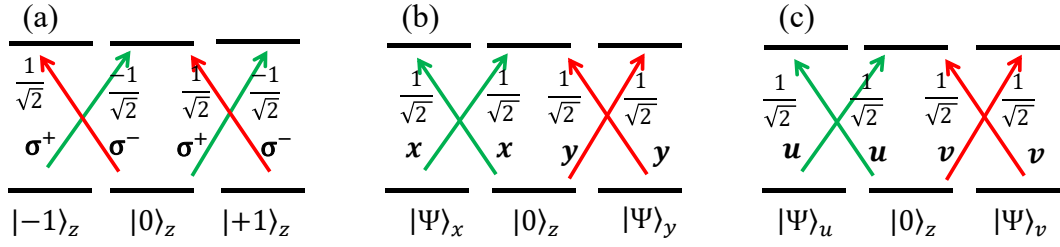


Figure 4.11: Sublevel structure of the levels of the D_1 transition. (a) In circular representation. (b) In linear x/y representation. (c) In linear u/v representation. Notice that the three sublevels of the upper level of the transition are different in the three representations.

4.4 Cases of the D_1 and D_2 transitions

4.4.1 FR noise of the D_1 and D_2 transitions

In this section, the discussion of the observation of the different spin noise modes is extended to the two other lines of metastable helium, namely the $J = 1 \rightarrow J = 1$ and $J = 1 \rightarrow J = 2$ transitions (so-called D_1 and D_2 lines). Figures 4.11(a) and 4.12(a) show the corresponding sublevel structures with the quantization axis oriented along z , together with the Clebsch-Gordan coefficients of the associated transitions. By comparison with the $J = 1 \rightarrow J = 0$ transition investigated in the preceding section (see Fig. 4.7(a)), one can see that the D_1 and D_2 lines are much more complicated. Understanding how the spin noise modes of Fig. 4.6 can be observed either as FR noise or as ellipticity noise thus requires a bit more formalism than in the case of the D_0 line. We start in this section by comparing the Faraday rotation noise for the D_1 and D_2 lines with the one for the D_0 line discussed in the previous section. To this aim, the optical couplings between the sublevels of the lower and upper levels of the different transitions, schematized in Figs. 4.7(a), 4.11(a), and 4.12(a) are represented as matrices. For example, for the D_0 line, the Clebsch-Gordan coefficients representing the coupling by σ^+ -polarized light between the two levels read

$$\Gamma_0^{(+)} = \begin{bmatrix} \frac{1}{\sqrt{3}} \\ 0 \\ 0 \end{bmatrix}, \quad (4.32)$$

where the three rows correspond to the three sublevels $| -1 \rangle_z$, $| 0 \rangle_z$, and $| +1 \rangle_z$ of the ground state and the single column to the nondegenerate upper level. Similarly, the coupling matrix for σ^- -polarized light reads

$$\Gamma_0^{(-)} = \begin{bmatrix} 0 \\ 0 \\ \frac{1}{\sqrt{3}} \end{bmatrix}. \quad (4.33)$$

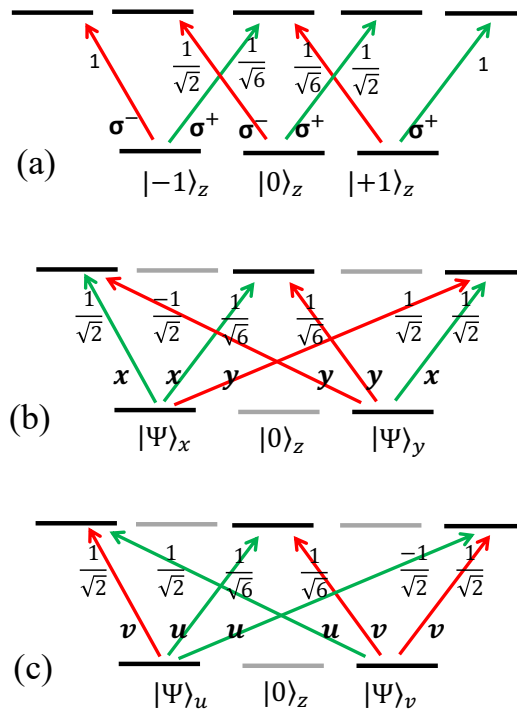


Figure 4.12: Same as Fig. 4.11 for the D_2 line. The transitions between the gray sublevels are not shown because they are coupled with equal Clebsch-Gordan coefficients for the two polarizations (x and y in (b) or u and v in (c)) and thus do not contribute to any linear birefringence.

Further, the coupling matrices for the D_1 line read

$$\Gamma_1^{(+)} = -\frac{1}{\sqrt{2}} \begin{bmatrix} 0 & 1 & 0 \\ 0 & 0 & 1 \\ 0 & 0 & 0 \end{bmatrix}, \Gamma_1^{(-)} = \frac{1}{\sqrt{2}} \begin{bmatrix} 0 & 0 & 0 \\ 1 & 0 & 0 \\ 0 & 1 & 0 \end{bmatrix}, \quad (4.34)$$

where the columns refer to the excited state of the D_1 line with the quantization axis oriented along z . Finally, in the case of the D_2 line, we have:

$$\Gamma_2^{(+)} = \begin{bmatrix} 0 & 0 & \frac{1}{\sqrt{6}} & 0 & 0 \\ 0 & 0 & 0 & \frac{1}{\sqrt{2}} & 0 \\ 0 & 0 & 0 & 0 & 1 \end{bmatrix}, \quad (4.35)$$

$$\Gamma_2^{(-)} = \begin{bmatrix} 1 & 0 & 0 & 0 & 0 \\ 0 & \frac{1}{\sqrt{2}} & 0 & 0 & 0 \\ 0 & 0 & \frac{1}{\sqrt{6}} & 0 & 0 \end{bmatrix}, \quad (4.36)$$

where the columns correspond to the Zeeman sublevels of the excited state of D_2 .

By comparing Figs. 4.11(a) and 4.12(a) with Fig. 4.7(a), one can predict the behavior of FR spin noise when the laser is tuned close to the D_1 and D_2 transitions. The difference between the D_1 and D_2 lines, on the one hand, and the D_0 line, on the other hand, is that the state $|0\rangle_z$ is now coupled to the upper level by σ^+ and σ^- -polarized light, with the same Clebsch-Gordan coefficients. This means that a fluctuation of the population of this state will induce the same variations of the refractive indices seen by the σ^+ and σ^- polarizations, and will thus not induce any FR. Consequently, some FR noise can be induced only by an imbalance between the populations of the states $|-1\rangle_z$ and $|1\rangle_z$. Figure 4.11(a) shows that for the D_1 line, the situation is the same as for the D_0 line: state $|-1\rangle_z$ affects only σ^+ -polarized light while state $|1\rangle_z$ affects only σ^- -polarized light. FR rotation noise should thus be the same for D_1 and D_0 lines. The situation is slightly different for the D_2 line: Figure 4.12(a) shows that both states $|-1\rangle_z$ and $|1\rangle_z$ are coupled to the upper level by both σ^+ and σ^- -polarized light. But the 1:6 ratio between the transitions strengths shows that again state $|-1\rangle_z$ is coupled to the upper level mainly by σ^+ -polarized light while state $|1\rangle_z$ is sensitive mainly to σ^- -polarized light. We thus expect again FR noise for the D_2 line to be very similar to the one for the D_0 and D_1 lines. These predictions are perfectly confirmed by both the numerical simulations Fig.4.4 and the experimental results Fig.4.3 as shown in the beginning of this chapter.

One can notice that the experimental CB spin noise spectra are weaker for the D_1 line than for the two other lines. The first reason for this is that the D_1 line is weaker than the D_2 line (see Fig. 4.1). But another reason behind this can be deduced from the simulations of Fig. 4.13. This figure shows the evolution of the Faraday rotation versus time, in the presence of the transverse magnetic field, when mechanisms \hat{M}_1 (Fig. 4.13(a)) and \hat{M}_3 (Fig. 4.13(b)) are excited at $t = 0$. These two mechanisms, which are responsible for the FR noise at frequency ω_L , are simulated for the three lines and show that the amplitude of Faraday rotation is approximately the same for the D_1 and D_2 lines for the same initial conditions. However, the signal induced by the D_2 line is out of phase with respect to the

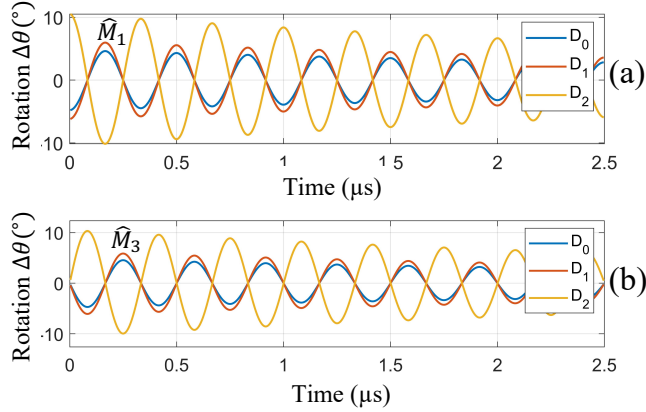


Figure 4.13: Time evolution of the probe polarization rotation close to the D_0 , D_1 , and D_2 lines for initial conditions corresponding to (a) mechanism \hat{M}_1 and (b) mechanism \hat{M}_3 .

ones induced by D_0 and D_1 lines. This phase shift also contributes to reducing the FR noise observed close to the D_1 line, because it contains some signal with the opposite sign coming from the nearby intense D_2 line. This destructive interference effect among the spin noise signals coming from the two transitions further contributes to reducing the FR noise.

4.4.2 Ellipticity noise of the D_1 and D_2 transitions

The prediction of the behavior of the ellipticity noise for the D_1 and D_2 lines can be performed in a manner similar to Section 4.3, i.e., by changing the basis of the lower level from $\{|-1\rangle_z, |0\rangle_z, |1\rangle_z\}$ to some more relevant basis $\{|\Psi_x\rangle, |0\rangle_z, |\Psi_y\rangle\}$ or $\{|\Psi_u\rangle, |0\rangle_z, |\Psi_v\rangle\}$. However, since the upper levels of these two transitions also exhibit several sublevels, this change of basis for the lower level depends on the considered transition. Moreover, one must also perform a change of basis for the upper level in order to isolate the different transitions corresponding to the different states of light polarization of Fig. 4.7(b).

Consequently, the coupling matrices corresponding to the ellipticity noise in the x/y and u/v basis read

$$\Gamma_i^{(x/y)} = M_{g,i}^{(x/y)} \Gamma_i M_{e,i}^{(x/y)}, \quad (4.37)$$

where $i = 0, 1, 2$ denotes the three different transitions with their corresponding upper levels, and where $M_{g,i}^{(x/y)}$ and $M_{e,i}^{(x/y)}$ are the matrices for the change of basis for the ground and excited levels of the transition, respectively. A relation similar to Eq. (4.37) holds for the u/v basis.

The expressions of the matrices for the change of basis are given by

$$M_{g,0}^{(x/y)} = \frac{1}{\sqrt{2}} \begin{bmatrix} 1 & 0 & 1 \\ 0 & \sqrt{2} & 0 \\ -i & 0 & i \end{bmatrix}, \quad (4.38)$$

$$M_{g,0}^{(u/v)} = \frac{1}{2} \begin{bmatrix} 1+i & 0 & 1-i \\ 0 & 2 & 0 \\ 1-i & 0 & 1+i \end{bmatrix}, \quad (4.39)$$

$$M_{e,0}^{(x/y)} = M_{e,0}^{(u/v)} = [1], \quad (4.40)$$

for the D_0 line,

$$M_{g,1}^{(x/y)} = \frac{1}{\sqrt{2}} \begin{bmatrix} -1 & 0 & 1 \\ 0 & \sqrt{2} & 0 \\ i & 0 & i \end{bmatrix}, \quad (4.41)$$

$$M_{g,1}^{(u/v)} = \frac{1}{2} \begin{bmatrix} -1-i & 0 & 1-i \\ 0 & 2 & 0 \\ -1+i & 0 & 1+i \end{bmatrix}, \quad (4.42)$$

$$M_{e,1}^{(x/y)} = \frac{1}{\sqrt{2}} \begin{bmatrix} 1 & 0 & i \\ 0 & \sqrt{2} & 0 \\ -1 & 0 & i \end{bmatrix}, \quad (4.43)$$

$$M_{e,1}^{(u/v)} = \frac{1}{2} \begin{bmatrix} 1-i & 0 & 1+i \\ 0 & 2 & 0 \\ -1-i & 0 & -1+i \end{bmatrix}, \quad (4.44)$$

for the D_1 line, and

$$M_{g,2}^{(x/y)} = M_{g,0}^{(x/y)}, \quad (4.45)$$

$$M_{g,2}^{(u/v)} = M_{g,0}^{(u/v)}, \quad (4.46)$$

$$M_{e,2}^{(x/y)} = \frac{1}{\sqrt{2}} \begin{bmatrix} 1 & 0 & 0 & 0 & i \\ 0 & 1 & 0 & i & 0 \\ 0 & 0 & \sqrt{2} & 0 & 0 \\ 0 & 1 & 0 & -i & 0 \\ 1 & 0 & 0 & 0 & -i \end{bmatrix}, \quad (4.47)$$

$$M_{e,2}^{(u/v)} = \frac{1}{2} \begin{bmatrix} \sqrt{2} & 0 & 0 & 0 & i\sqrt{2} \\ 0 & 1-i & 0 & 1+i & 0 \\ 0 & 0 & 2 & 0 & 0 \\ 0 & 1+i & 0 & 1-i & 0 \\ \sqrt{2} & 0 & 0 & 0 & -i\sqrt{2} \end{bmatrix}, \quad (4.48)$$

for the D_2 line.

Using these transformation matrices in Eq. (4.37), the coupling matrices in these linear

basis become

$$\Gamma_0^{(x)} = \Gamma_0^{(u)} = \begin{bmatrix} \frac{1}{\sqrt{3}} \\ 0 \\ 0 \end{bmatrix}, \quad (4.49)$$

$$\Gamma_0^{(y)} = \Gamma_0^{(v)} = \begin{bmatrix} 0 \\ 0 \\ \frac{1}{\sqrt{3}} \end{bmatrix}, \quad (4.50)$$

for the D_0 line. They confirm the branching ratios represented in Figs. 4.7(b) and 4.7(c) and the results discussed in Section 4.3.

For the D_1 line, the coupling matrices become

$$\Gamma_1^{(x)} = \Gamma_1^{(u)} = \frac{1}{\sqrt{2}} \begin{bmatrix} 0 & 1 & 0 \\ 1 & 0 & 0 \\ 0 & 0 & 0 \end{bmatrix}, \quad (4.51)$$

$$\Gamma_1^{(y)} = \Gamma_1^{(v)} = \frac{1}{\sqrt{2}} \begin{bmatrix} 0 & 0 & 0 \\ 0 & 0 & 1 \\ 0 & 1 & 0 \end{bmatrix}, \quad (4.52)$$

which are summarized in Figs. 4.11(b) and 4.11(c). Finally, for the D_2 line, these matrices read

$$\Gamma_2^{(x)} = \begin{bmatrix} \frac{1}{\sqrt{2}} & 0 & \frac{1}{\sqrt{6}} & 0 & 0 \\ 0 & \frac{1}{\sqrt{2}} & 0 & 0 & 0 \\ 0 & 0 & 0 & 0 & \frac{1}{\sqrt{2}} \end{bmatrix}, \quad (4.53)$$

$$\Gamma_2^{(y)} = \begin{bmatrix} 0 & 0 & 0 & 0 & \frac{1}{\sqrt{2}} \\ 0 & 0 & 0 & \frac{1}{\sqrt{2}} & 0 \\ -\frac{1}{\sqrt{2}} & 0 & \frac{1}{\sqrt{6}} & 0 & 0 \end{bmatrix}, \quad (4.54)$$

and

$$\Gamma_2^{(u)} = \begin{bmatrix} 0 & 0 & \frac{1}{\sqrt{6}} & 0 & -\frac{1}{\sqrt{2}} \\ 0 & \frac{1}{\sqrt{2}} & 0 & 0 & 0 \\ \frac{1}{\sqrt{2}} & 0 & 0 & 0 & 0 \end{bmatrix}, \quad (4.55)$$

$$\Gamma_2^{(v)} = \begin{bmatrix} \frac{1}{\sqrt{2}} & 0 & 0 & 0 & 0 \\ 0 & 0 & 0 & \frac{1}{\sqrt{2}} & 0 \\ 0 & 0 & \frac{1}{\sqrt{6}} & 0 & \frac{1}{\sqrt{2}} \end{bmatrix}. \quad (4.56)$$

These branching ratios are shown in Figs. 4.12(b) and 4.12(c), except for the gray levels of Figs. 4.12(b) and 4.12(c), which are coupled with equal Clebsch-Gordan coefficients for the two polarizations and thus do not contribute to any linear birefringence.

By comparing Figs. 4.7(b), 4.11(b), and 4.12(b), we can predict that the ellipticity noise detected in the vicinity of the D_2 line should be strongly different from the one detected

close to the D_0 and D_1 lines. Indeed, Figs. 4.7(b) and 4.11(b) show that for the D_0 and D_1 lines, the states $|\Psi_x\rangle$ and $|\Psi_y\rangle$ are respectively coupled to the upper level by x - and y - polarized light *only*. On the contrary, in the case of the D_2 line, the states $|\Psi_x\rangle$ and $|\Psi_y\rangle$ are always coupled to the upper level by *both* x - and y - polarized light. For example, according to the coupling coefficients of Fig. 4.12(b) and Eqs. (4.53) and (4.54), the state $|\Psi_x\rangle$ is coupled to the upper level by x - and y - polarized light with probabilities respectively proportional to $2/3$ and $1/2$, which are quite close. This means that the fluctuating LB created by mechanisms \hat{M}_4 , \hat{M}_7 , and \hat{M}_8 of Fig. 4.6 and originating from an imbalance $n_x - n_y$ between the populations of states $|\Psi_x\rangle$ and $|\Psi_y\rangle$ will lead to a much weaker LB in the case of the D_2 line than in the case of the D_0 and D_1 line. Moreover, we predict that the associated ellipticity noise at frequency $2\omega_L$ will be smaller and also less polarization sensitive in the vicinity of the D_2 line.

This conclusion also holds for the component of LB noise with its neutral axes oriented along the u and v directions of Fig. 4.7(b). Comparison of Figs. 4.7(c), 4.11(c), and 4.12(c) again shows that in this case the ellipticity noise at frequency ω_L , corresponding to mechanisms \hat{M}_5 and \hat{M}_6 of Fig. 4.6, should behave similarly in the vicinity of the D_0 and D_1 lines but be much weaker and less polarization resolved for the D_2 line.

These expectations are confirmed by the measurements reproduced in Fig. 4.3 and the simulations of Fig. 4.4. The LB fluctuations of the D_1 line (Figs. 4.3(b) and 4.4(b)) are similar to the ones of the D_0 line. On the contrary, in the vicinity of the D_2 line, the predicted signal (see Fig. 4.4(d)) is so weak that it becomes undetectable in the experiment (see Fig. 4.3(d)).

Finally, Figure 4.14 shows the oscillation of the rotation or ellipticity of an extremely weak probe (0.1 mW) when the atomic system evolves under a magnetic field for each unbalanced initial state.

Figure 4.14 compares the effects of different atomic spin mechanisms summarized in Table 4.1 on the different polarization states of the probe light. The investigations of the seven polarization states are performed with different θ and either rotation or ellipticity according to the corresponding birefringence types. For example, spin polarizations with $\hat{M}_4, \hat{M}_7, \hat{M}_8$ cause x/y LB, therefore they are studied in terms of ellipticity with $\theta = 45^\circ$ and spin polarizations with \hat{M}_5, \hat{M}_6 cause u/v LB, therefore they are studied in terms of ellipticity with $\theta = 0^\circ$.

Figure 4.14 also compares the effects of the same spin mechanism on the polarization states of light with different resonance frequencies near D_0, D_1, D_2 . The three lines show similar oscillation modes but different phases and different amplitudes. For the amplitude, D_2 has the strongest rotation and the weakest ellipticity. In terms of phase, rotation close to D_2 is out of phase with the rotation of the other two lines as shown in Fig. 4.14 (a). Ellipticity for D_1 is out of phase with the ellipticity of the other two lines as shown in Figs. 4.14 (b) and (c).

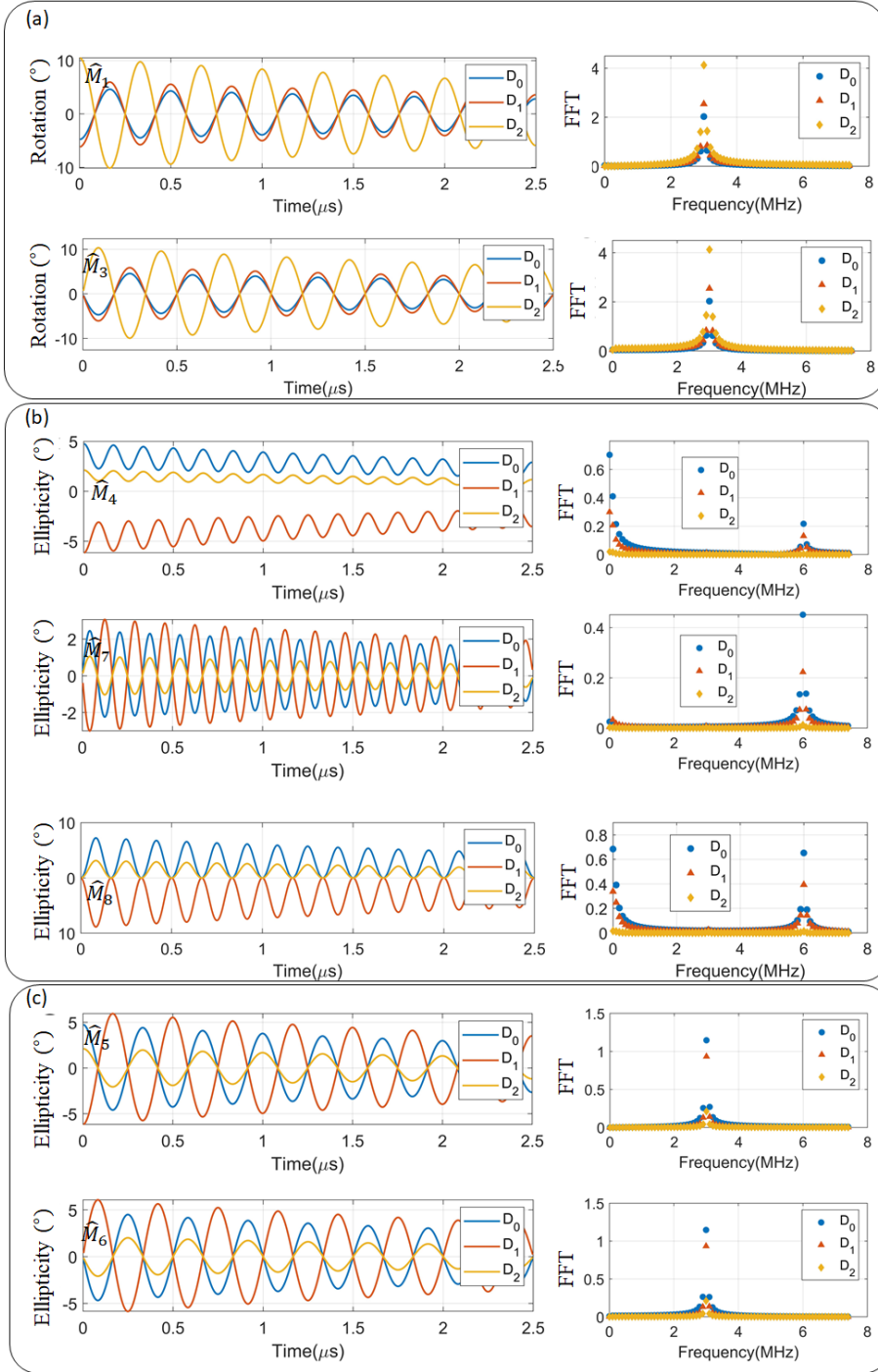


Figure 4.14: Comparison between rotation or ellipticity of probe near D_0 , D_1 , and D_2 under different initial conditions. (a) The polarization rotation (due to CB) with \hat{M}_1 or \hat{M}_3 initially polarized states. (b) The polarization ellipticity (due to x/y LB) with \hat{M}_4 , \hat{M}_7 or \hat{M}_8 initially polarized states. (c) The polarization ellipticity (due to u/v LB) with \hat{M}_5 or \hat{M}_6 initially polarized states.

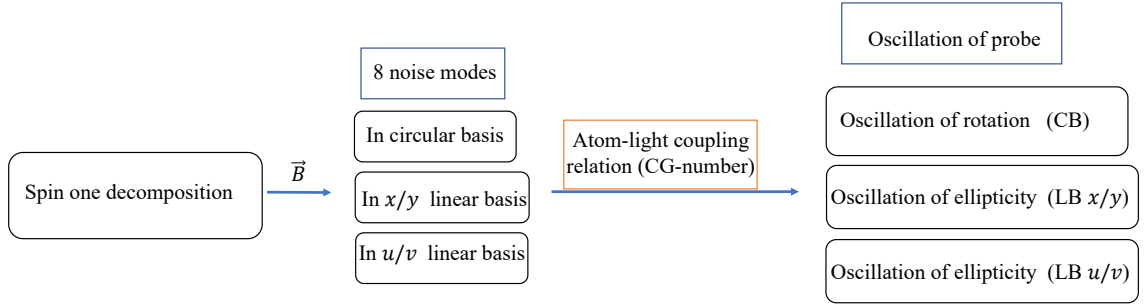


Figure 4.15: The structure of SNS study of a spin-one system.

4.5 Conclusion

In this chapter, the noise modes of a spin-1 system in the presence of a magnetic field are investigated. The corresponding noises imprinted on the polarization of an initially linearly polarized probe light beam are studied in details when the light is detuned from three different transitions corresponding to three different upper level structures. In all cases, both Faraday rotation and ellipticity noises, induced respectively by fluctuating circular and linear birefringences, are theoretically and experimentally analyzed. Figure 4.15 summarizes the processes of SNS of a spin-one system.

Compared with conventional SNS that focuses on Faraday rotation noise only, the additionally detected ellipticity noise opens new windows for the system. Indeed, it permits one to fully unveil the richer spin-noise dynamics of high-spin systems. All put together, the detection of different spin-noise signals for different orientations of the probe polarization permits one to fully attribute the different components of the light polarization noise to different modes of oscillation of the spin state. As a consequence, although the polarization of the probe does not affect the spin noise itself, it has a strong influence on the spin-noise signal when the probe laser effect on the atoms can be neglected.

Moreover, this paper illustrates the fact that contrary to a commonly accepted idea, spin-noise signals obtained with large detuned light do not depend only on the structure of the lower level of the transition: the structure of the upper level matters and can make the linear birefringence so weak that its effect is not visible anymore. Indeed, using metastable ^4He that exhibits three well-separated lines starting from the same $J = 1$ lower level, both theory and experiments confirm that ellipticity and Faraday rotation noises behave differently and that the ellipticity noise resonances can be washed out in the vicinity of some transitions. This is explained by the way of the different spin-noise modes map to the polarization components of the probe light through the associated Clebsch-Gordan coefficients.

The present work has benefited of the relatively simple level structure of ^4He , in which the different transitions are well separated despite Doppler broadening at room temperature. However, it opens interesting perspectives for even more complicated systems, such

as alkali atoms, in which the spins of the levels are even larger, and in which the separation between hyperfine levels is very often smaller than the Doppler broadening. Indeed, generalizing the present approach to these more complicated atoms could allow one to predict the conditions in which one can observe spin noise modes that are usually inaccessible.

Besides, the decomposition of spin noise of the spin-1 system into eight different noise modes could be used to fully characterize the state of a spin-1 system by a tomographic technique based on this set of measurement modes[91, 92].

Correlation between FR noise and ellipticity noise

Contents

5.1	Definitions	60
5.1.1	Covariance	60
5.1.2	Correlator C_2	61
5.1.3	Magnitude square coherence	61
5.2	Correlation results	62
5.2.1	Case where $\theta = 0^\circ$	62
5.2.2	Case where $\theta = 45^\circ$	64
5.3	Interpretation of correlations in terms of spin noise modes	66
5.3.1	Weak correlation at $\theta = 0^\circ$	66
5.3.2	Strong correlation at $\theta = 45^\circ$	67
5.4	Proposed experiment	69
5.5	Conclusion	69

We have seen in the preceding chapters that the spin noise with a spin higher than 1/2 manifests itself as rotation and ellipticity noise of the probe beam. These two kinds of spin noise signatures have been studied in detail in the previous chapters. It is interesting to investigate the correlation of these two types of noise, after we have studied the effect of spin noise on the polarization direction and ellipticity of the probe light, respectively. Because this would give us additional information not included in previous studies.

I begin with some definitions useful for correlation studies and then provide some simulation results, which are encouraging and can shed some insight for future experimental work.

5.1 Definitions

In this section, we introduce several mathematical tools useful to characterize the degree of correlation between two signals.

5.1.1 Covariance

We can detect the rotation angle $\theta_1(t)$ and the ellipticity $\theta_2(t)$ at the same time and get the covariance

$$\text{Cov}(\theta_1(t), \theta_2(t)) = \langle \theta_1(t)\theta_2(t) \rangle, \quad (5.1)$$

which appears in the following equation:

$$\langle [\theta_1(t) + \theta_2(t)]^2 \rangle = \langle \theta_1^2(t) \rangle + \langle \theta_2^2(t) \rangle + 2 \langle \theta_1(t)\theta_2(t) \rangle. \quad (5.2)$$

If ellipticity and rotation are correlated, ie $\langle \theta_1(t)\theta_2(t) \rangle \neq 0$, the variance of the sum of the two signals

$$\theta_3(t) = \theta_1(t) + \theta_2(t) \quad (5.3)$$

is larger or smaller than the sum of the noise powers of $\theta_1(t)$ and $\theta_2(t)$. Further, as before, we can use the PSD to study the correlation in the frequency domain, which is the Fourier transform of the correlation:

$$r_{i,j}(\tau) = \langle \theta_i(t)\theta_j(t + \tau) \rangle \xrightarrow{\mathcal{F}} S_{i,j}(f), \quad i, j = 1, 2, 3 \quad (5.4)$$

when $i = j$, $S_{i,i}$ is the so called *power spectrum*, and when $i \neq j$, $S_{i,j}$ is the *cross correlation spectrum*.

In addition, the normalized covariance, also known as Pearson's product-moment coefficient or correlation coefficient, can be used to characterize the correlation between two signals. The correlation coefficient is defined as

$$\bar{\rho}_{1,2} = \frac{\text{Cov}(\theta_1, \theta_2)}{\sigma_1\sigma_2}, \quad (5.5)$$

where σ_1 and σ_2 are the standard deviations of θ_1 and θ_2 , respectively.

5.1.2 Correlator C_2

We can define the correlator between the two power spectra [46] to evidence the correlation as

$$C_2 \equiv \frac{P_{3,3} - P_{1,1} - P_{2,2}}{P_{1,1} + P_{2,2}}, \quad (5.6)$$

where $P_{i,i}$ is the total integrated PSD over the considered frequency range:

$$P_{i,i} = \int |S_{i,i}(f)|^2 df. \quad (5.7)$$

The correlator C_2 should therefore be expected to be $C_2 = 0$ if the θ_1, θ_2 are uncorrelated, but depart from 0 to -1 or 1 when they are completely anti-correlated or correlated.

5.1.3 Magnitude square coherence

Generally, the cross spectrum is used to study the correlation between two signals. Unlike PSD, which is positive and real, the cross spectrum is a complex function and can be written as

$$S_{1,2}(f) = \text{Re}\{S_{1,2}(f)\} + i \text{Im}\{S_{1,2}(f)\}. \quad (5.8)$$

A complex exponential of frequency f with any phase lag ϕ can be written as a sum of in-phase and quadrature parts:

$$e^{i(ft+\phi)} = e^{ift} \cos \phi + ie^{ift} \sin \phi. \quad (5.9)$$

So the complex value $S_{1,2}(f)$ can describe any linear lagged relationship between $\theta_1(t)$ and $\theta_2(t)$ at a given frequency f . The modulus $|S_{1,2}(f)|$ gives the degree of correlation and the argument $\arg S_{1,2}(f)$ gives the phase shift between the correlated parts of the two signals at frequency f .

In the signal processing literature [93–95], the magnitude square coherence (MSC) is mostly used to describe the frequency distribution of the correlation of the two signals and is defined as

$$C_{1,2}(f) = \frac{|S_{1,2}(f)|^2}{S_{1,1}(f)S_{2,2}(f)}, \quad (5.10)$$

which is the normalized cross spectrum.

It is also convenient to integrate the MSC over frequency to get the total degree of correlation of the two signals $M_{1,2}$:

$$M_{1,2} = \frac{(\int |S_{1,2}(f)| df)^2}{\int S_{1,1}(f) df \int S_{2,2}(f) df}. \quad (5.11)$$

The integrated MSC is usually used when the frequency distribution of the correlation is less interesting.

The covariance, correlator C_2 , MSC $C_{i,j}$ and integrated MSC $M_{i,j}$ used to represent the correlation are all obtained from two original time signals $\theta_1(t)$ and $\theta_2(t)$.

The correlator C_2 is the real part of the cross spectrum after normalization as demonstrated by the following. The auto-correlation of $\theta_3(t)$ is

$$\begin{aligned} r_{3,3}(\tau) &= \langle [\theta_1(t) + \theta_2(t)] \cdot [\theta_1(t + \tau) + \theta_2(t + \tau)] \rangle \\ &= r_{1,1}(\tau) + r_{2,2}(\tau) + r_{1,2}(\tau) + r_{2,1}(\tau), \end{aligned} \quad (5.12)$$

with

$$r_{1,2}(\tau) = r_{2,1}^*(-\tau). \quad (5.13)$$

The PSD of $\theta_3(t)$ is

$$S_{3,3}(f) = S_{1,1}(f) + S_{2,2}(f) + 2 \operatorname{Re}\{S_{1,2}(f)\}. \quad (5.14)$$

From Eqs.(5.4, 5.6, 5.12 - 5.14), we can see that the correlator C_2 is the real part of the cross spectrum after normalization.

The advantage of the correlator C_2 is that it can be obtained from integrated PSD. As shown in [46], in the experiment, we can obtain the PSD by ESA easily and get C_2 . However, the cross spectra rely on the time sequence data, which needs a longer acquisition time to obtain clear spectra.

5.2 Correlation results

We have seen that rotation noise and ellipticity noise come from different types of population imbalance between the sublevels of the system probed with a laser detuned far from resonance. In this situation, there should be no correlation between rotation noise and ellipticity noise since the kinds of spin noise modes contributing to rotation or ellipticity noise are independent of each other.

Nevertheless, for smaller probe detuning both birefringence and dichroism can be created by a certain type of spin noise modes. This is expected to lead to some correlation between ellipticity and rotation noise. To prove this point, the correlation as a function of the detuning is investigated below.

5.2.1 Case where $\theta = 0^\circ$

Firstly, we start with $\theta = 0^\circ$, i.e. the polarization of the incident probe is aligned with the magnetic field. As there is only one resonance at Larmor frequency at $\theta = 0^\circ$, it is supposed to be simpler than other angles θ .

The simulation of Figure 5.1 shows the PSD of $\theta_i(t)$, $i = 1, 2, 3$. The mathematical sum $S_{1,1} + S_{2,2}$ is compared with $S_{3,3}$. The non-zero difference $S_{3,3} - (S_{1,1} + S_{2,2})$ evidences the correlation. The obvious differences between Fig.5.1 (a) and (c) prove that

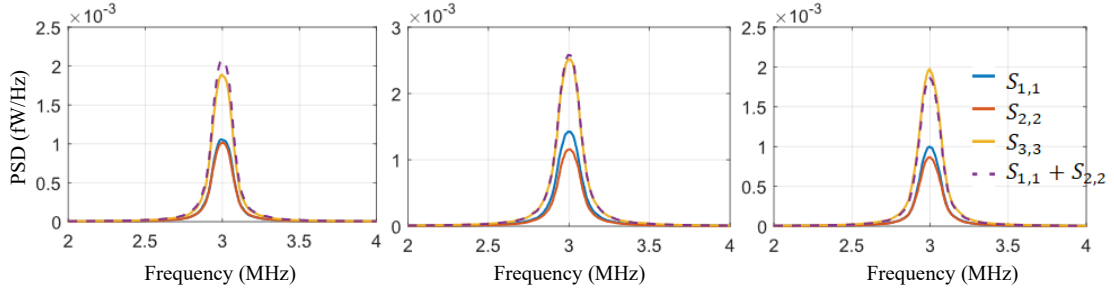


Figure 5.1: The PSD with different detuning (a) $\Delta/2\pi = -0.75$ GHz (b) $\Delta/2\pi = 0$ (c) $\Delta/2\pi = 0.75$ GHz. $\theta = 0^\circ$, probe power 0.1 mW. Time duration $50/\gamma_r$ and discretization time of the evolution is $1/50\Delta$.

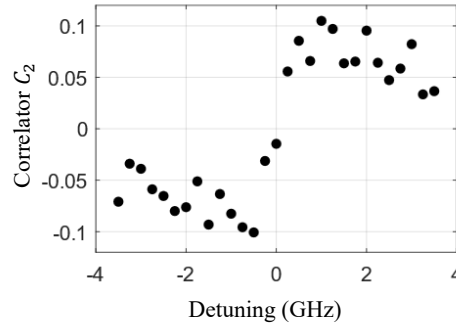


Figure 5.2: The correlator C_2 obtained through Eq. 5.6 as a function of detuning.

FR and ellipticity noise are partially correlated at detuning 0.75 GHz. Figure 5.2 shows that correlation C_2 tends to be zero for large detunings and at resonance whereas it has non-zero values for intermediate detunings. This simulation result validates our initial expectation. Only when both birefringence and dichroism exist, rotation and ellipticity have correlations. Furthermore, the detuning behavior of correlator C_2 is anti-symmetric with respect to the resonance center, just like the dispersion curve. These features prove the point that the correlated parts of the rotation noise and the ellipticity noise come from the birefringence and dichroism associated with the same mechanism, and are not associated with correlations between different noise mechanisms.

Figure 5.3 shows the MSC of rotation noise and ellipticity noise for different detunings. The results are consistent with Fig. 5.1 and Fig. 5.2. MSC is bigger for moderate detunings (0.75 GHz, 1.5 GHz) than for large detunings (3.5 GHz) and at resonance. In addition, MSC has a local maximum at Larmor frequency 3 MHz, which means that rotation and ellipticity noises are more correlated at this eigenfrequency.

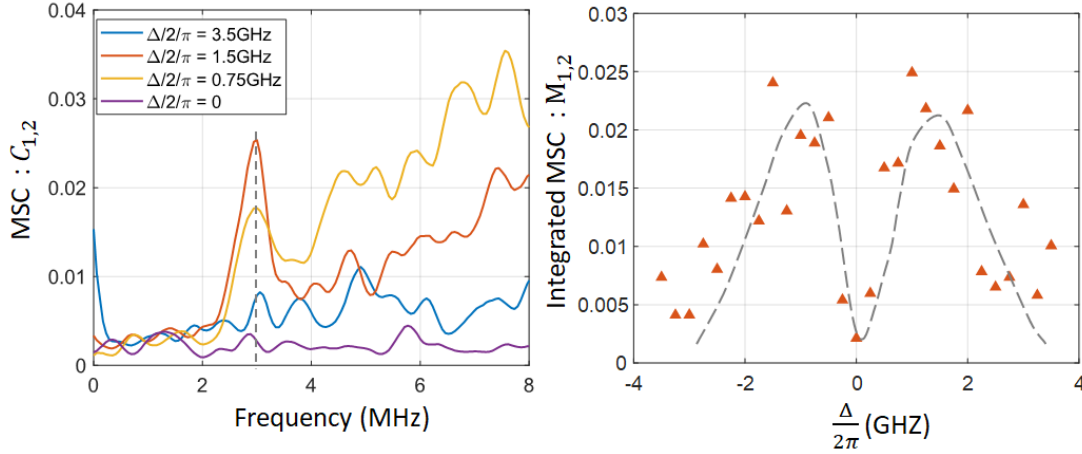


Figure 5.3: MSC (a) and integrated MSC (b) of rotation noise and ellipticity noise ($\theta = 0^\circ$) under different detunings. The dotted line of (b) is only for eye guiding.

5.2.2 Case where $\theta = 45^\circ$

As the SNS has a strong θ dependence, it is interesting to study the correlation as the function of θ . The situation will become more complicated as there are two resonances at ω_L and $2\omega_L$ when $\theta = 45^\circ$.

Figure 5.4 shows the PSD of $\theta_i(t)$, $i = 1, 2, 3$. Here we find that for intermediate detunings (Fig. 5.4(a) and (c)), the difference $S_{3,3} - (S_{1,1} + S_{2,2})$ is much bigger than in the case $\theta = 0^\circ$. And this difference vanishes at resonance as shown in Fig. 5.4 (b), which is the same as the case $\theta = 0^\circ$.

Another interesting result is that the correlators at frequencies ω_L and $2\omega_L$ always have opposite signs. This is shown more clearly in Fig. 5.5. These opposite correlations at ω_L and $2\omega_L$ will be explained later. The detuning behavior of the correlator C_2 has an anti-symmetric shape like a dispersion curve.

Figure 5.6 shows the MSC $M_{1,2}$ and integrated MSC $M_{1,2}$. Similarly, for large detunings and at resonance, as Fig. 5.6(b) shows, the correlation disappears. From Fig. 5.6(a) we can see that at zero, Larmor ω_L , and double Larmor frequency $2\omega_L$, MSC is almost one. These are exactly the characteristic frequencies of the spin noise spectrum.

These simulations show that FR and ellipticity noise are partially correlated in both cases $\theta = 0^\circ$ and $\theta = 45^\circ$. The correlation is always stronger when the detuning is moderate no matter θ . The difference between the two cases is that the correlation is much stronger when $\theta = 45^\circ$ compared with $\theta = 0^\circ$. To understand the reason behind it, we resort to the eight types of spin noise mechanisms seen in Chapter 4.

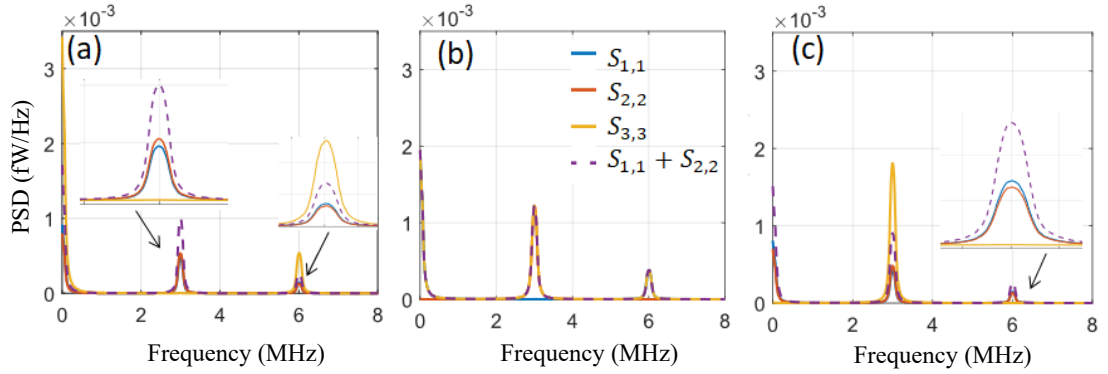


Figure 5.4: Spin noise PSD with different detunings (a) $\Delta/2\pi = -0.75$ GHz (b) $\Delta/2\pi = 0$ (c) $\Delta/2\pi = 0.75$ GHz. $\theta = 45^\circ$, probe power 0.1 mW. The inserts are zooms. Time duration $50/\gamma_r$ and discretization time of the evolution is $1/50\Delta$.

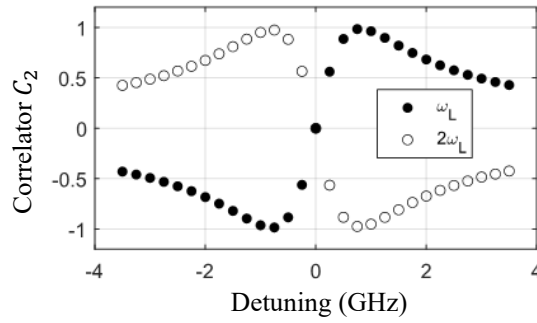


Figure 5.5: Correlator C_2 for resonances centered at ω_L and $2\omega_L$ as a function of the detuning.

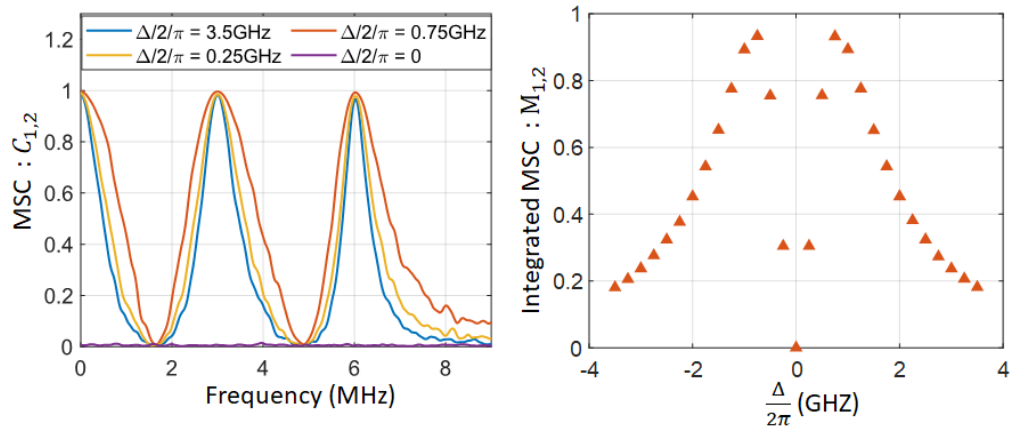


Figure 5.6: (a) MSC and (b) integrated MSC of rotation noise and ellipticity noise ($\theta = 45^\circ$) under different detunings. Welch's method is utilized to reduce the high variance of MSC.

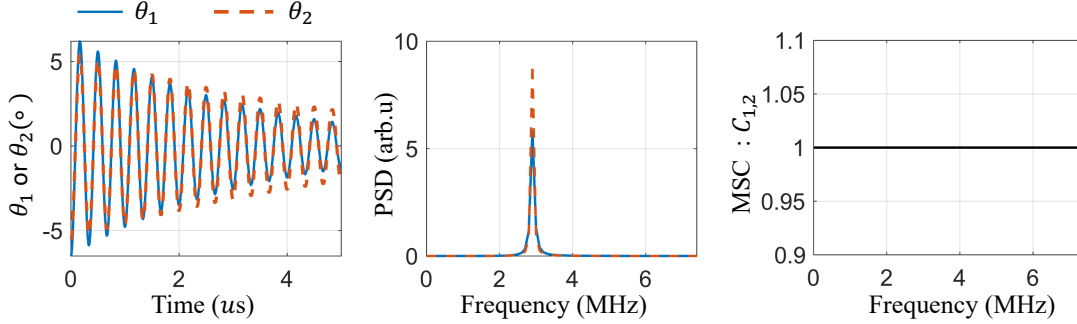


Figure 5.7: Rotation θ_1 and ellipticity θ_2 oscillation of the probe beam detuned by 0.75 GHz at $\theta = 0^\circ$. Initial state of the system corresponds to mode \hat{M}_1 only with $\lambda_1 = 2/3$.

5.3 Interpretation of correlations in terms of spin noise modes

5.3.1 Weak correlation at $\theta = 0^\circ$

We should notice that even with a well chosen detuning, the two kinds of noise are only weakly correlated when $\theta = 0^\circ$ as shown in Fig. 5.2 and Fig. 5.3. In fact, such a weak correlation is unexpected. Indeed, any spin noise mode is expected to generate both ellipticity noise and rotation noise for intermediate detunings. For example, with $\theta = 0^\circ$ and $\Delta/2\pi = 0.75$ GHz, the rotation noise comes from CB due to spin noise modes \hat{M}_1 and \hat{M}_3 and LD with u/v neutral axes due to spin noise modes \hat{M}_5 and \hat{M}_6 . Ellipticity noise comes from CD due to spin noise modes \hat{M}_1 and \hat{M}_3 and LB with u/v neutral axes due to spin noise modes \hat{M}_5 and \hat{M}_6 . Therefore, FR and ellipticity should be strongly correlated.

Let us consider the simulation with $\theta = 0^\circ$ and 0.75 GHz detuning as an example to explain this weak linear correlation.

Rotation and ellipticity noises caused by the same spin noise mode are totally correlated with MSC equal to one. As an example of this case, Fig. 5.7 shows the rotation θ_1 and ellipticity θ_2 oscillation of a probe with 0.75 GHz detuning polarized at $\theta = 0^\circ$ passing through the spin system with only mode \hat{M}_1 initially excited with $\lambda_1 = \frac{2}{3}$. When the ensemble oscillates coherently, the rotation and ellipticity caused by the spin system are perfectly correlated with MSC=1 and correlation coefficient $\bar{\rho}_{1,2} = 1$.

However, mode \hat{M}_1 is usually not alone and all noise modes must be considered. For example, Fig. 5.8 shows the evolution of the rotation $\theta_1(t)$ and ellipticity $\theta_2(t)$ with only one of the modes $\hat{M}_1, \hat{M}_3, \hat{M}_5$ or \hat{M}_6 initially excited. Obviously, $\theta_1(t)$ and $\theta_2(t)$ are either correlated with $\bar{\rho}_{1,2} = 1$ (\hat{M}_1, \hat{M}_3) or anti-correlated with $\bar{\rho}_{1,2} = -1$ (\hat{M}_5, \hat{M}_6).

In reality, spin fluctuation includes all kinds of spin noise modes. The phase shifts

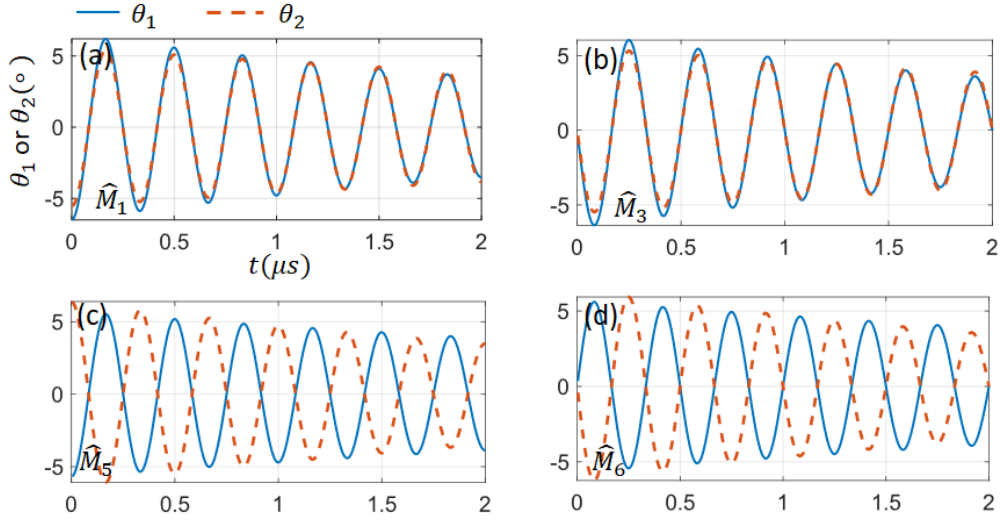


Figure 5.8: The rotation θ_1 and ellipticity θ_2 oscillation of a 0.1 mW probe with 0.75 GHz detuning polarized at $\theta = 0^\circ$ passing through the spin system with only mode \hat{M}_1 (a), \hat{M}_3 (b), \hat{M}_5 (c) and \hat{M}_6 (d) initially excited with $\lambda_1 = \frac{2}{3}$.

between $\theta_1(t)$ and $\theta_2(t)$ are different for the different noise mechanisms, the simultaneous excitation of all these mechanisms contributes to reducing the correlation between θ_1 and θ_2 .

For example, suppose that rotation and ellipticity noises arise from the fluctuations that involve different mechanisms, such as \hat{M}_1 and \hat{M}_5 .

$$\hat{f}(t) = \lambda_1(t)\hat{M}_1 + \lambda_5(t)\hat{M}_5. \quad (5.15)$$

The variance of $\lambda_1(t)$ and $\lambda_5(t)$ is the same and is equal to σ^2 . The generated random signals $\theta_1(t)$ and $\theta_2(t)$ are

$$\begin{aligned} \theta_1(t) &= a\lambda_1(t) + b\lambda_5(t) \\ \theta_2(t) &= c\lambda_1(t) + d\lambda_5(t). \end{aligned} \quad (5.16)$$

Parameters a , b , c , and d indicate the linear relation between the generated signals and the spin fluctuations. Then the covariance of θ_1 and θ_2 is

$$\begin{aligned} \text{Cov}(\theta_1, \theta_2) &= \langle \theta_1 \cdot \theta_2 \rangle \\ &= (ac + bd + ad + bc)\sigma^2. \end{aligned} \quad (5.17)$$

If the parameters a , b , c , and d have opposite signs, the resulting covariance tends to be zero. As a result, the correlation between rotation and ellipticity tends to be zero when $\theta = 0^\circ$.

5.3.2 Strong correlation at $\theta = 45^\circ$

When $\theta = 45^\circ$, the caused rotation and ellipticity come from mechanisms $\hat{M}_1, \hat{M}_3, \hat{M}_4, \hat{M}_7, \hat{M}_8$.

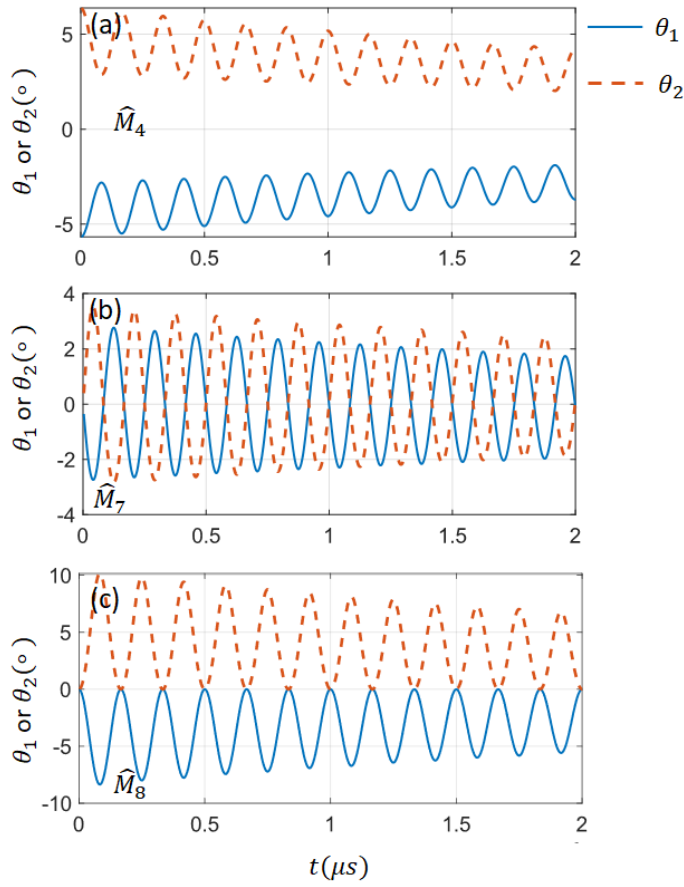


Figure 5.9: The rotation θ_1 and ellipticity θ_2 oscillation of a 0.1 mW probe with 0.75 GHz detuning polarized at $\theta = 45^\circ$ passing through the spin system with only mode \hat{M}_4 (a), \hat{M}_7 (b) and \hat{M}_8 (c) initially excited with $\lambda_4 = \frac{2}{3}$, $\lambda_7 = \frac{2}{3}$ and $\lambda_8 = -\frac{\sqrt{3}}{3}$, respectively.

More precisely, one observes that:

- 1) At ω_L , the rotation noise and the ellipticity noise arise from CB or CD respectively due to fluctuation modes \hat{M}_1 and \hat{M}_3 . A mixture of \hat{M}_1 and \hat{M}_3 does not cancel the correlation since they both produce rotation and ellipticity noise with a positive correlation as shown in Figs. 5.8 (a) and (b).
- 2) At $2\omega_L$, the rotation noise and the ellipticity noise arise from LD or LB respectively due to fluctuation modes \hat{M}_4 , \hat{M}_7 and \hat{M}_8 . A mixture of fluctuations \hat{M}_4 , \hat{M}_7 , and \hat{M}_8 does not cancel the correlations since they both produce rotation and ellipticity noise with anti-correlation as shown in Fig. 5.9.

From Fig. 5.9 and Fig. 5.8(a)(b), we can solve the question to know why noises of ω_L and $2\omega_L$ have opposite correlators C_2 . The origin of this phenomenon lies in the positive correlations for mechanisms \hat{M}_1 and \hat{M}_3 observed at ω_L and the negative correlations for mechanisms \hat{M}_4 , \hat{M}_7 and \hat{M}_8 observed at $2\omega_L$.

In summary, the correlation of rotation and ellipticity noises at $\theta = 45^\circ$ is much stronger than at $\theta = 0$. The θ dependence of the correlation is depicted in Figure 5.10. At $\theta = 45^\circ$, the correlation is maximum and tends to be zero as θ approaches 0° and 90° .

5.4 Proposed experiment

In order to test these predictions, we propose the following experiment to record the rotation and ellipticity noises simultaneously. An extra balanced detection system is required as shown in Fig. 5.11. After the cell, the probe beam is split by a 50:50 beam splitter. Both beams carry the polarization noise information with half power. One path is similar to the END set-up to record the ellipticity noise and the other one is similar to the RND set-up to record the rotation noise. The two signals, acquired simultaneously by a multichannel oscilloscope, can then be further processed to extract the correlations.

5.5 Conclusion

In this chapter, we have numerically predicted the correlations between FR noise and ellipticity noises with varying detunings and angles θ . The correlation is predicted to exist for intermediate detunings when there are both birefringence and dichroism. Surprisingly, the correlation has a strong θ dependence. When the noise source contains several different mechanisms, the correlation between rotation and ellipticity noise is predicted to be strongly attenuated.

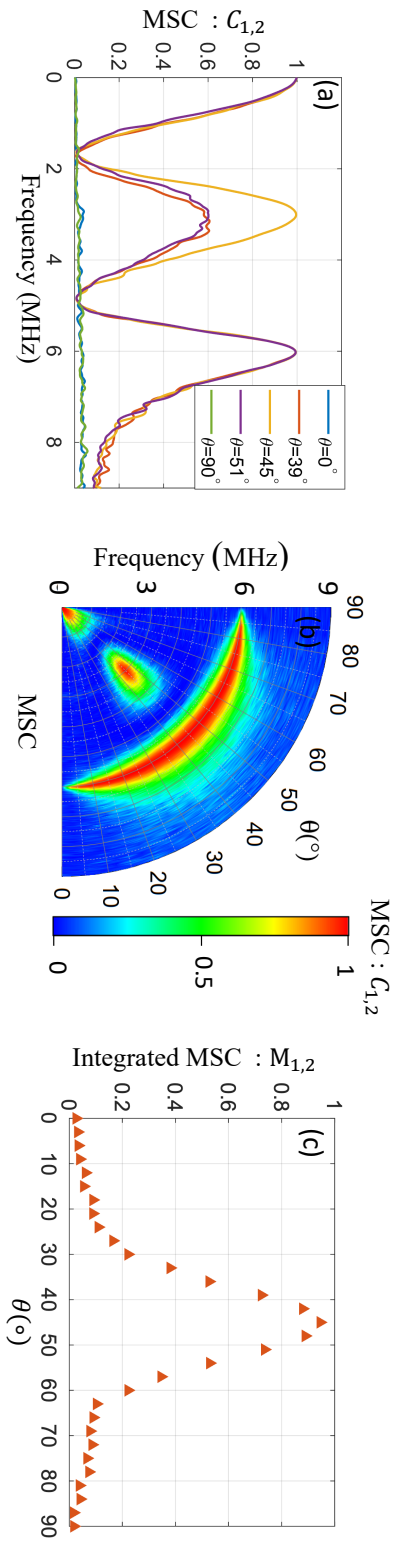


Figure 5.10: MSC (a,b) and integrated MSC (c) of rotation noise and ellipticity noise ($\Delta/2\pi = 0.75$ GHz) with different θ .

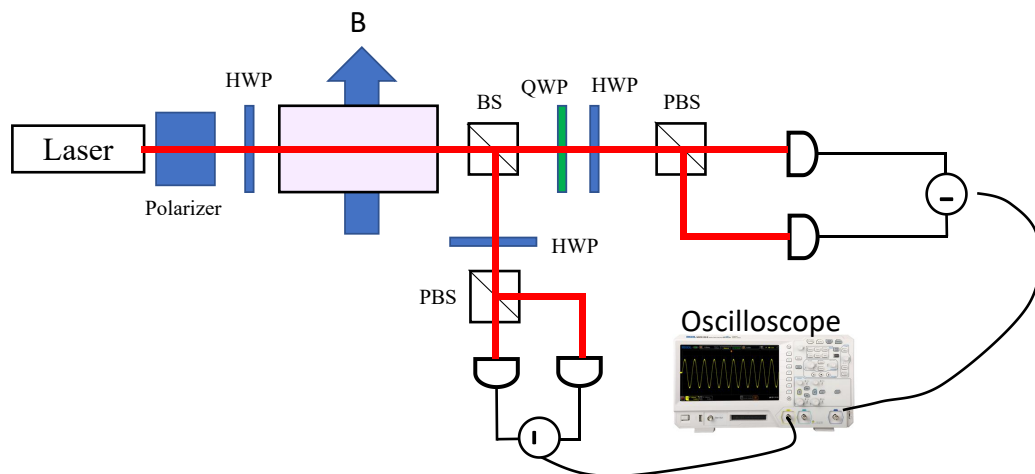


Figure 5.11: Schematic of the experimental set-up for correlation measurement. The FR and ellipticity noises are recorded by an oscilloscope at the same time.

Chapter 6

SNS in the presence of magnetic noise

Contents

6.1 Modeling the magnetic noise	74
6.1.1 Fluctuating Larmor frequency	75
6.1.2 SNS simulation in the presence of magnetic noise	75
6.2 Simulation results with varying noise bandwidth	77
6.3 Interpretation in terms of oscillation modes	77
6.4 Experimental Noise Calibration	80
6.5 Conclusion	81

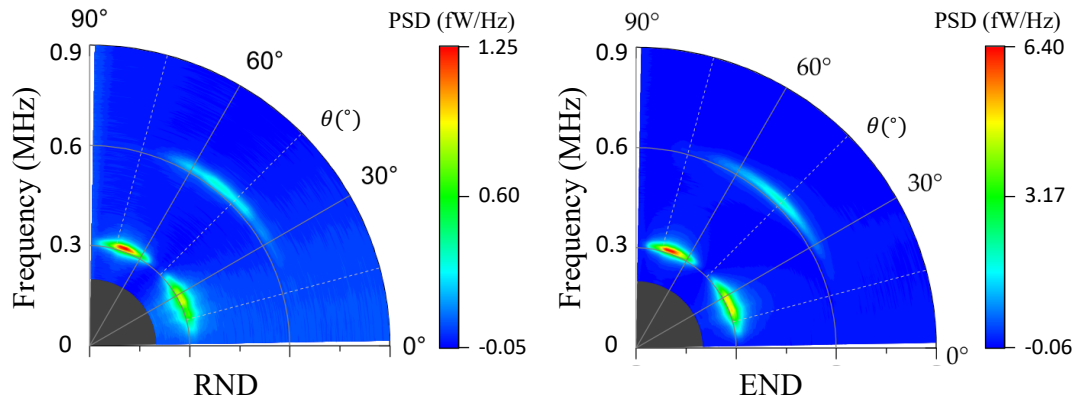


Figure 6.1: Experimental results of θ dependence of (a) Faraday rotation and (b) ellipticity of SNS when the set-up is not stable.

SNS is expected to be sensitive to magnetic field noise, as this noise can for sure enlarge the resonances and eventually wash them out. However, we observe that magnetic noise can have some other effects on the resonances. Indeed, it can also be a source of spin noise signals different from the noise coming from the transit. If the B-field fluctuates, it can contain the frequency components that can couple the Zeeman sublevels. In the present chapter, we present such initially surprising experimental results and show that they can be modeled by taking into account the presence of magnetic field noise.

Figure 6.1 shows the experimental results originally recorded by Pascal Neveu during his Ph.D. We can see that the polarization dependence is very different from the one we have shown in the previous chapters. When these data were recorded, the experiment was in a lab subjected to many electromagnetic perturbations. In this chapter, we show that the shape of the SNS resonances of Fig. 6.1 can indeed be reproduced if one introduces magnetic noise.

Before simulating the magnetic noise, it is important to clarify that the observed polarization pattern can have various sources, and magnetic field noise is just one of them. The experimental process itself, including platform vibrations and laser noise, can also impact the results. In the simulations that follow, we successfully demonstrate that magnetic field noise tends to strengthen the observed pattern.

6.1 Modeling the magnetic noise

Here we consider a noisy magnetic field with fluctuating amplitude. The direction is supposed to be fixed.

6.1.1 Fluctuating Larmor frequency

The generated magnetic field $B(t)$ is proportional to the current $I(t)$ in the Helmholtz coil. We suppose that this current has a mean value \bar{I} and a white Gaussian noise. So does the generated field $B(t)$. In the following, we call $b(t)$ the fluctuating part of the field $B(t)$.

We start from the model of Chapter 3 in which a random noise matrix $\hat{f}(t)$ is introduced after each iteration used to complete the evolution of the density matrix. Similarly, to simulate the magnetic noise, a random real value $b(t)$ is added to the average magnetic field \bar{B} at each iteration.

At every step, the Hamiltonian is thus equal to

$$H(t) = \hbar \begin{pmatrix} 0 & \frac{\omega_L(t)}{\sqrt{2}} & 0 & \frac{\Omega^{+*}}{\sqrt{3}} \\ \frac{\omega_L(t)}{\sqrt{2}} & 0 & \frac{\omega_L(t)}{\sqrt{2}} & 0 \\ 0 & \frac{\omega_L(t)}{\sqrt{2}} & 0 & -\frac{\Omega^{-*}}{\sqrt{3}} \\ \frac{\Omega^+}{\sqrt{3}} & 0 & -\frac{\Omega^-}{\sqrt{3}} & \Delta \end{pmatrix}, \quad (6.1)$$

where $\omega_L(t) = -\gamma B(t)$ with $\gamma = -eg/2m$. This Hamiltonian determines the evolution of the system using the equation

$$\frac{d\rho}{dt} = \frac{1}{i\hbar}[H(t), \rho] + \frac{1}{i\hbar}D(\rho) \quad (6.2)$$

over a time step of duration dt_b . One should notice that this discretization time is related to the bandwidth of the simulated white noise of \mathbf{B} and therefore the step duration here is a parameter that needs to be carefully considered.

6.1.2 SNS simulation in the presence of magnetic noise

Figure 6.2 shows a simulation result of SNS signal with a noisy magnetic field. One can see that the θ dependence changes a lot and becomes similar to the experiment results of Fig. 6.1. The strongest SNS signal at Larmor frequency occurs at around $\theta = 25^\circ$ and $\theta = 70^\circ$. The shapes of the noise spectra are completely different from those induced by transit noise. This θ dependence cannot be explained by the three kinds of birefringences we introduced before.

However, it is important to note that we were unable to fully replicate the experimental results in our simulations. One of the most noticeable discrepancies is that the simulated rotational noise intensity is considerably lower than observed in the experiment. Additionally, the contrasts between the strongest noises at $\theta = 25^\circ$ and $\theta = 70^\circ$ and the weakest signals at $\theta = 45^\circ$, $\theta = 0^\circ$ and $\theta = 90^\circ$ are less pronounced compared to the experimental data. As we said before, considering only magnetic field noise is not a strictly comprehensive description. Other sources of noise need to be considered in the future.

In the experiment, the transit noise of the atoms always exists. A more realistic situation would correspond to both transit and magnetic field noise existing simultaneously. As they

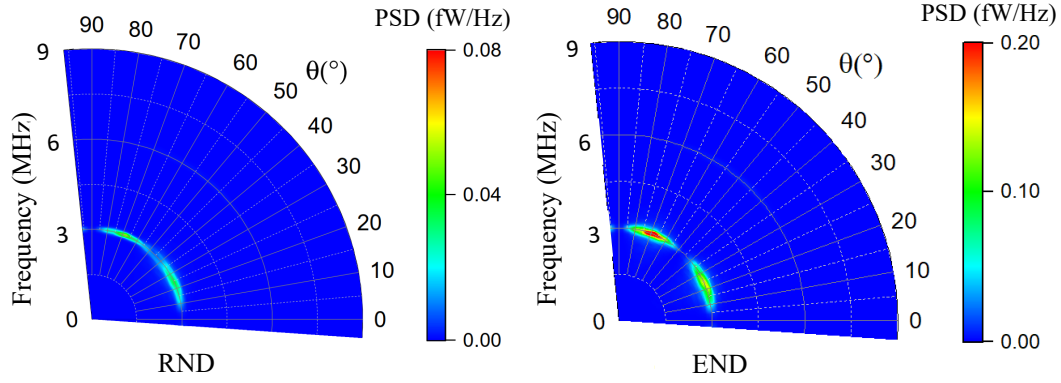


Figure 6.2: A simulation results of SNS with magnetic field noise. Transit noise is not included. The Larmor frequency is 3×10^6 Hz, the variance of the magnetic noise is $0.2 \times 3 \times 10^9$ Hz² and the bandwidth is 5 MHz. Time duration $50/\gamma_r$ and discretization time of the evolution is $1/50\Delta$.

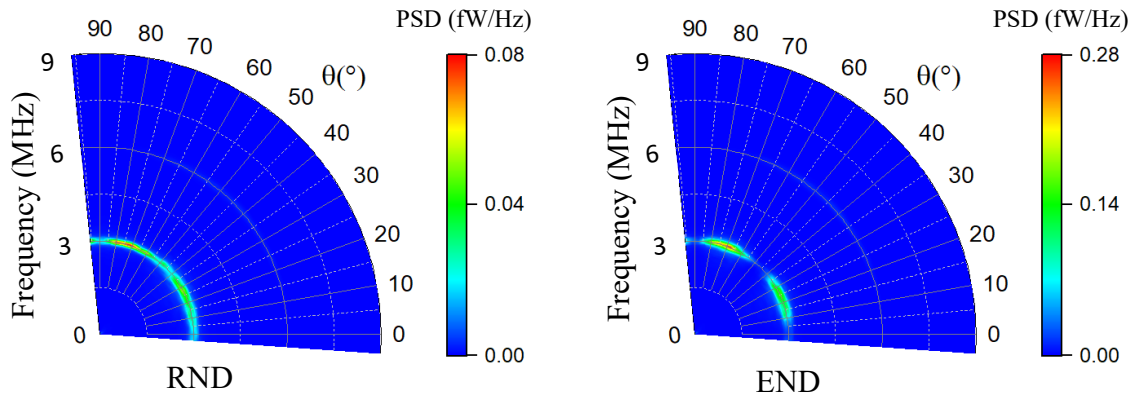


Figure 6.3: Simulated SNS with transit noise of the atoms and magnetic noise. The Larmor frequency is 3×10^6 Hz, the variance of the magnetic noise is $0.2 \times 3 \times 10^9$ Hz² and bandwidth is 5 MHz. Time duration $50/\gamma_r$ and discretization time of the evolution is $1/50\Delta$.

have different origins, and the power spectra of the two kinds of noise add incoherently. The final noise pattern depends on the relative strengths of the transit noise and $\mathbf{B}(t)$ -field noise.

We show in Fig. 6.3 what happens when we simulate the SNS with both transit noise and magnetic noise with bandwidth 5 MHz. The simulations can reproduce the ellipticity noise well, but they do not fully match the experimental results for rotational noise. Rotation has no big difference compared to the case without magnetic field noise. This is likely because magnetic field noise makes only a minor contribution to the overall rotation noise.

6.2 Simulation results with varying noise bandwidth

In the experiments and simulations, there is of course no true white noise. The bandwidth of a true white noise is infinite and so is the power it carries. We actually simulate a white noise after it has passed through a low-pass filter. The energy of the noise is not of large interest as it is clear that a larger noise gives larger fluctuations in the system. Here we focus on the role of the noise bandwidth. In the iterative comprehension of the density matrix evolution, the discretization time dt_b determines the bandwidth of the noise f_{bw} :

$$f_{bw} = \frac{1}{dt_b}. \quad (6.3)$$

This can be proved by the Wiener-Khinchin theorem.

The bandwidth of magnetic noise plays a crucial role in determining the SNS signal. Figure 6.4 depicts the SNS signal originating solely from magnetic noise with varying bandwidth but keeping the same power. Notably, the SNS signal is weak when the bandwidth falls below 3 MHz or exceeds 50 MHz, but becomes stronger when the bandwidth is around 5 MHz and 10 MHz. This relationship can be attributed to magnetic resonance, as the Larmor frequency (Zeeman splitting) is typically several MHz. Thus, when the magnetic noise exhibits more power around the Larmor frequency, the SNS signal becomes stronger.

6.3 Interpretation in terms of oscillation modes

In fact, it is surprising that some magnetic field amplitude noise can cause spin fluctuations. For a magnetic field perpendicular to the light propagation direction z , it affects the coupling strength between Zeeman sublevels quantized along z . But it does not affect the population distribution of spin states.

In this section, we try to explain this polarization dependence based on the eight noise modes theory we developed in chapter 4. The idea to understand magnetic field noise is to convert it into the noise types that we understand well: the eight moments $\hat{M}_i, i =$

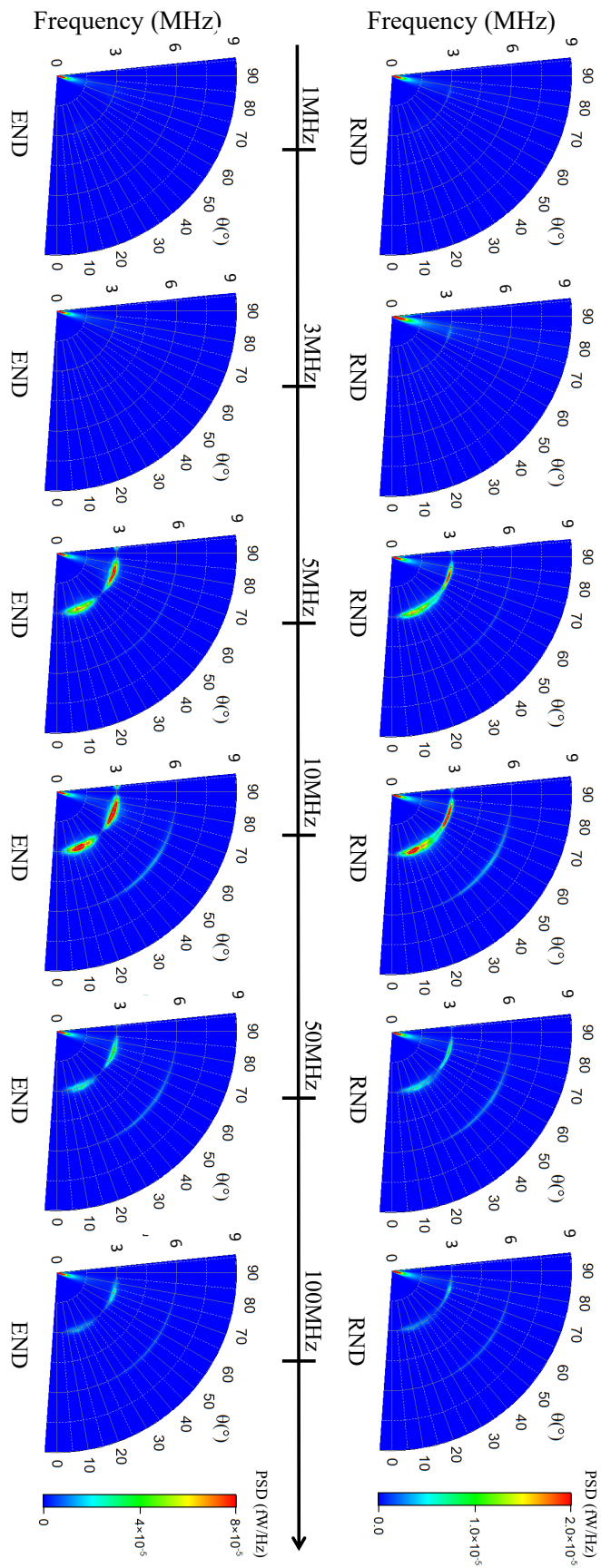


Figure 6.4: Simulated SNS with magnetic noise. The Larmor frequency is 3×10^6 Hz, the variance of the noise is $0.1 \times 3 \times 10^6$ Hz² and the bandwidth is different as shown in the figure. Time duration $50/\gamma_r$ and discretization time of the evolution is $1/50\Delta$

$1, \dots, 8$. Then our aim is to analyse the cause of the fluctuations of the spin system when the magnitude of the magnetic field changes.

The successive steps of this analysis are the following:

- 1) Simulate the density matrix of the system with true experimental parameters. After a period of time t_1 , the system becomes stable¹. Now the elements of the density matrix have constant values².
- 2) At t_1 , the magnetic field exhibits some variation and becomes $B + b$. The density matrix $\rho + d\rho'$ at $t_1 + dt$ is obtained by the Von Neumann equation. At the same time, one gets the density matrix $\rho + d\rho$ at $t_1 + dt$ without magnetic fluctuation. Then the difference $\Delta\rho = d\rho' - d\rho$ is the change of the state of the system due to magnetic noise.
- 3) Write $\Delta\rho$ in terms of the eight spin mechanisms $\hat{M}_i, i = 1, 2, \dots, 8$. Then we know which mechanisms cause the spin noise.

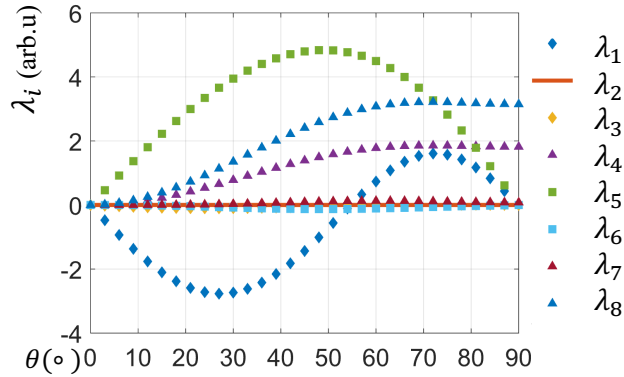


Figure 6.5: The amplitude of the spin noise modes induced by magnetic noise as a function of θ . The probe is detuned by 1.5 GHz. The input power is 1 mW. λ_i 's represent the amplitude of the different noise modes.

Using this method, Figure 6.5 shows the induced eight different spin components $\hat{M}_i, i = 1, \dots, 8$ due to magnetic field fluctuations as a function of θ with a 1mW probe. It shows that the induced spin noise mainly consists of $\hat{M}_1, \hat{M}_5, \hat{M}_7$, and \hat{M}_8 . At $\theta = 0^\circ$, all spin noise components are zero, which means that there is no fluctuation even though the magnetic field is noisy. However, at other angles θ , some of the noise modes get excited if the magnetic field is noisy. In Chapter 4, the eight noise modes \hat{M}_i were divided into three main categories leading to different birefringence: CB, LB with x/y neutral axes, LB with

¹The initial state is a thermal state. A probe with 1 mW power can induce optical pumping.

²There will be very small floats due to precision issues with MATLAB. This float can be ignored as it is several magnitude orders smaller than the considered fluctuation

u/v neutral axes. Now the θ dependence of SNS originating from magnetic noise can be explained:

- 1) \hat{M}_1 mechanism, that gives CB, plotted as blue diamonds in Fig. 6.5, is no longer independent of θ . Its maximum value occurs at around 25° and a second maximum occurs around 72° . Therefore, the induced CB noise is stronger near these angles, which is exactly the pattern depicted by the simulation of Fig. 6.4.
- 2) \hat{M}_7 and \hat{M}_8 modes give LB with x/y neutral axes. As θ increases from 0° to 90° , \hat{M}_7 and \hat{M}_8 get stronger. The induced x/y LB gets stronger when θ approaches 90° .
- 3) Among the main noise modes excited by magnetic noise, only \hat{M}_5 gives LB with neutral axes along u/v . \hat{M}_5 has a maximum value around $\theta = 50^\circ$ and becomes zero at $\theta = 0^\circ$ and $\theta = 90^\circ$. As a result, there is no ellipticity noise near $\theta = 0^\circ$ and $\theta = 90^\circ$.

6.4 Experimental Noise Calibration

Firstly, it is worth noting that magnetic field noise can originate not only from current instabilities but also from the interference of the electromagnetic field in the environment. However, for the purposes of this study, we focus on magnetic field noise resulting from current instabilities. This approach serves as a reference and support for our experimental verification of the impact of magnetic field noise in the future.

Secondly, in the simulations of this chapter, I introduced a noisy Larmor frequency. However, it is very necessary to know the noise level of a certain physical quantity of the equipment in the experiment. The Helmholtz coil that generated magnetic field is powered by a power supply (Aim TTi EX354RD). The power supply with current 1A gives 3×10^6 Hz Larmor frequency. The relation between the Larmor frequency and the current of the power supply I_s is

$$f = g_b \times I_s. \quad (6.4)$$

where $g_b = 3 \times 10^6$ Hz/A.

In the simulation code, suppose that a random value b is drawn following a Gaussian distribution $N(0, \sigma_b^2)$ for every interval dt_b with $\sigma_b^2 = 0.1 \times 3 \times 10^6$ Hz². Correspondingly, the variance of the current of the power supply is

$$\sigma_i^2 = \sigma_b^2 / g_b^2 = 0.3 \times 10^{-7} \text{A}^2. \quad (6.5)$$

The PSD of this noise current can be measured. The averaged PSD \bar{P}_i of such a noise current in duration time T can be deduced from the following equation:

$$\bar{P}_i = \frac{E_i}{T f_{iw}}, \quad E_i = \sigma_i^2 \cdot \frac{T}{dt_b} / R_e. \quad (6.6)$$

where R_e depends on the measuring equipment. Therefore one has

$$\bar{P}_i = \sigma_i^2 / R_e. \quad (6.7)$$

6.5 Conclusion

In this chapter, we have studied the effect of magnetic field amplitude noise on SNS. We have seen that the SNS pattern may change if the magnetic field is noisy. This pattern can be understood by decomposing it into the eight spin noise modes. We then find that the induced fluctuation of the system has different spin polarization components for different values θ . This work provides a new perspective for future analysis of the impact of other disturbances on SNS. However, there are still some discrepancies between the simulations and experiments. The simulated rotation noise is weaker than the experimental one. Other kinds of noise should be taken into account. Controllable magnetic noise awaits to be introduced in the experiment for a truly quantitative comparison with the simulations. Nevertheless, the work here offers insights into understanding the spin noise spectrum in noisy magnetic field and presents a potential avenue for detecting the stability of external magnetic fields.

Conclusion

The objective of this Ph.D research is to investigate new phenomena in SNS by utilizing metastable helium vapor at room temperature. The research begins by exploring the second harmonic resonance and polarization patterns of SNS.

By checking the probe detuning and the polarization direction of the probe, we point out the four main effects of a spin-1 system including circular birefringence, linear birefringence, circular dichroism, and linear dichroism. Furthermore, using the three well separated $J = 1 \rightarrow J = 0$, $J = 1 \rightarrow J = 1$, and $J = 1 \rightarrow J = 2$ transitions available in metastable ^4He , we can thus emphasize the role of the structure of the upper level of the probed transition and provide a complete understanding of the SNS of a spin-1 system. We observed different results near different transitions, and to address this phenomenon, we developed a spin-1 model. The spin-1 system can be decomposed into eight noise modes, each of which corresponds to a specific oscillation mode of a linearly polarized probe. This spin-1 model provides a clear explanation for the second harmonic resonance and polarization pattern observed in the system.

In addition, a numerical simulation model was developed, incorporating a noise operator to replicate the random fluctuations present in a spin-1 system. This simulation is capable of fitting our experimental results both qualitatively and quantitatively. Moreover, as a valuable reference, the simulation results can guide our future experiments.

By employing both the simulation model and the spin-1 model, we investigated a more complex phenomenon in SNS, namely the correlation between rotation noise and ellipticity noise. Our findings reveal that the correlation is dependent on the polarization direction and wavelength of the probe, and the spin-1 model offers an explanation for this polarization dependence. This study gives us the correlation information which is not captured by the power spectrum of rotation and ellipticity noise. The correlation between the rotation and ellipticity indicates that the two signals come from the same spin noise modes and it also provides the phase information for rotation and ellipticity. However, we must note that the correlation study in Chapter 5 is still incomplete, and the corresponding experiment is yet to be performed.

We also explored the effects of noisy magnetic fields on SNS results, which is a common occurrence in experimental settings. For the sake of simplicity, we only examined the SNS results when the amplitude of the applied magnetic field fluctuates. The spin-1 model can explain the resulting changes in polarization, which underscores its practicality. It is worth further investigating the correlation between the eight noise modes in the presence of magnetic field noise. I anticipate that the independent noise modes will display correlations with each other when subjected to magnetic field noise. However, we must emphasize that the corresponding experiment is still pending. The sensitivity of SNS to magnetic noise makes it a promising tool for magnetometry and stabilization of externally generated magnetic fields.

In this thesis, we have examined a simple spin-1 system and proposed a spin-1 model. By leveraging experiments, simulations, and analytical theory, we have demonstrated the consistency of our study. We hope that the methods and theories developed in this thesis can be extended to other systems beyond metastable helium. Just as the spin-1/2 model is not solely applicable to spin-1/2 systems, the spin-1 model can also be applied to other systems. The spontaneous spin resonance at double Larmor frequency at cesium atomic vapor has been reported recently [42, 86]. The observed results in a spin system with $F=4$ can be well explained by our spin-one model. Furthermore, as demonstrated in Chapters 5 and 6, the spin-1 model presents distinct advantages in tackling complex problems. Naturally, the viability of more extensions will be subject to further investigation and time will tell.

In spin-1, the eight noise modes can be mapped to the different kinds of birefringence effect of light. When the spin value exceeds one, additional noise modes emerge, introducing further complexity in their relation to the probing process. The possibility of observing oscillations at higher frequencies remains a puzzle, representing an intriguing area for future research.

The thesis has its limitations. We have not covered cutting-edge topics such as higher order spin correlations and correlations of different spin components, which could be the focus of future research. Reducing the number of atoms to achieve a non-Gaussian distribution can be relevant for studying higher order correlators. It is also highly interesting to observe collective effects that arise with increased density and pressure. Furthermore, the study of two-beam SNS is intriguing. We can observe the SNS changes of the system subjected to a strong pump. The presence of the pumping effect will lead to correlations between different spin states, which will also influence the spin noise results. This non-equilibrium SNS can be used to learn the pump effect in a system. The dependence on the polarization of the pump can be used to reveal the level structure.

Lastly, I hope that the research presented in this thesis will contribute to the advancement of spin noise spectroscopy.

Main results obtained in Faraday geometry

A.1 Introduction

Magneto-optical experiment can be performed with two main geometries, with the light beam travelling along (Faraday geometry) or perpendicularly to (Voigt geometry) the magnetic field. When the system is inherently anisotropic, such as low dimensional materials[96], the choice of the geometry is important since the relaxation time of the spin varies in different direction [97]. For isotropic media, such as an atomic vapor, most SNS experiments use Voigt geometry to avoid technical noise. In Faraday geometry, the spectrum of spin orientation noise is centered at zero frequency as I will show in this appendix. The measurement is then made difficult by the technical noise at low frequencies. Furthermore, SNS in Faraday geometry lacks information on magnetic splitting, which is critical for spin system characterization.

Nevertheless, there is still valuable information available with the Faraday geometry [42, 43, 90], such as the relaxation time of the system as function of the applied longitudinal magnetic field and temperature [98]. This appendix shows the main SNS results of metastable helium in the Faraday geometry.

A.2 Spin oscillation frequency in Faraday geometry

Here I still use the quantization direction along z , i.e. along the light propagation direction. The quantum operators are expressed in the atomic basis $\{|-1\rangle_z, |0\rangle_z, |1\rangle_z\}$.

The Schrodinger equation for a spin-1 system with a magnetic field along z is

$$\frac{i}{\hbar} \frac{d|\psi\rangle}{dt} = H_B |\psi\rangle, \text{ where } H_B = \hbar\omega_L \begin{bmatrix} -1 & 0 & 0 \\ 0 & 0 & 0 \\ 0 & 0 & 1 \end{bmatrix}. \quad (\text{A.1})$$

H_B has three eigen-values, $-\hbar\omega_L$, 0 and $\hbar\omega_L$, associated with the eigenstates $|-1\rangle_z$, $|0\rangle_z$, $|+1\rangle_z$, respectively. The solution of the Schrodinger equation can be written as a linear combination of the three eigenstates with coefficients C_i that depends on the initial state:

$$|\psi\rangle = C_1 e^{i\omega_L t} |-1\rangle_z + C_2 |0\rangle_z + C_3 e^{-i\omega_L t} |+1\rangle_z. \quad (\text{A.2})$$

The population difference between the two levels $|-1\rangle_z$ and $|+1\rangle_z$ is

$$\Delta\rho_{-1,1} = |C_1|^2 - |C_3|^2. \quad (\text{A.3})$$

The population unbalance between level $|-1\rangle_z$ and $|+1\rangle_z$ will not evolve under the influence of the longitudinal magnetic field for any initial condition. It is quite obvious that the eigenstates of the Hamiltonian do not evolve over time. This also means that the spectrum of spin orientation fluctuations is centered at zero frequency. As a result, CB and CD noises will never contribute to any non-zero frequency resonances.

In the linear basis $\{|\Psi\rangle_x, |0\rangle_z, |\Psi\rangle_y\}$, the solution of Eq. (A.2) becomes

$$|\psi'\rangle = \mathcal{M}_g |\psi\rangle = \begin{bmatrix} C_1/\sqrt{2}e^{i\omega_L t} + C_3/\sqrt{2}e^{-i\omega_L t} \\ C_2 \\ -iC_1/\sqrt{2}e^{i\omega_L t} + iC_3/\sqrt{2}e^{-i\omega_L t} \end{bmatrix}, \quad (\text{A.4})$$

with

$$\mathcal{M}_g = \begin{bmatrix} \frac{1}{\sqrt{2}} & 0 & \frac{1}{\sqrt{2}} \\ 0 & 1 & 0 \\ -\frac{i}{\sqrt{2}} & 0 & \frac{i}{\sqrt{2}} \end{bmatrix}, \quad |\psi\rangle = \begin{bmatrix} C_1 e^{-i\omega_L t} \\ C_2 \\ C_3 e^{i\omega_L t} \end{bmatrix}. \quad (\text{A.5})$$

The population difference between the two levels $|\Psi\rangle_x$ and $|\Psi\rangle_y$ is

$$\Delta\rho_{x,y} = C_1 C_3^* e^{i2\omega_L t} + c.c = 2|C_1 C_3| \cos(2\omega_L t + \varphi_{31}). \quad (\text{A.6})$$

where φ_{31} is the phase difference between C_1 and C_3 . The population difference $\rho_{xx} - \rho_{yy}$ has a component oscillating at $2\omega_L$. This means that we can observe the spin noise spectrum centered at $2\omega_L$ due to the LB or LD noises with neutral axes along x and y .

Finally, the solution of Eq. (A.2) in the linear basis $\{|\Psi_u\rangle, |0\rangle_z, |\Psi_v\rangle\}$ is

$$|\psi''\rangle = \mathcal{M}_g |\psi\rangle = \begin{bmatrix} \frac{1+i}{2}C_1 e^{i\omega_L t} + \frac{1-i}{2}C_3 e^{-i\omega_L t} \\ C_2 \\ \frac{1-i}{2}C_1 e^{i\omega_L t} + \frac{1+i}{2}C_3 e^{-i\omega_L t} \end{bmatrix}, \quad (\text{A.7})$$

with

$$\mathcal{M}_g = \frac{1}{2} \begin{bmatrix} 1+i & 0 & 1-i \\ 0 & 2 & 0 \\ 1-i & 0 & 1+i \end{bmatrix}, \quad |\psi\rangle = \begin{bmatrix} C_1 e^{-i\omega_L t} \\ C_2 \\ C_3 e^{i\omega_L t} \end{bmatrix}. \quad (\text{A.8})$$

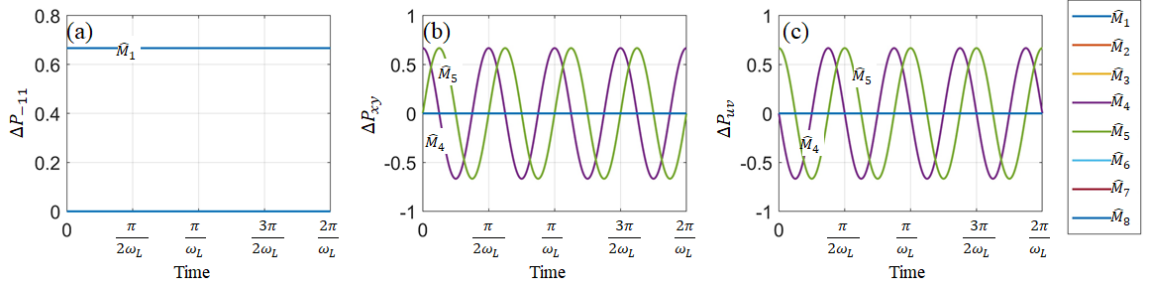


Figure A.1: Evolution of the population difference of the two relevant levels (a) $|{-1}\rangle_z$ and $|1\rangle_z$ (b) $|\Psi_x\rangle$ and $|\Psi_y\rangle$ (c) $|\Psi_u\rangle$ and $|\Psi_v\rangle$. All eight spin mechanisms $\hat{M}_i, i = 1, 2, \dots, 8$ are excited but only three of them contribute to population imbalance: the population differences are zero for the noise modes $\hat{M}_2, \hat{M}_3, \hat{M}_6, \hat{M}_7$ and \hat{M}_8 . The eight initial states are obtained by Eq. 4.1.

The population difference between the two levels $|\Psi\rangle_u$ and $|\Psi\rangle_v$ is

$$\Delta\rho_{u,v} = iC_1C_3^*e^{-i2\omega_L t} + c.c = 2|C_1C_3| \cos\left(2\omega_L t + \varphi_{31} - \frac{\pi}{2}\right). \quad (\text{A.9})$$

The population difference $\rho_{u,v}$ oscillates at the double Larmor frequency. The spin noise spectrum thus has a resonance at $2\omega_L$ coming from LB or LD noises with neutral axes along u and v .

Conclusion :

- 1) CB noise under Faraday geometry is centered at zero frequency. This makes CB noise difficult to observe in such an experiment.
- 2) For a spin-one system, SNS has a $2\omega_L$ resonance due to the LB noise, which is very different from the spin-1/2 model, for which there is only one resonance centered at zero. The isotropy of the geometry makes this resonance independent of the polarization input direction.
- 3) LB with x/y neutral axes and LB with u/v neutral axes have the same resonance at $2\omega_L$ as shown in Eqs. (A.6) and (A.9). The unbalanced population contribute equally to both LB noise mechanism, with a $\pi/2$ phase shift.

A.3 The evolution of the eight spin noise modes

Figure A.1 shows the evolution of the population difference of the two relevant levels for the eight different initial states \hat{M}_i . These initial states are obtained by Eq. 4.1. The initial states are $\rho(0) = \frac{1}{3}\hat{\mathbb{I}} + \frac{1}{3}\hat{M}_i$ with $\lambda_i = 2/3 (i = 1, 2, \dots, 8)$.

In Figure A.1(a), the \hat{M}_1 mode gives a non-zero population difference ΔP_{-11} that remains constant while all the other modes give zero population differences. \hat{M}_4, \hat{M}_5 states

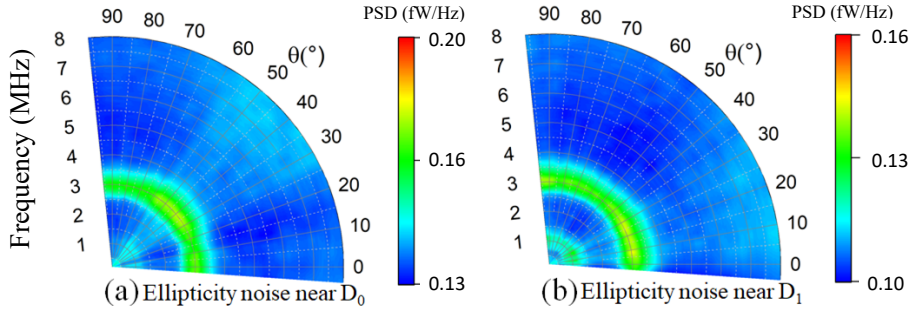


Figure A.2: Ellipticity noise obtained with a 1.5 mW probe laser. (a) 1.5 GHz blue detuned from the D_0 line. (b) 2 GHz blue detuned from the D_1 line. Spin noise resonances are centered at $2\omega_L/2\pi = 3$ MHz. (The remaining signal below 1 MHz is coming from technical noises).

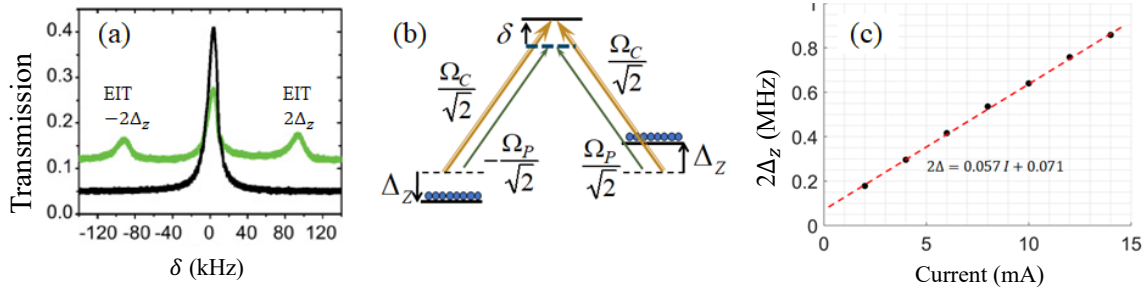


Figure A.3: (a) Transmission of the probe beam in the EIT experiment as a function of the detuning. The transparency windows occur for detunings $\delta = \pm 2\Delta_z$. The black curve is obtained without any \mathbf{B} field, and the green one with a longitudinal magnetic field providing a $2\Delta_z$ equals of about 80kHz. (b) The level structure and Zeeman splittings of the EIT experiment. (c) The frequency $2\Delta_z$ as function of the current in the solenoid providing the longitudinal magnetic field.

both lead to population differences ΔP_{xy} and ΔP_{uv} oscillations at $2\omega_L$ and all other noise modes give zero population differences.

A.4 Experimental results and simulations

No rotation noise is observable in the experiment, which is consistent with the fact that the CB noise is centered at zero frequency. The ellipticity noise can be observed near the D_0 and D_1 lines, as shown in Figure A.2, but not near the D_2 line. Indeed, when the probe is tuned near D_2 , it exhibits a much weaker LB noise due to the multi-level structure of the upper levels as explained in the case of the Voigt geometry (Chapter 4). The probe power is 1.5 mW and the experiment is performed with detunings 1.5 GHz from the D_0 line and 2 GHz from the D_1 line. The longitudinal magnetic field $\mathbf{B} = B_z \mathbf{z}$ is generated

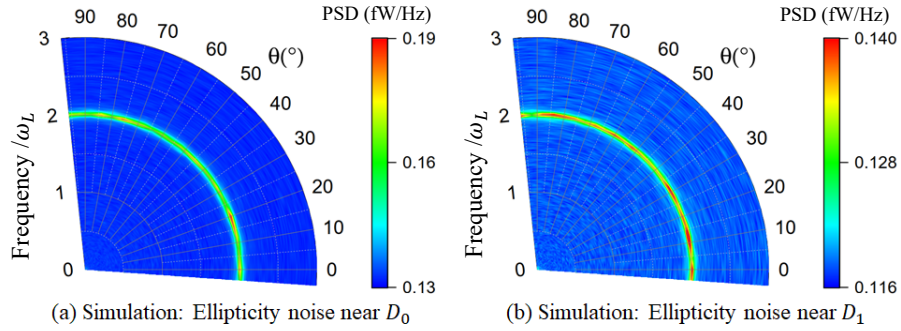


Figure A.4: Numerical simulations of the PSD of the ellipticity noise obtained with $\Omega/2\pi = 40$ MHz and light frequencies (a) a 1.5 GHz blue detuned from the D_0 line. (b) a 2 GHz blue detuned from the D_1 line. Spin noise resonances are centered at $2\omega_L/2\pi = 6$ MHz. The background noise is simulated according to the transmitted probe power (1.1 mW and 0.95 mW near D_0 and D_1).

by a solenoid with a current $I \simeq 50$ mA corresponding to a Larmor frequency of about 1.5 MHz. The \mathbf{B} field value was calibrated using Electromagnetic induced transparency (EIT) resonances as shown in Fig. A.3. The black curve is obtained without any magnetic field, while the green one was recorded in the presence of a longitudinal one. Indeed, the $|\pm 1\rangle_z$ are shifted by the Zeeman splitting Δ_z , leading to a shift of $2\Delta_z$ for the 2 photon EIT resonances. The remaining transmission window at $\delta = 0$ kHz is due to coherent population oscillation [99]. We could thus plot the $2\Delta_z$ shift of the EIT resonances as a function of the current in the solenoid Fig. A.3 (c). We could not go as high as 50 mA, because the available frequency ramp for the EIT experiment could not exceed 1 MHz. But the linear fit allows us to find that a current of 50 mA corresponds to $2\Delta_z = 3$ MHz.

Figure A.4 shows the corresponding simulation results. The experimental results are consistent with the theory. Indeed, we cannot see any orientation noise. The only discrepancy is that the resonances are much thinner than the experimental ones, which can easily be explained by the inhomogeneities of the \mathbf{B} field along z .

The spin noise of spin 1/2 system

B.1 Spin-1/2 system in a magnetic field

In this section, we present a simpler case: the spin- $\frac{1}{2}$ system. It is a widely accepted approach to describe the interaction between light and matter in atomic and semiconductor systems [84, 85].

The quantization direction is here along z , ie, the light propagation direction. The spin operators along z , x and y axis are

$$S_z = \frac{\hbar}{2} \begin{bmatrix} 1 & 0 \\ 0 & -1 \end{bmatrix}, \quad S_x = \frac{\hbar}{2} \begin{bmatrix} 0 & 1 \\ 1 & 0 \end{bmatrix}, \quad \text{and} \quad S_y = \frac{\hbar}{2} \begin{bmatrix} 0 & -i \\ i & 0 \end{bmatrix}, \quad (\text{B.1})$$

respectively. The Hamiltonien of the spin-1/2 system in a magnetic field reads

$$H = H_0 + \gamma \mathbf{B} \cdot \hat{\mathbf{S}}, \quad (\text{B.2})$$

where

$$\gamma = -g \frac{q}{2m_e c} \quad (\text{B.3})$$

and H_0 is the unperturbed atomic Hamiltonian, g is the Lande factor, \mathbf{B} is the applied magnetic field and $\hat{\mathbf{S}}$ is the spin operator of the electron. With $\mathbf{B} = B_x \mathbf{x}$, the magnetic interaction Hamiltonien H_B is

$$H_B = \frac{1}{2} \hbar \omega_L \begin{bmatrix} 0 & 1 \\ 1 & 0 \end{bmatrix}, \quad \text{with} \quad \omega_L = \gamma B_x. \quad (\text{B.4})$$

The evolution of the spin system in the magnetic field can be described by the Schrodinger equation

$$i\hbar \frac{d|\psi\rangle}{dt} = H_B |\psi\rangle. \quad (\text{B.5})$$

H_B has two eigen values, $-\frac{1}{2}\hbar\omega_L$, and $\frac{1}{2}\hbar\omega_L$, associated to the following eigen vectors respectively:

$$\begin{aligned} |v_1\rangle &= \frac{1}{\sqrt{2}}(|-1/2\rangle_z - |1/2\rangle_z), \\ |v_2\rangle &= \frac{1}{\sqrt{2}}(|-1/2\rangle_z + |1/2\rangle_z). \end{aligned} \quad (\text{B.6})$$

Any solution of the Schrodinger equation can be written as a linear combination of the two eigen vectors $|v_1\rangle$ and $|v_2\rangle$, with coefficients C_1 and C_2 which depend on the initial state:

$$|\psi(0)\rangle = C_1 e^{i\frac{1}{2}\omega_L t} |v_1\rangle + C_2 e^{-i\frac{1}{2}\omega_L t} |v_2\rangle. \quad (\text{B.7})$$

B.1.1 Spin-1/2 decomposition

The population differences of the levels interacting with the two orthogonal polarized states lead the birefringence or dichroism .

The population difference between the states $|-1/2\rangle_z$ and $|1/2\rangle_z$ can be obtained from Eq. (B.7) and reads

$$\Delta P = \rho_{-\frac{1}{2},-\frac{1}{2}} - \rho_{\frac{1}{2},\frac{1}{2}} = 2|C_1 C_2| \cos(\omega_L t - \varphi_{12}). \quad (\text{B.8})$$

where φ_{12} is the phase difference between C_1 and C_2 . The population difference between the states $|-1/2\rangle_z$ and $|1/2\rangle_z$ undergoes oscillations at ω_L under the influence of a transverse magnetic field $\mathbf{B} = B_x \mathbf{x}$ except when C_1 or C_2 is zero. This occurs when the initial state $|\psi\rangle$ is one of the eigenstates of H_B . The population is then evenly distributed between the two states and $\Delta P = 0$ and does not oscillate.

The above description clearly shows the importance of the initial state. We thus now consider different initial states to get the corresponding oscillation modes. The most general density matrix ρ can be constructed from the spin operators $\hat{\mathbf{S}}$:

$$\rho = \frac{1}{2}(\mathbb{I} + \mathbf{a} \cdot \hat{\mathbf{S}}), \quad (\text{B.9})$$

where $\mathbf{a} = (a_x, a_y, a_z)$ is a real vector, which indicates the spin polarization (or spin orientation) of the system. We can consider different initial states with different values of \mathbf{a} :

$$\rho_0^z = \begin{bmatrix} 1 & 0 \\ 0 & 0 \end{bmatrix}, \quad \rho_0^x = \begin{bmatrix} \frac{1}{2} & \frac{1}{2} \\ \frac{1}{2} & \frac{1}{2} \end{bmatrix}, \quad \text{and} \quad \rho_0^y = \begin{bmatrix} \frac{1}{2} & \frac{-i}{2} \\ \frac{i}{2} & \frac{1}{2} \end{bmatrix}, \quad (\text{B.10})$$

corresponding to $\mathbf{a} = (0, 0, 1)$, $\mathbf{a} = (1, 0, 0)$ and $\mathbf{a} = (0, 1, 0)$, respectively. Other initial states can always be seen as linear combinations of the above three ones.

The evolution of the system can be modelled by:

$$\rho(t) = \hat{U}(t)\rho(0)\hat{U}^\dagger(t), \quad (\text{B.11})$$

where the evolution operator $\hat{U}(t)$ is given by

$$\hat{U}(t) = \exp \left[-i \frac{\hat{H}_B t}{\hbar} \right]. \quad (\text{B.12})$$

It can then be used to calculate the density matrix at different time.

Figure B.1 indeed shows the evolution of spin-1/2 system with the three different initial states. Fig. B.1 (b), corresponding to a system polarized along x , does not exhibit any oscillation. This can be easily understood as the \mathbf{B} field is parallel to x and thus can not be lead to precession of this state. Fig. B.1(a) and (c) show that the other states precess at ω_L with a $\pi/2$ phase shift.

B.1.2 Atom-photon coupling

Let us now consider the probe laser in the two cases as shown in Fig. B.2: (a) the two lower levels are coupled to two excited ones. (b) the two lower levels are coupled to four excited ones. The optical couplings between the sublevels of the lower and upper levels of the spin-1/2 system, schematized in Fig. B.2, are also represented as matrices as we did in Chapter 4. The rows are the lower states, and the columns are the excited ones. The coupling relation matrices for Fig. B.2 (a) are then

$$\Gamma_a^{(+)} = \begin{bmatrix} 0 & -\sqrt{\frac{2}{3}} \\ 0 & 0 \end{bmatrix} \quad \text{and} \quad \Gamma_a^{(-)} = \begin{bmatrix} 0 & 0 \\ \sqrt{\frac{2}{3}} & 0 \end{bmatrix}, \quad (\text{B.13})$$

where Γ_a^+ and Γ_a^- represent the coupling by σ^+ and σ^- polarized light, respectively. The entries show the Clebsch-Gordan coefficients which indicate the coupling strength. Similarly, the coupling relation matrices for Fig. B.2 (b) are

$$\Gamma_b^{(+)} = \begin{bmatrix} 0 & 0 & \sqrt{\frac{1}{3}} & 0 \\ 0 & 0 & 0 & 1 \end{bmatrix} \quad \text{and} \quad \Gamma_b^{(-)} = \begin{bmatrix} 1 & 0 & 0 & 0 \\ 0 & \sqrt{\frac{1}{3}} & 0 & 0 \end{bmatrix}, \quad (\text{B.14})$$

where Γ_b^+ and Γ_b^- represent the coupling by σ^+ and σ^- polarized light, respectively.

B.1.3 Representation transformation

In order to determine if spin-1/2 can cause LB noise, we must investigate the optical coupling in alternative representations where the levels of the system are coupled by linearly polarized light. The optical coupling in x/y linear representations can be calculated using the following formula

$$\Gamma_{a,b}^{(x/y)} = \mathcal{M}_g^{(x/y)} \Gamma \mathcal{M}_e^{(x/y)}. \quad (\text{B.15})$$

where $\Gamma_{a,b}^{(x/y)}$ is the optical coupling matrix in the x/y linear basis. $\mathcal{M}_g^{(x/y)}$ is a 2 by 2 unitary matrix which can be seen as the linear combination principle for ground levels.

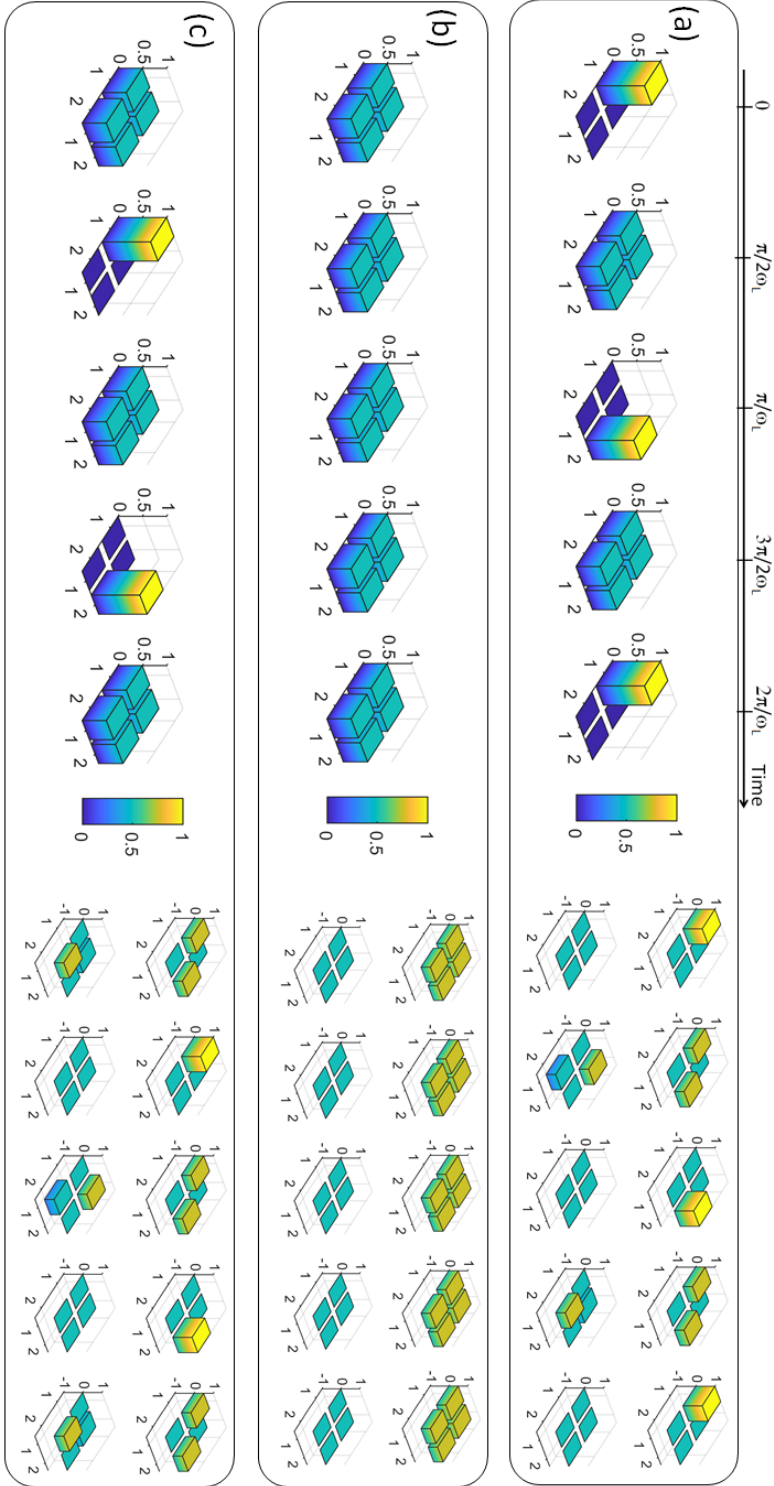


Figure B.1: Time evolution of the modulus of the density matrix ρ of a spin- $\frac{1}{2}$ in a magnetic field $\mathbf{B} = B_z \hat{x}$ for different initial states: (a) z polarized ρ_0^z , (b) x polarized ρ_0^x and (c) y polarized ρ_0^y . The right insert pictures are the real part (up) and imaginary part (down) of ρ .

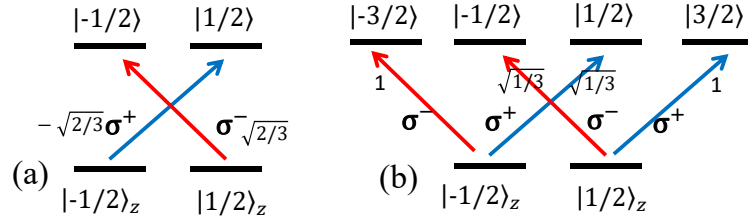


Figure B.2: Schematic of the atom-light coupling relation for two different spin 1/2 systems. The optical coupling types are shown in red (σ^-) blue (σ^+) with their corresponding Clebsch-Gordan coefficients.

The size of unitary matrix $\mathcal{M}_e^{(x/y)}$ depends on the number of the related excited states, which shows the linear combination principle of excited states.

The following matrices then give the information of the optical coupling relation in the x/y linear basis of Fig. B.2(a):

$$\Gamma_a^{(x)} = \frac{1}{\sqrt{3}} \begin{bmatrix} 1 & 0 \\ 0 & 1 \end{bmatrix} \quad \text{and} \quad \Gamma_a^{(y)} = \frac{1}{\sqrt{3}} \begin{bmatrix} 0 & 1 \\ -1 & 0 \end{bmatrix}. \quad (\text{B.16})$$

with

$$\mathcal{M}_g^{(x/y)} = \frac{1}{\sqrt{2}} \begin{bmatrix} 1 & 1 \\ i & -i \end{bmatrix}, \quad \mathcal{M}_e^{(x/y)} = \frac{1}{\sqrt{2}} \begin{bmatrix} 1 & i \\ -1 & i \end{bmatrix}. \quad (\text{B.17})$$

As each ground level couple with upper ones through both x and y polarized light in the same way, x/y LB noise cannot occur.

Similarly, we can get the optical coupling relations of the system Fig. B.2(b) in x/y linear basis

$$\Gamma_b^{(x)} = \frac{1}{\sqrt{2}} \begin{bmatrix} 1 & 1/\sqrt{3} & 0 & 0 \\ 0 & 0 & 1/\sqrt{3} & -1 \end{bmatrix} \quad (\text{B.18})$$

and

$$\Gamma_b^{(y)} = \frac{1}{\sqrt{2}} \begin{bmatrix} 0 & 0 & 1/\sqrt{3} & 1 \\ 1 & -1/\sqrt{3} & 0 & 0 \end{bmatrix} \quad (\text{B.19})$$

with

$$\mathcal{M}_g^{(x/y)} = \frac{1}{\sqrt{2}} \begin{bmatrix} 1 & 1 \\ i & -i \end{bmatrix}, \quad \mathcal{M}_e^{(x/y)} = \frac{1}{\sqrt{2}} \begin{bmatrix} 1 & 0 & 0 & i \\ 0 & 1 & i & 0 \\ 0 & 1 & -i & 0 \\ 1 & 0 & 0 & -i \end{bmatrix} \quad (\text{B.20})$$

Again, each ground level couple with upper ones through both x and y polarized light in a symmetrical manner. So that the system cannot exhibit x/y LB noise.

The same method can be used to show the absence of LB noise along u and v in such systems.

Appendix C

Hamiltonien and dipole operator

The strength of the coupling between the electromagnetic field and the atoms depends on the atomic transition. This appendix details the specific cases of the three lines of He^4 used in this thesis.

C.1 Dipole operator near D_0, D_1, D_2

The dipole operator \hat{d} in spherical basis is

$$\hat{d} = -\hat{d}^+ \boldsymbol{\sigma}^+ + \hat{d}^0 \mathbf{e}_z + \hat{d}^- \boldsymbol{\sigma}^-. \quad (\text{C.1})$$

It is a tensor operator of rank one, and we can use the Wigner-Eckart theorem [100] to get its non-vanishing elements. Near the D_0 line, we consider the angular momentum eigenstates representation $|lm\rangle$: $|1, -1\rangle$, $|1, 0\rangle$, $|1, 1\rangle$ and $|0, 0\rangle$. One has

$$\langle 0, 0 | \hat{d}^+ | 1, -1 \rangle = \langle 1, -1, 1, 1 | 0, 0 \rangle d_0 = \frac{d_0}{\sqrt{3}}, \quad (\text{C.2})$$

$$\langle 0, 0 | \hat{d}^0 | 1, 0 \rangle = \langle 1, 0, 1, 0 | 0, 0 \rangle d_0 = -\frac{d_0}{\sqrt{3}}, \quad (\text{C.3})$$

$$\langle 0, 0 | \hat{d}^- | 1, 1 \rangle = \langle 1, 1, 1, -1 | 0, 0 \rangle d_0 = \frac{d_0}{\sqrt{3}}, \quad (\text{C.4})$$

d_0 is here the value of the reduced matrix element $C_{0,1}^1$, which appears in the Wigner-Eckart theorem as quantity independent of the considered Zeeman sublevels and of the polarization of the light. This is what we call the dipole moment of the transition. For simplicity, we will consider d_0 is real and positive. The matrix of the dipole operator \hat{d} is

then

$$\hat{d} = \begin{bmatrix} 0 & 0 & 0 & -\frac{d_0}{\sqrt{3}} \\ 0 & 0 & 0 & 0 \\ 0 & 0 & 0 & 0 \\ 0 & 0 & \frac{d_0}{\sqrt{3}} & 0 \end{bmatrix} \sigma^{++} + \begin{bmatrix} 0 & 0 & 0 & 0 \\ 0 & 0 & 0 & -\frac{d_0}{\sqrt{3}} \\ 0 & 0 & 0 & 0 \\ 0 & -\frac{d_0}{\sqrt{3}} & 0 & 0 \end{bmatrix} e_{z+} + \begin{bmatrix} 0 & 0 & 0 & 0 \\ 0 & 0 & 0 & 0 \\ 0 & 0 & 0 & \frac{d_0}{\sqrt{3}} \\ -\frac{d_0}{\sqrt{3}} & 0 & 0 & 0 \end{bmatrix} \sigma^{-}. \quad (\text{C.5})$$

Similarly, close to the D_1 transition line, if d_1 is the transition dipole moment, the matrix of the dipole operator is

$$\hat{d}^1 = \begin{bmatrix} 0 & 0 & 0 & 0 & \frac{d_1}{\sqrt{2}} & 0 \\ 0 & 0 & 0 & 0 & 0 & \frac{d_1}{\sqrt{2}} \\ 0 & 0 & 0 & 0 & 0 & 0 \\ 0 & \frac{d_1}{\sqrt{2}} & 0 & 0 & 0 & 0 \\ 0 & 0 & \frac{d_1}{\sqrt{2}} & 0 & 0 & 0 \\ 0 & 0 & 0 & 0 & 0 & 0 \end{bmatrix} \sigma^{++} + \begin{bmatrix} 0 & 0 & 0 & -\frac{d_1}{\sqrt{2}} & 0 & 0 \\ 0 & 0 & 0 & 0 & 0 & 0 \\ 0 & 0 & 0 & 0 & 0 & \frac{d_1}{\sqrt{2}} \\ -\frac{d_1}{\sqrt{2}} & 0 & 0 & 0 & 0 & 0 \\ 0 & 0 & 0 & 0 & 0 & 0 \\ 0 & 0 & \frac{d_1}{\sqrt{2}} & 0 & 0 & 0 \end{bmatrix} e_{z+} + \begin{bmatrix} 0 & 0 & 0 & 0 & 0 & 0 \\ 0 & 0 & 0 & \frac{d_1}{\sqrt{2}} & 0 & 0 \\ 0 & 0 & 0 & 0 & \frac{d_1}{\sqrt{2}} & 0 \\ 0 & 0 & 0 & 0 & 0 & 0 \\ \frac{d_1}{\sqrt{2}} & 0 & 0 & 0 & 0 & 0 \\ 0 & \frac{d_1}{\sqrt{2}} & 0 & 0 & 0 & 0 \end{bmatrix} \sigma^{-}. \quad (\text{C.6})$$

In the vicinity of the D_2 transition line, if d_2 is the transition dipole moment, the matrix of

the dipole operator is

$$\hat{d}^2 = \begin{bmatrix} 0 & 0 & 0 & 0 & 0 & -\frac{d_2}{\sqrt{6}} & 0 & 0 \\ 0 & 0 & 0 & 0 & 0 & 0 & -\frac{d_2}{\sqrt{2}} & 0 \\ 0 & 0 & 0 & 0 & 0 & 0 & 0 & -d_2 \\ d_2 & 0 & 0 & 0 & 0 & 0 & 0 & 0 \\ 0 & \frac{d_2}{\sqrt{2}} & 0 & 0 & 0 & 0 & 0 & 0 \\ 0 & 0 & \frac{d_2}{\sqrt{6}} & 0 & 0 & 0 & 0 & 0 \\ 0 & 0 & 0 & 0 & 0 & 0 & 0 & 0 \\ 0 & 0 & 0 & 0 & 0 & 0 & 0 & 0 \end{bmatrix} \sigma^{++}$$

$$\begin{bmatrix} 0 & 0 & 0 & 0 & \frac{d_2}{\sqrt{2}} & 0 & 0 & 0 \\ 0 & 0 & 0 & 0 & 0 & \frac{d_2}{\sqrt{6}} & 0 & 0 \\ 0 & 0 & 0 & 0 & 0 & 0 & \frac{d_2}{\sqrt{2}} & 0 \\ 0 & 0 & 0 & 0 & 0 & 0 & 0 & 0 \\ \frac{d_2}{\sqrt{2}} & 0 & 0 & 0 & 0 & 0 & 0 & 0 \\ 0 & \frac{d_2}{\sqrt{6}} & 0 & 0 & 0 & 0 & 0 & 0 \\ 0 & 0 & \frac{d_2}{\sqrt{2}} & 0 & 0 & 0 & 0 & 0 \\ 0 & 0 & 0 & 0 & 0 & 0 & 0 & 0 \end{bmatrix} e_z +$$

$$\begin{bmatrix} 0 & 0 & 0 & d_2 & 0 & 0 & 0 & 0 \\ 0 & 0 & 0 & 0 & \frac{d_2}{\sqrt{2}} & 0 & 0 & 0 \\ 0 & 0 & 0 & 0 & 0 & \frac{d_2}{\sqrt{6}} & 0 & 0 \\ 0 & 0 & 0 & 0 & 0 & 0 & 0 & 0 \\ 0 & 0 & 0 & 0 & 0 & 0 & 0 & 0 \\ -\frac{d_2}{\sqrt{6}} & 0 & 0 & 0 & 0 & 0 & 0 & 0 \\ 0 & -\frac{d_2}{\sqrt{2}} & 0 & 0 & 0 & 0 & 0 & 0 \\ 0 & 0 & -d_2 & 0 & 0 & 0 & 0 & 0 \end{bmatrix} \sigma^{-}.$$

(C.7)

C.2 Hamiltonien of spin system.

In our experimental configuration, the hamiltonian consists of three terms:

$$H = H_0 + g\mu_B \mathbf{B} \cdot \mathbf{S} - \hat{d} \cdot \mathbf{E}. \quad (\text{C.8})$$

H_0 is the free Hamiltonien of the atomic system. The second term is the coupling of the Zeeman sublevels due to the applied magnetic field \mathbf{B} . The last term is the dipole interaction with the electromagnetic field. The classical light field can be written:

$$\mathbf{E} = (\mathcal{E}e^{-i\omega t} + \mathcal{E}^*e^{i\omega t})/2. \quad (\text{C.9})$$

We use the rotating wave approximation (RWA) and the dipole approximation which neglects the spatial variation of the electromagnetic field. The system is quantized along the propagation axis z : in this case, the light has no e_z component. If the magnetic field is applied along x , the Hamiltonien near the D_0 line and in the basis $2^3S_1 |1, -1\rangle, |1, 0\rangle, |1, 1\rangle$ and $2^3P_0 |0, 0\rangle$ is

$$H_{D_0} = \hbar \begin{pmatrix} 0 & \frac{\omega_L}{\sqrt{2}} & 0 & \frac{\Omega^-}{\sqrt{3}} \\ \frac{\omega_L}{\sqrt{2}} & 0 & \frac{\omega_L}{\sqrt{2}} & 0 \\ 0 & \frac{\omega_L}{\sqrt{2}} & 0 & -\frac{\Omega^+}{\sqrt{3}} \\ \frac{\Omega^+}{\sqrt{3}} & 0 & -\frac{\Omega^-}{\sqrt{3}} & \Delta_0 \end{pmatrix} \quad (\text{C.10})$$

with $d_0\mathcal{E}/2\hbar = \Omega^+\sigma^+ + \Omega^-\sigma^-$. The Hamiltonien near the D_1 line and in the basis $2^3S_1 |1, -1\rangle, |1, 0\rangle, |1, 1\rangle$ and $2^3P_1 |1, -1\rangle, |1, 0\rangle, |1, 1\rangle$ is

$$H_{D_1} = \hbar \begin{pmatrix} 0 & \frac{\omega_L}{\sqrt{2}} & 0 & 0 & -\frac{\Omega^-}{\sqrt{2}} & 0 \\ \frac{\omega_L}{\sqrt{2}} & 0 & \frac{\omega_L}{\sqrt{2}} & -\frac{\Omega^+}{\sqrt{2}} & 0 & -\frac{\Omega^-}{\sqrt{2}} \\ 0 & \frac{\omega_L}{\sqrt{2}} & 0 & 0 & \frac{\Omega^+}{\sqrt{2}} & 0 \\ 0 & -\frac{\Omega^-}{\sqrt{2}} & 0 & \Delta_1 & \frac{\omega_L}{\sqrt{2}} & 0 \\ -\frac{\Omega^+}{\sqrt{2}} & 0 & -\frac{\Omega^-}{\sqrt{2}} & \frac{\omega_L}{\sqrt{2}} & \Delta_1 & \frac{\omega_L}{\sqrt{2}} \\ 0 & -\frac{\Omega^+}{\sqrt{2}} & 0 & 0 & \frac{\omega_L}{\sqrt{2}} & \Delta_1 \end{pmatrix}. \quad (\text{C.11})$$

The Hamiltonien near the D_2 line and in the basis $2^3S_1 |1, -1\rangle, |1, 0\rangle, |1, 1\rangle$ and

$2^3 P_2 |2, -2\rangle, |2, -1\rangle, |2, 0\rangle, |2, 1\rangle, |2, 2\rangle$ is

$$H_{D_2} = \hbar \begin{pmatrix} 0 & \frac{\omega_L}{\sqrt{2}} & 0 & -\Omega^+ & 0 & +\frac{\Omega^-}{\sqrt{6}} & 0 & 0 \\ \frac{\omega_L}{\sqrt{2}} & 0 & \frac{\omega_L}{\sqrt{2}} & 0 & -\frac{\Omega^+}{\sqrt{2}} & 0 & +\frac{\Omega^-}{\sqrt{2}} & 0 \\ 0 & \frac{\omega_L}{\sqrt{2}} & 0 & 0 & 0 & -\frac{\Omega^+}{\sqrt{6}} & 0 & +\Omega^- \\ -\Omega^- & 0 & 0 & \Delta_2 & \omega_L & 0 & 0 & 0 \\ 0 & -\frac{\Omega^-}{\sqrt{2}} & 0 & \omega_L & \Delta_2 & \sqrt{\frac{3}{2}}\omega_L & 0 & 0 \\ +\frac{\Omega^+}{\sqrt{6}} & 0 & -\frac{\Omega^-}{\sqrt{6}} & 0 & \sqrt{\frac{3}{2}}\omega_L & \Delta_2 & \sqrt{\frac{3}{2}}\omega_L & 0 \\ 0 & +\frac{\Omega^+}{\sqrt{2}} & 0 & 0 & 0 & \sqrt{\frac{3}{2}}\omega_L & \Delta_2 & \omega_L \\ 0 & 0 & +\Omega^+ & 0 & 0 & 0 & \omega_L & \Delta_2 \end{pmatrix}. \quad (\text{C.12})$$

C.3 Polarization of the system

The light propagation function under the slow varying envelope approximation is

$$\frac{\partial \mathcal{E}}{\partial z} + \frac{1}{c} \frac{\partial \mathcal{E}}{\partial t} = i \frac{\omega}{2\epsilon_0 c} \mathcal{P}, \quad (\text{C.13})$$

where \mathcal{P} is the slow varying part of the polarization of the atomic ensemble with n_{at} atoms. One has

$$\vec{P} = (\mathcal{P}e^{-i\omega t} + \mathcal{P}^*e^{i\omega t})/2, \quad (\text{C.14})$$

$$\vec{P} = n_{at} \langle \hat{d} \rangle = n_{at} \text{Tr}[\rho \hat{d}], \quad (\text{C.15})$$

where $\text{Tr}(\rho \hat{d})$ is an average dipole moment over all the atoms. By the expression of the dipole operator Eq. (C.5) to Eq. (C.7), the expectation value of \hat{d} for the three transitions D_0, D_1 and D_2 are respectively:

$$\langle \hat{d} \rangle_0 = \frac{d_0}{\sqrt{3}} (-\rho_{14} \sigma^- + \rho_{34} \sigma^+ - \rho_{24} \mathbf{e}_z) + c.c., \quad (\text{C.16})$$

$$\langle \hat{d} \rangle_1 = \frac{d_1}{\sqrt{2}} [(\rho_{15} + \rho_{26}) \sigma^- + (\rho_{24} + \rho_{35}) \sigma^+ + (-\rho_{14} + \rho_{36}) \mathbf{e}_z] + c.c., \quad (\text{C.17})$$

$$\langle \hat{d} \rangle_2 = d_2 [(\rho_{14} + \frac{\rho_{25}}{\sqrt{2}} + \frac{\rho_{36}}{\sqrt{6}}) \sigma^+ + (-\frac{\rho_{16}}{\sqrt{6}} - \frac{\rho_{27}}{\sqrt{2}} - \rho_{38}) \sigma^- + (\rho_{15} + \frac{\rho_{26}}{\sqrt{6}} + \frac{\rho_{37}}{\sqrt{2}}) \mathbf{e}_z] + c.c., \quad (\text{C.18})$$

where ρ_{ij} is the element of the density matrix, which is in the row i and the column j .

As the Hamiltonien is given in the rotating basis, the density matrix is calculated in the same basis, writing:

$$\begin{cases} \tilde{\rho}_{ij} = \rho_{ij}e^{-i\omega t} \\ \tilde{\rho}_{ji} = \rho_{ji}e^{i\omega t} \end{cases} \quad \text{for } j > i. \quad (\text{C.19})$$

Combining Eqs. (C.14, C.16 ~ C.18), we can then get the slow varying envelope of the polarization \mathcal{P} around the D_0 , D_1 and D_2 lines:

$$\mathcal{P} = n_{at} \frac{d_0}{\sqrt{3}} (\rho_{43} \sigma^- - \rho_{41} \sigma^+), \quad (\text{C.20})$$

$$\mathcal{P}^1 = n_{at} \frac{d_1}{\sqrt{2}} [(\rho_{42} + \rho_{53}) \sigma^- + (\rho_{51} + \rho_{62}) \sigma^+], \quad (\text{C.21})$$

$$\mathcal{P}^2 = n_{at} d_2 [(\rho_{41} + \frac{\rho_{52}}{\sqrt{2}} + \frac{\rho_{63}}{\sqrt{6}}) \sigma^- + (-\frac{\rho_{61}}{\sqrt{6}} - \frac{\rho_{72}}{\sqrt{2}} - \rho_{83}) \sigma^+]. \quad (\text{C.22})$$

Appendix D

Operators in different basis

We consider here the three lower states of the metastable level of helium 2^3S_1 : $\{|-1\rangle_z, |0\rangle_z, |+1\rangle_z\}$. z is the propagation direction of the laser beam. As the \mathbf{B} field defines a specific x direction, a better analysis of our experimental results lead us to check with two other basis: $\{|\Psi_x\rangle, |0\rangle_z, |\Psi_y\rangle\}$ and $\{|\Psi_u\rangle, |0\rangle_z, |\Psi_v\rangle\}$ where

$$|\Psi_x\rangle = \frac{1}{\sqrt{2}}(|-1\rangle_z + |1\rangle_z), \quad (\text{D.1})$$

$$|\Psi_y\rangle = -\frac{i}{\sqrt{2}}(|-1\rangle_z - |1\rangle_z). \quad (\text{D.2})$$

$$|\Psi_u\rangle = \frac{1}{\sqrt{2}}(e^{i\pi/4} |-1\rangle_z + e^{-i\pi/4} |+1\rangle_z), \quad (\text{D.3})$$

$$|\Psi_v\rangle = \frac{1}{\sqrt{2}}(e^{-i\pi/4} |-1\rangle_z + e^{i\pi/4} |+1\rangle_z). \quad (\text{D.4})$$

$\{|\Psi_x\rangle$ and $|\Psi_y\rangle\}$ are coupled to the excited states by linear polarizations along x and y respectively, while $\{|\Psi_u\rangle$ and $|\Psi_v\rangle\}$ are coupled to the upper levels by the linear polarizations rotated by 45° , labelled u and v .

Any operator \hat{M} in the $\{|-1\rangle_z, |0\rangle_z, |+1\rangle_z\}$ basis can be obtained in the $\{|\Psi_x\rangle, |0\rangle_z, |\Psi_y\rangle\}$ basis by:

$$\hat{M}' = S\hat{M}S^\dagger, \quad (\text{D.5})$$

with

$$S = \frac{1}{\sqrt{2}} \begin{pmatrix} 1 & 0 & 1 \\ 0 & \sqrt{2} & 0 \\ i & 0 & -i \end{pmatrix}. \quad (\text{D.6})$$

The matrix S can be obtained from the Eqs. [D.1](#) and [D.2](#).

For a change to the $\{|\Psi_u\rangle, |0\rangle_z, |\Psi_v\rangle\}$ basis, using the Eqs. D.3 and D.4, we can similarly find a change by basis matrix U :

$$\hat{M}'' = U\hat{M}U^\dagger. \quad (\text{D.7})$$

with

$$U = \frac{1}{2} \begin{pmatrix} 1-i & 0 & 1+i \\ 0 & 2 & 0 \\ 1+i & 0 & 1-i \end{pmatrix}. \quad (\text{D.8})$$

Let us look at the spin mechanisms defined in the chapter 4. Three of the eight spin mechanisms \hat{M}_4, \hat{M}_7 and \hat{M}_8 are rewritten in x/y linear basis and two of them are rewritten in u/v linear basis. These spin mechanisms changes and corresponding matrices are given below:

$\hat{M}_4, \hat{M}_7, \hat{M}_8$ in x/y linear basis

$$\hat{M}_4 = \begin{bmatrix} 0 & 0 & 1 \\ 0 & 0 & 0 \\ 1 & 0 & 0 \end{bmatrix} \xrightarrow{S\hat{M}_4S^\dagger} \begin{bmatrix} 1 & 0 & 0 \\ 0 & 0 & 0 \\ 0 & 0 & -1 \end{bmatrix}, \quad (\text{D.9})$$

$$\hat{M}_7 = \frac{1}{\sqrt{2}} \begin{bmatrix} 0 & -i & 0 \\ i & 0 & i \\ 0 & -i & 0 \end{bmatrix} \xrightarrow{S\hat{M}_7S^\dagger} \frac{1}{\sqrt{2}} \begin{bmatrix} 0 & -i & 0 \\ i & 0 & 0 \\ 0 & 0 & 0 \end{bmatrix}, \quad (\text{D.10})$$

$$\hat{M}_8 = \frac{1}{\sqrt{3}} \begin{bmatrix} 1 & 0 & 1 \\ 0 & -2 & 0 \\ 1 & 0 & 1 \end{bmatrix} \xrightarrow{S\hat{M}_8S^\dagger} \frac{1}{\sqrt{2}} \begin{bmatrix} 1 & 0 & 0 \\ 0 & -2 & 0 \\ 0 & 0 & 1 \end{bmatrix}. \quad (\text{D.11})$$

\hat{M}_5, \hat{M}_6 in uv linear basis

$$\hat{M}_5 = \begin{bmatrix} 0 & 0 & -i \\ 0 & 0 & 0 \\ i & 0 & 0 \end{bmatrix} \xrightarrow{U\hat{M}_5U^\dagger} \begin{bmatrix} -1 & 0 & 0 \\ 0 & 0 & 0 \\ 0 & 0 & 1 \end{bmatrix}, \quad (\text{D.12})$$

$$\hat{M}_6 = \frac{1}{\sqrt{2}} \begin{bmatrix} 0 & 1 & 0 \\ 1 & 0 & -1 \\ 0 & -1 & 0 \end{bmatrix} \xrightarrow{U\hat{M}_6U^\dagger} \frac{1}{\sqrt{2}} \begin{bmatrix} 0 & -i & 0 \\ i & 0 & -i \\ 0 & i & 0 \end{bmatrix}. \quad (\text{D.13})$$

Bibliography

- [1] E. B. Aleksandrov and V. S. Zapasskii. Magnetic resonance in the faraday-rotation noise spectrum. *JETP*, 54:64, 1981.
- [2] SA Crooker, DG Rickel, AV Balatsky, and DL Smith. Spectroscopy of spontaneous spin noise as a probe of spin dynamics and magnetic resonance. *Nature*, 431(7004):49–52, 2004.
- [3] M Römer, J Hübner, and M Oestreich. Spin noise spectroscopy in semiconductors. *Review of Scientific Instruments*, 78(10):103903, 2007.
- [4] Michael Oestreich, M Römer, Rolf J Haug, and D Hägele. Spin noise spectroscopy in gaas. *Physical review letters*, 95(21):216603, 2005.
- [5] Georg M Müller, Michael Oestreich, Michael Römer, and Jens Hübner. Semiconductor spin noise spectroscopy: Fundamentals, accomplishments, and challenges. *Physica E: Low-dimensional Systems and Nanostructures*, 43(2):569–587, 2010.
- [6] SA Crooker, J Brandt, C Sandfort, A Greilich, DR Yakovlev, D Reuter, AD Wieck, and M Bayer. Spin noise of electrons and holes in self-assembled quantum dots. *Physical review letters*, 104(3):036601, 2010.
- [7] GM Bruun, Brian M Andersen, Eugene Demler, and Anders S Sørensen. Probing spatial spin correlations of ultracold gases by quantum noise spectroscopy. *Physical review letters*, 102(3):030401, 2009.
- [8] Bogdan Mihaila, Scott A Crooker, Krastan B Blagoev, Dwight G Rickel, Peter B Littlewood, and Darryl L Smith. Spin noise spectroscopy to probe quantum states of ultracold fermionic atom gases. *Physical Review A*, 74(6):063608, 2006.
- [9] Valerii S. Zapasskii. Spin-noise spectroscopy: from proof of principle to applications. *Adv. Opt. Photon.*, 5(2):131–168, Jun 2013.
- [10] Dibyendu Roy, Luyi Yang, Scott A Crooker, and Nikolai A Sinitsyn. Cross-correlation spin noise spectroscopy of heterogeneous interacting spin systems. *Scientific Reports*, 5(1):1–7, 2015.

- [11] Shikang Liu, Pascal Neveu, Joseph Delpy, Luka Hemmen, Etienne Brion, E Wu, Fabien Bretenaker, and Fabienne Goldfarb. Birefringence and dichroism effects in the spin noise spectra of a spin-1 system. *New Journal of Physics*, 24:113047, 2022.
- [12] S Liu, P Neveu, J Delpy, E Wu, F Bretenaker, and F Goldfarb. Spin-noise spectroscopy of a spin-one system. *Physical Review A*, 107(2):023527, 2023.
- [13] Joseph Delpy, Shikang Liu, Pascal Neveu, E Wu, Fabien Bretenaker, and Fabienne Goldfarb. Spin-noise spectroscopy of optical light shifts. *Physical Review A*, 107(1):L011701, 2023.
- [14] John Bertrand Johnson. Thermal agitation of electricity in conductors. *Physical review*, 32(1):97, 1928.
- [15] Harry Nyquist. Thermal agitation of electric charge in conductors. *Physical review*, 32(1):110, 1928.
- [16] Rep Kubo. The fluctuation-dissipation theorem. *Reports on progress in physics*, 29(1):255, 1966.
- [17] DR White, R Galleano, A Actis, H Brixy, M De Groot, J Dubbeldam, AL Reesink, F Edler, H Sakurai, RL Shepard, et al. The status of johnson noise thermometry. *Metrologia*, 33(4):325, 1996.
- [18] R Brown and Richard Q Twiss. Correlation between photons in two coherent beams of light. *Nature*, 177(4497):27–29, 1956.
- [19] Ryuta Yamamoto, Jun Kobayashi, Kohei Kato, Takuma Kuno, Yuto Sakura, and Yoshiro Takahashi. Site-resolved imaging of single atoms with a faraday quantum gas microscope. *Physical Review A*, 96(3):033610, 2017.
- [20] Miroslav Gajdacz, Poul L Pedersen, Troels Mørch, Andrew J Hilliard, Jan Arlt, and Jacob F Sherson. Non-destructive faraday imaging of dynamically controlled ultracold atoms. *Review of Scientific Instruments*, 84(8):083105, 2013.
- [21] Mick A Kristensen, Miroslav Gajdacz, Poul L Pedersen, Carsten Klempt, Jacob F Sherson, Jan J Arlt, and Andrew J Hilliard. Sub-atom shot noise faraday imaging of ultracold atom clouds. *Journal of Physics B: Atomic, Molecular and Optical Physics*, 50(3):034004, 2017.
- [22] Jakob Meineke, Jean-Philippe Brantut, David Stadler, Torben Müller, Henning Moritz, and Tilman Esslinger. Interferometric measurement of local spin fluctuations in a quantum gas. *Nature Physics*, 8(6):454–458, 2012.
- [23] Dayou Yang, Catherine Laflamme, DV Vasilyev, MA Baranov, and Peter Zoller. Theory of a quantum scanning microscope for cold atoms. *Physical Review Letters*, 120(13):133601, 2018.

- [24] Alessio Recati and Sandro Stringari. Spin fluctuations, susceptibility, and the dipole oscillation of a nearly ferromagnetic fermi gas. *Physical Review Letters*, 106(8):080402, 2011.
- [25] Ehud Altman, Eugene Demler, and Mikhail D Lukin. Probing many-body states of ultracold atoms via noise correlations. *Physical Review A*, 70(1):013603, 2004.
- [26] Paul Niklas Jepsen, Jesse Amato-Grill, Ivana Dimitrova, Wen Wei Ho, Eugene Demler, and Wolfgang Ketterle. Spin transport in a tunable heisenberg model realized with ultracold atoms. *Nature*, 588(7838):403–407, 2020.
- [27] Katja Gosar, Tina Arh, Tadej Mežnaršič, Ivan Kvasič, Dušan Ponikvar, Tomaž Apih, Rainer Kaltenbaek, Erik Zupanič, Samo Beguš, Peter Jeglič, et al. Single-shot sterngerlach magnetic gradiometer with an expanding cloud of cold cesium atoms. *Physical Review A*, 103(2):022611, 2021.
- [28] Maheswar Swar, Dibyendu Roy, D Dhanalakshmi, Saptarishi Chaudhuri, Sanjukta Roy, and Hema Ramachandran. Measurements of spin properties of atomic systems in and out of equilibrium via noise spectroscopy. *Opt. Express*, 26(24):32168–32183, Nov 2018.
- [29] Yuval Cohen, Krishna Jadeja, Sindi Sula, Michela Venturelli, Cameron Deans, Luca Marmugi, and Ferruccio Renzoni. A cold atom radio-frequency magnetometer. *Applied Physics Letters*, 114(7):073505, 2019.
- [30] Vito Giovanni Lucivero, Ricardo Jiménez-Martínez, Jia Kong, and Morgan W. Mitchell. Squeezed-light spin noise spectroscopy. *Phys. Rev. A*, 93:053802, May 2016.
- [31] Pavel Sterin, Julia Wiegand, Jens Hübner, and Michael Oestreich. Optical amplification of spin noise spectroscopy via homodyne detection. *Phys. Rev. Applied*, 9:034003, Mar 2018.
- [32] M. Yu. Petrov, A. N. Kamenskii, V. S. Zapasskii, M. Bayer, and A. Grelich. Increased sensitivity of spin noise spectroscopy using homodyne detection in n -doped gaas. *Phys. Rev. B*, 97:125202, Mar 2018.
- [33] Nikolai A Sinitsyn and Yuriy V Pershin. The theory of spin noise spectroscopy: a review. *Reports on Progress in Physics*, 79(10):106501, 2016.
- [34] EB Aleksandrov and VS Zapasskii. Magnetic resonance in the faraday-rotation noise spectrum. *Zh. Eksp. Teor. Fiz*, 81:132–138, 1981.
- [35] S. A. Crooker, D. G. Rickel, A. V. Balatsky, and D. L. Smith. Spectroscopy of spontaneous spin noise as a probe of spin dynamics and magnetic resonance. *Nature*, 431:49–52, 2004.

- [36] V Shah, G Vasilakis, and MV Romalis. High bandwidth atomic magnetometry with continuous quantum nondemolition measurements. *Physical review letters*, 104(1):013601, 2010.
- [37] A Kuzmich, L Mandel, J Janis, YE Young, R Egnisman, and NP Bigelow. Quantum nondemolition measurements of collective atomic spin. *Physical Review A*, 60(3):2346, 1999.
- [38] GE Katsoprinakis, AT Dellis, and IK Kominis. Measurement of transverse spin-relaxation rates in a rubidium vapor by use of spin-noise spectroscopy. *Physical Review A*, 75(4):042502, 2007.
- [39] DS Smirnov, B Reznichenko, A Auffèves, and L Lanco. Measurement back action and spin noise spectroscopy in a charged cavity qed device in the strong coupling regime. *Physical Review B*, 96(16):165308, 2017.
- [40] Steeve Cronenberger, Denis Scalbert, David Ferrand, Hervé Boukari, and Joël Cibert. Atomic-like spin noise in solid-state demonstrated with manganese in cadmium telluride. *Nature communications*, 6(1):1–6, 2015.
- [41] Maheswar Swar, Dibyendu Roy, Subhajit Bhar, Sanjukta Roy, and Saptarishi Chaudhuri. Detection of spin coherence in cold atoms via faraday rotation fluctuations. *Physical Review Research*, 3(4):043171, 2021.
- [42] A. A. Fomin, M. Yu. Petrov, G. G. Kozlov, M. M. Glazov, I. I. Ryzhov, M. V. Balabas, and V. S. Zapasskii. Spin-alignment noise in atomic vapor. *Phys. Rev. Research*, 2:012008, Jan 2020.
- [43] VO Kozlov, NS Kuznetsov, DS Smirnov, II Ryzhov, GG Kozlov, and VS Zapasskii. Spin noise in birefringent media. *Physical Review Letters*, 129(7):077401, 2022.
- [44] Takahisa Mitsui. Spontaneous noise spectroscopy of an atomic magnetic resonance. *Physical review letters*, 84(23):5292, 2000.
- [45] Valerii S Zapasskii, Alex Greilich, Scott A Crooker, Yan Li, Gleb G Kozlov, Dmitri R Yakovlev, Dirk Reuter, Andreas D Wieck, and Manfred Bayer. Optical spectroscopy of spin noise. *Physical Review Letters*, 110(17):176601, 2013.
- [46] Luyi Yang, P Glasenapp, A Greilich, D Reuter, AD Wieck, DR Yakovlev, M Bayer, and SA Crooker. Two-colour spin noise spectroscopy and fluctuation correlations reveal homogeneous linewidths within quantum-dot ensembles. *Nature Communications*, 5(1):1–7, 2014.
- [47] William Esco Moerner and Gary C Bjorklund. *Persistent spectral hole-burning: science and applications*, volume 1. Springer, 1988.
- [48] JMHJ Erland, K-H Pantke, V Mizeikis, VG Lyssenko, and Jørn Märcher Hvam. Spectrally resolved four-wave mixing in semiconductors: influence of inhomogeneous broadening. *Physical Review B*, 50(20):15047, 1994.

- [49] Torsten Meier, Peter Thomas, and Stephan W Koch. *Coherent semiconductor optics: from basic concepts to nanostructure applications*. Springer Science & Business Media, 2007.
- [50] M Römer, J Hübner, and M Oestreich. Spatially resolved doping concentration measurement in semiconductors via spin noise spectroscopy. *Applied Physics Letters*, 94(11):112105, 2009.
- [51] Mansoor Sheik-Bahae, Ali A Said, and Eric W Van Stryland. High-sensitivity, single-beam n^2 measurements. *Optics letters*, 14(17):955–957, 1989.
- [52] Mansoor Sheik-Bahae, Ali A Said, T-H Wei, David J Hagan, and Eric W Van Stryland. Sensitive measurement of optical nonlinearities using a single beam. *IEEE journal of quantum electronics*, 26(4):760–769, 1990.
- [53] MM Glazov and EL Ivchenko. Spin noise in quantum dot ensembles. *Physical Review B*, 86(11):115308, 2012.
- [54] MM Glazov and VS Zapasskii. Linear optics, raman scattering, and spin noise spectroscopy. *Optics Express*, 23(9):11713–11723, 2015.
- [55] Yuriy V Pershin, Valeriy A Slipko, Dibyendu Roy, and Nikolai A Sinitsyn. Two-beam spin noise spectroscopy. *Applied Physics Letters*, 102(20):202405, 2013.
- [56] Steeve Cronenberger, Chahine Abbas, Denis Scalbert, and H Boukari. Spatiotemporal spin noise spectroscopy. *Physical review letters*, 123(1):017401, 2019.
- [57] Fuxiang Li, Yuriy V Pershin, Valeriy A Slipko, and Nikolai A Sinitsyn. Nonequilibrium spin noise spectroscopy. *Physical Review Letters*, 111(6):067201, 2013.
- [58] Pablo Schad, Boris N Narozhny, Gerd Schön, and Alexander Shnirman. Nonequilibrium spin noise and noise of susceptibility. *Physical Review B*, 90(20):205419, 2014.
- [59] Maheswar Swar, Dibyendu Roy, D Dhanalakshmi, Saptarishi Chaudhuri, Sanjukta Roy, and Hema Ramachandran. Measurements of spin properties of atomic systems in and out of equilibrium via noise spectroscopy. *Optics Express*, 26(24):32168–32183, 2018.
- [60] DS Smirnov, Ph Glasenapp, M Bergen, MM Glazov, D Reuter, AD Wieck, M Bayer, and A Greilich. Nonequilibrium spin noise in a quantum dot ensemble. *Physical Review B*, 95(24):241408, 2017.
- [61] Julia Wiegand, Dmitry S Smirnov, Jens Hübner, Mikhail M Glazov, and Michael Oestreich. Spin and reoccupation noise in a single quantum dot beyond the fluctuation-dissipation theorem. *Physical Review B*, 97(8):081403, 2018.
- [62] Fuxiang Li, Avadh Saxena, Darryl Smith, and Nikolai A Sinitsyn. Higher-order spin noise statistics. *New Journal of Physics*, 15(11):113038, 2013.

- [63] Christian Flindt, Christian Fricke, Frank Hohls, Tomáš Novotný, Karel Netočný, Tobias Brandes, and Rolf J Haug. Universal oscillations in counting statistics. *Proceedings of the National Academy of Sciences*, 106(25):10116–10119, 2009.
- [64] Shuji Nakamura, Yoshiaki Yamauchi, Masayuki Hashisaka, Kensaku Chida, Kensuke Kobayashi, Teruo Ono, Renaud Leturcq, Klaus Ensslin, Keiji Saito, Yasuhiro Utsumi, et al. Nonequilibrium fluctuation relations in a quantum coherent conductor. *Physical review letters*, 104(8):080602, 2010.
- [65] Yasuhiro Utsumi, DS Golubev, Michael Marthaler, Keiji Saito, Toshimasa Fujisawa, and Gerd Schön. Bidirectional single-electron counting and the fluctuation theorem. *Physical Review B*, 81(12):125331, 2010.
- [66] Fuxiang Li, SA Crooker, and NA Sinitsyn. Higher-order spin-noise spectroscopy of atomic spins in fluctuating external fields. *Physical Review A*, 93(3):033814, 2016.
- [67] Sebastian Starosielec, Rachel Fainblat, Jörg Rudolph, and Daniel Hägele. Two-dimensional higher order noise spectroscopy up to radio frequencies. *Review of Scientific Instruments*, 81(12):125101, 2010.
- [68] A Bechtold, F Li, K Müller, Tobias Simmet, P-L Ardel, Jonathan J Finley, and Nikolai A Sinitsyn. Quantum effects in higher-order correlators of a quantum-dot spin qubit. *Physical Review Letters*, 117(2):027402, 2016.
- [69] Dmitriy S Smirnov, Vladimir Nikolaevich Mantsevich, and Mikhail Mikhailovich Glazov. Theory of optically detected spin noise in nanosystems. *Physics-Uspekhi*, 64(9):923, 2021.
- [70] Carlos P Espigares, Pedro L Garrido, and Pablo I Hurtado. Dynamical phase transition for current statistics in a simple driven diffusive system. *Physical Review E*, 87(3):032115, 2013.
- [71] James M Hickey, Christian Flindt, and Juan P Garrahan. Trajectory phase transitions and dynamical lee-yang zeros of the glauber-ising chain. *Physical Review E*, 88(1):012119, 2013.
- [72] Ryogo Kubo. Generalized cumulant expansion method. *Journal of the Physical Society of Japan*, 17(7):1100–1120, 1962.
- [73] Jerry M Mendel. Tutorial on higher-order statistics (spectra) in signal processing and system theory: Theoretical results and some applications. *Proceedings of the IEEE*, 79(3):278–305, 1991.
- [74] Ramin Dahbashi, Jens Hübner, Fabian Berski, Klaus Pierz, and Michael Oestreich. Optical spin noise of a single hole spin localized in an (inga) as quantum dot. *Physical review letters*, 112(15):156601, 2014.

- [75] MM Sharipova, AN Kamenskii, II Ryzhov, M Yu Petrov, GG Kozlov, A Greilich, M Bayer, and VS Zapasskii. Stimulated spin noise in an activated crystal. *Journal of Applied Physics*, 126(14):143901, 2019.
- [76] F. Goldfarb, J. Ghosh, M. David, J. Ruggiero, T. Chanelière, J.-L. Le Gouët, H. Gilles, R. Ghosh, and F. Bretenaker. Observation of ultra-narrow electromagnetically induced transparency and slow light using purely electronic spins in a hot atomic vapor. *Europhys. Lett.*, 82(5):54002, 2008.
- [77] SS Hodgman, RG Dall, LJ Byron, KGH Baldwin, SJ Buckman, and AG Truscott. Metastable helium: A new determination of the longest atomic excited-state lifetime. *Physical review letters*, 103(5):053002, 2009.
- [78] Nikolai A Sinitsyn and Yuriy V Pershin. The theory of spin noise spectroscopy: a review. *Reports on Progress in Physics*, 79(10):106501, sep 2016.
- [79] Takahisa Mitsui. Spontaneous noise spectroscopy of an atomic magnetic resonance. *Physical review letters*, 84(23):5292, 2000.
- [80] M. Yu. Petrov, I. I. Ryzhov, D. S. Smirnov, L. Yu. Belyaev, R. A. Potekhin, M. M. Glazov, V. N. Kulyasov, G. G. Kozlov, E. B. Aleksandrov, and V. S. Zapasskii. Homogenization of doppler broadening in spin noise spectroscopy. *Phys. Rev. A*, 97:032502, Mar 2018.
- [81] E Figueroa, F Vewinger, J Appel, and A I Lvovsky. Decoherence of electromagnetically induced transparency in atomic vapor. *Optics letters*, 31(17):2625–2627, 2006.
- [82] Chitram Banerjee. *Experimental and Theoretical Study of Two Non-linear Processes Induced by Ultra-narrow Resonances in Atoms*. PhD thesis, Université Paris-Saclay (ComUE), 2019.
- [83] Dieter Suter and Thomas Marty. Experimental observation of the rotation properties of atomic multipoles. *JOSA B*, 11(1):242–252, 1994.
- [84] HJ Carmichael. An open system approach to quantum optics, vol. m 18 of lecture notes in physics, 1993.
- [85] Eougenious L Ivchenko. *Optical spectroscopy of semiconductor nanostructures*. Alpha Science Int'l Ltd., 2005.
- [86] GG Kozlov, AA Fomin, M Yu Petrov, II Ryzhov, and VS Zapasskii. Raman scattering model of the spin noise. *Optics Express*, 29(4):4770–4782, 2021.
- [87] A. R. Shlyakhov, V. V. Zemlyanov, M. V. Suslov, A. V. Lebedev, G. S. Paraoanu, G. B. Lesovik, and G. Blatter. Quantum metrology with a transmon qutrit. *Phys. Rev. A*, 97:022115, Feb 2018.

- [88] VA Soltamov, C Kasper, AV Poshakinskiy, AN Anisimov, EN Mokhov, A Sperlich, SA Tarasenko, PG Baranov, GV Astakhov, and V Dyakonov. Excitation and coherent control of spin qubit modes in silicon carbide at room temperature. *Nature communications*, 10(1):1–8, 2019.
- [89] Giorgio Colangelo, Robert J Sewell, Naeimeh Behbood, Ferran Martin Ciurana, Gil Triginer, and Morgan W Mitchell. Quantum atom–light interfaces in the gaussian description for spin-1 systems. *New Journal of Physics*, 15(10):103007, 2013.
- [90] Bogdan Mihaila, Scott A Crooker, Dwight G Rickel, Krastan B Blagoev, Peter B Littlewood, and Darryl L Smith. Quantitative study of spin noise spectroscopy in a classical gas of k 41 atoms. *Physical Review A*, 74(4):043819, 2006.
- [91] A. Kuzmich, L. Mandel, J. Janis, Y. E. Young, R. Egnisman, and N. P. Bigelow. Quantum nondemolition measurements of collective atomic spin. *Phys. Rev. A*, 60:2346–2350, Sep 1999.
- [92] T. Fernholz, H. Krauter, K. Jensen, J. F. Sherson, A. S. Sørensen, and E. S. Polzik. Spin squeezing of atomic ensembles via nuclear-electronic spin entanglement. *Phys. Rev. Lett.*, 101:073601, Aug 2008.
- [93] Gary Carter, Charles Knapp, and Albert Nuttall. Estimation of the magnitude-squared coherence function via overlapped fast fourier transform processing. *IEEE transactions on audio and electroacoustics*, 21(4):337–344, 1973.
- [94] Michael Brandstein and Darren Ward. *Microphone arrays: signal processing techniques and applications*. Springer Science & Business Media, 2001.
- [95] Radoslav Bortel and Pavel Sovka. Approximation of statistical distribution of magnitude squared coherence estimated with segment overlapping. *Signal Processing*, 87(5):1100–1117, 2007.
- [96] Wang-Kong Tse, A Saxena, DL Smith, and NA Sinitsyn. Spin and valley noise in two-dimensional dirac materials. *Physical Review Letters*, 113(4):046602, 2014.
- [97] Luyi Yang, Nikolai A Sinitsyn, Weibing Chen, Jiangtan Yuan, Jing Zhang, Jun Lou, and Scott A Crooker. Long-lived nanosecond spin relaxation and spin coherence of electrons in monolayer mos₂ and ws₂. *Nature Physics*, 11(10):830–834, 2015.
- [98] Cornelis Jacobus Gorter. *Paramagnetic relaxation*, volume 15. Elsevier Amsterdam, 1947.
- [99] T. Lauprêtre, S. Kumar, P. Berger, R. Faoro, R. Ghosh, F. Bretenaker, and F. Goldfarb. Ultranarrow resonance due to coherent population oscillations in a Λ -type atomic system. *Phys. Rev. A*, 85:051805(R), May 2012.
- [100] Jun John Sakurai and Eugene D Commins. *Modern quantum mechanics*, revised edition, 1995.

Acknowledgment

This work was completed under the agreement on joint international supervision between Université-Paris-Saclay in France and East China Normal University (ECNU) in China. I wish to express my deep appreciation to all individuals involved on both sides who provided me with this opportunity. Thank you for your support throughout this journey.

I would like to express my deepest gratitude and appreciation to my supervisors Dr. Fabien Bretenaker, Dr. Fabienne Goldfarb (Laboratoire LuMIn, Orsay), and Dr. E Wu (State Key Laboratory of Precision Spectroscopy, Shanghai) for their continued guidance and invaluable support throughout these years. Thanks to them, I had the opportunity to learn from many brilliant and friendly individuals within the two exceptional groups. The invaluable experience has been instrumental in my personal and academic growth.

In 2017, I had the chance to be accepted as a master student in E's group. I followed Dr. Botao Wu to make some fluorescent materials and try to enhance the fluorescence with an infrared laser. I can still feel the excitement when I observe the fluorescence and nanostructure of these materials. I want to thank Dr. Botao W, Chengda Pan, and Qiang Ma who ever taught me standard experimental operation.

In 2019, I had the opportunity to go to France and work in Fabien's group at LuMIn on the topic of the coherent process of metastable helium. I am especially grateful to Yifan SUN, who helped me settle in and become acquainted with the French lifestyle. I would also like to acknowledge Pascal Neveu, who taught me all the experiment's intricacies, and the fundamentals of quantum optics, and gave me some initial training at the start of my Ph.D.

It feels like just yesterday when I was discussing spin noise spectroscopy with Fabienne, Fabien, and Joseph Delpy. Our conversations ignited sparks of enthusiasm for spin noise and led to fruitful outcomes. I will miss the days when we all worked together. I would like to also express my gratitude to my mentors for their support in my personal life during my stay in France. I thank Fabien for accompanying me to the police station to file a report when my money was stolen. I also thank Fabienne for doing her best to assist me in applying for CROUS residence. I would like to thank the Ph.D colleagues who helped and accompanied me in these years. I also appreciate the engineer of LuMIn Sebastien Rousselot who helped us with many engineering issues during our lab shifting.

I am grateful to my friends who cheered each other on during the lockdown, and the friends who once traveled together, those joys made me appreciate the beauty of Europe and let me learn to relax.

I am deeply grateful to E for her trust and encouragement. When I was under big pressure in France, she helped me rebuild

my confidence. In addition, I would like to extend my appreciation to Proser project and China Scholarship Council for its administrative and financial support, allowing me to devote myself to my studies.

Finally, I would like to convey sincere thanks to all my family members for their constant support, enthusiastic encouragement and trust. You have always been my backing, supporting me to move forward and letting me have a chance to see the wonderfulness of the world.

